University of Groningen

Growth of binary oxides on Si substrates

Antoja Lleonart, Jordi

DOI:
10.33612/diss.180860479

IMPORTANT NOTE: You are advised to consult the publisher's version (publisher's PDF) if you wish to cite from it. Please check the document version below.

Document Version
Publisher's PDF, also known as Version of record

Publication date:
2021

Link to publication in University of Groningen/UMCG research database

Citation for published version (APA):
Antoja Lleonart, J. (2021). *Growth of binary oxides on Si substrates: solid solutions of SiO2-GeO2 and HfO2-ZrO2*. University of Groningen. https://doi.org/10.33612/diss.180860479

Copyright
Other than for strictly personal use, it is not permitted to download or to forward/distribute the text or part of it without the consent of the author(s) and/or copyright holder(s), unless the work is under an open content license (like Creative Commons).

The publication may also be distributed here under the terms of Article 25fa of the Dutch Copyright Act, indicated by the “Taverne” license. More information can be found on the University of Groningen website: https://www.rug.nl/library/open-access/self-archiving-pure/taverne-amendment.

Take-down policy
If you believe that this document breaches copyright please contact us providing details, and we will remove access to the work immediately and investigate your claim.

Downloaded from the University of Groningen/UMCG research database (Pure): http://www.rug.nl/research/portal. For technical reasons the number of authors shown on this cover page is limited to 10 maximum.

Download date: 20-11-2022

GROWTH OF BINARY OXIDES ON SI SUBSTRATES

SOLID SOLUTIONS OF SiO_2-GeO_2 AND HfO_2-ZrO_2

Jordi Antoja Lleonart

university of groningen

faculty of science
and engineering

zernike institute for
advanced materials

NWO
Nederlandse Organisatie voor Wetenschappelijk Onderzoek

Keywords: silica thin films, hafnia-zirconia, atomic layer deposition, pulsed-laser deposition, devitrifying agent, crystallization, x-ray diffraction, pole figures, electron back-scatter diffraction
Printed by: Ridderprint (www.ridderprint.nl)

Front & Back: Carlota Garrigós Serrano

Original thesis template from Technische Universiteit Delft, used with permission.

Zernike Institute PhD thesis series 2021-18
ISSN 1570-1530
ISBN 978-94-6416-800-6
The work described in this thesis was performed in the Nanostructures of Functional Oxides research group of the Zernike Institute for Advanced Materials at the University of Groningen, the Netherlands. This work was funded by The Netherlands Organisation for Scientific Research NWO (TOP-PUNT grant 718.016002).

university of
groningen

GROWTH OF BINARY OXIDES ON SI SUBSTRATES

SOLID SOLUTIONS OF SiO_2-GeO_2 AND HfO_2-ZrO_2

PhD thesis

to obtain the degree of PhD at the
University of Groningen
on the authority of the
Rector Magnificus Prof. C. Wijmenga,
in accordance with
the decision by the College of Deans.

This thesis will be defended in public on

Friday 8th of October, 2021, at 16:15 hours

by

Jordi ANTOJA-LLEONART

born on Friday 27th of November, 1992
in Granollers, Spain

Supervisors

Prof. B. Noheda
Prof. B.J. Kooi

Assessment Committee

Prof. M.A. Loi
Prof. W.M.M. Kessels,
Prof. T. Banerjee

CONTENTS

1 Introduction **1**
1.1 Motivation and outline . . . 1
1.2 Brief history of piezoelectricity . . . 3
1.3 Piezoelectricity and ferroelectricity . . . 5
1.4 Quartz . . . 7
1.5 Hafnia-zirconia . . . 13

2 Experimental methods **15**
2.1 Substrate preparation . . . 15
2.2 Atomic Layer Deposition (ALD) . . . 16
2.3 Pulsed Laser Deposition (PLD) . . . 22
2.4 Atomic Force Microscopy (AFM) . . . 24
2.5 X-Ray Diffraction (XRD) . . . 28
2.6 Ellipsometry . . . 35
2.7 Electron microscopy . . . 37

3 ALD growth of SiO_2 and GeO_2 **41**
3.1 Basics of SiO_2 ALD growth . . . 41
3.2 GeO_2 ALD growth . . . 43
3.3 GeO_2 dielectric measurements . . . 46
3.4 SiO_2-GeO_2 ALD growth . . . 48
3.5 SiO_2-GeO_2 film crystallization . . . 51
3.6 Conclusions . . . 56
3.7 Author contributions . . . 56

4 PLD growth and crystallization of $Si_{0.7}Ge_{0.3}O_2$ **59**
4.1 Introduction . . . 59
4.2 Experimental . . . 60
4.3 Results and discussion . . . 61
4.4 Conclusions . . . 77
4.5 Author contributions . . . 77

5 PLD growth of HfO_2-ZrO_2 **79**
5.1 Introduction . . . 80
5.2 Experimental . . . 81
5.3 Results and discussion . . . 82
5.4 Conclusions . . . 97
5.5 Author contributions . . . 97

Summary 99

Samenvatting 103

Curriculum Vitae 107

Acknowledgements 109

Bibliography 117

1

INTRODUCTION

This first chapter sets the stage for the rest of the thesis. It starts with a short outline of the work carried out, which is put into the broader context of current day piezoelectrics. This is followed by a very accessible essay on the history and physics of piezoelectricity, and finally the two materials of interest are introduced: quartz and hafnia-zirconia.

1.1. MOTIVATION AND OUTLINE

Piezoelectric materials, which can efficiently convert mechanical to electrical energy and vice versa, are well-established in today's society in a variety of applications. The direct piezoelectric effect is used in energy harvesting and piezoelectric spark ignition, as well as mechanical sensors. The converse piezoelectric effect is exploited in several kinds of actuators, including those involved in ink-jet printing and high-precision positioning elements such as those required in scanning probe microscopies and adaptable optics for space mirrors.

It is not unusual for both the direct and converse effect to be utilized in a single system, as exemplified by sonar and ultrasound devices, which include an emitter and a receiver. It is also possible to find both effects in use in a single piezoelectric element; that is the case for crystal oscillators which are routinely used as time or frequency standards, very commonly found in electronic devices. A common theme to most of these applications is that they require cheap, widely available, stable materials. This is why a usual choice of piezoelectric is lead zirconate titanate ($PbZr_xTi_{1-x}O_3$, or simply PZT - see Section 1.2); together with related compounds, it has some of the highest reported piezoelectric coefficients, giving it excellent performance. Yet, also together with related compounds, it is remarkably toxic, mainly due to its lead content.

This is inconvenient because devices that use PZT cannot always be recovered at the end of their life, and improper containment in the presence of water can cause their dissolution and release into the environment [1], as can PZT processing without careful atmosphere control [2]. That has sometimes been overlooked in favor of its other outstanding properties, but in the past two decades there has been a legislative effort by the European

Union to minimize the use and release of toxic materials, including lead, in areas such as the automotive industry [3, 4]. It is, therefore, not surprising that lead-free piezoelectrics of high performance are a widely pursued goal in solid state materials, with notable examples being materials related to barium titanate [5], a range of alkaline niobates [6, 7], and bismuth alkaline titanates [2, 8], among others. Moreover, although in this text most aspects of piezoelectricity are approached from the perspective of crystalline oxides, it has been known for decades that this property is also found in polymers [9] and biological samples like bone [10] and wood [11]. Whatever the case, it is imperative to keep in mind that none of these materials are desirable by virtue of being lead-free per se, and that they still must meet criteria such as stability and nontoxicity (this one is probably broken by piezoelectrics based on antimony [12]). As pointed out by Rödel *et al.*, the quest for lead-free piezoelectrics seeks not only to replace PZT, but also to find application in areas where PZT is not a suitable candidate; an example of this is the making of pressure sensors, as PZT depolarizes when subjected to large pressures, and therefore other materials are preferred [1].

The main motivation for this thesis is, therefore, the search for new sustainable piezoelectrics in thin film form. To that end, two different lead-free piezoelectric materials have been investigated.

The first one is crystalline silicon dioxide. This is relevant to the current context of piezoelectricity in chiefly two ways. First, it brings one more push to the area of lead-free piezoelectrics with the use of cheap, abundant and nontoxic material in the form of quartz, while attempting to improve its properties by dissolving into it other oxides, such as germania.

Second, it addresses the need to miniaturize the resonator device in oscillator circuits. The manufacture of higher frequency oscillators (currently made of quartz as well) is desirable to improve the performance of electronic systems [13]. In an electromechanical resonator, the resonance frequency increases as the size decreases [14]. For instance, an ideal quartz cantilever of 1 mm length and 10 μm thickness (square cross-section. This is not what modern resonators look like) has its first natural frequency at 6 kHz. Keeping a constant aspect ratio, at 10 nm thickness the natural frequency reaches 6 MHz. Because of this, the miniaturization of piezoelectric resonators based on current concepts is a historic struggle. Although improved over the years, the method of shaping them from larger crystals makes it difficult to achieve thicknesses below the micrometer scale [15–18] and does not ease integration with electronic devices. With the advent of 5G and its successors, new methods of integrating high-frequency resonators with traditional electronics become urgently needed [13], and making these resonators out of piezoelectric thin films (which can have thicknesses below 100 nn) can offer a solution.

The second focus of the project is a more recent addition to the piezoelectric scene: hafnium zirconium oxide (HZO). This solid solution has seen tremendous attention in the last few years due to its paradigm-defying ferroelectric behavior in the nanoscale, as well as the possibility to integrate it with current CMOS processing. These properties make it a prime candidate for use in nanostructured devices.

In this introductory chapter, after this motivation, the history of piezoelectricity (including ferroelectrics) is summarized. After that, some key concepts in piezoelectricity and ferroelectricity are discussed, followed by material-specific introductions on quartz and HZO. The Experimental methods chapter provides a basis for the research techniques used in following chapters, including the procedures to synthesize and prepare samples as well as the methods to characterize them.

The research chapters follow. In Chapter 3, the growth of SiO_2/GeO_2 multilayers by Atomic Layer Deposition (ALD) is investigated with the eventual aim to produce α-quartz structure solid solutions. Chapter 4 details growth of SiO_2/GeO_2 mixes by a different method, Pulsed Laser Deposition (PLD), and their crystallization. In Chapter 5, the direct PLD growth of HZO on silicon substrates is characterized as well. This is all followed by a short summary of this thesis.

1.2. BRIEF HISTORY OF PIEZOELECTRICITY

The piezoelectric effect is a phenomenon by which objects made of certain materials develop a net electric dipole after a mechanical stress is applied on them; its history is neatly recollected in several documents, for instance the book by Jaffe [19]. The piezoelectric effect was first discovered in quartz crystals and published, under the name of polar electricity, in 1880 by the brothers Jacques and Pierre Curie [20], who in turn had been following Gaugain's work on the pyroelectricity (the generation of a temporary current upon heating or cooling, linked to the presence of a permanent electric dipole) of tourmaline. The Curie brothers noticed similarities between these two properties, which are now understood as closely linked. Indeed, all pyroelectric materials are also piezoelectric, but this will be discussed in further detail in the following sections. The Curie brothers also identified trends in the direction of the piezoelectric axis [21], at that time relating it to certain macroscopic crystal faces of quartz. Only decades later was the crystal structure of quartz elucidated [22, 23].

If an electric field is applied to these piezoelectric objects, by the converse piezoelectric effect they undergo a deformation, or strain. This effect, reciprocal to the direct piezoelectric effect, was predicted by Lippmann [24] and later on confirmed empirically, again by the Curie brothers [25]. The experiment which was used as confirmation also arguably stands as the first true application of piezoelectric materials. In order to detect electrically induced deformations in a crystal, the authors built the very first piezoelectric pressure sensor, which used quartz sheets connected to an electrometer. Although this had all happened during the early 1880s, no wide applications for piezoelectricity would emerge until World War I and the advent of sonar. In 1921, Joseph Valasek explained how the piezoelectricity of Rochelle salt could be influenced, among others, by applying an external electric field to it [26], and he pointed out the similarity of this behavior to ferromagnetism by recording hysteresis loops between surface charge and applied electric field [27], as shown in Figure 1.1. His observations are now widely regarded as the discovery of ferroelectricity (although the term itself was coined later on [28]), which is the phenomenon by which the permanent polarization of a pyroelectric material can be switched with an external electric field. There were (and still are), however, a few issues with Rochelle salt, including instability towards dehydration, which precluded its extensive use.

The next great leap forward in the field, the rise of distorted perovskite ferroelectric materials, happened with the discovery of barium titanate ($BaTiO_3$) during World War II. It appears that nearly simultaneous, independent efforts in that direction were made by several researchers around the world [28]. This includes Japan and Russia, as well the United

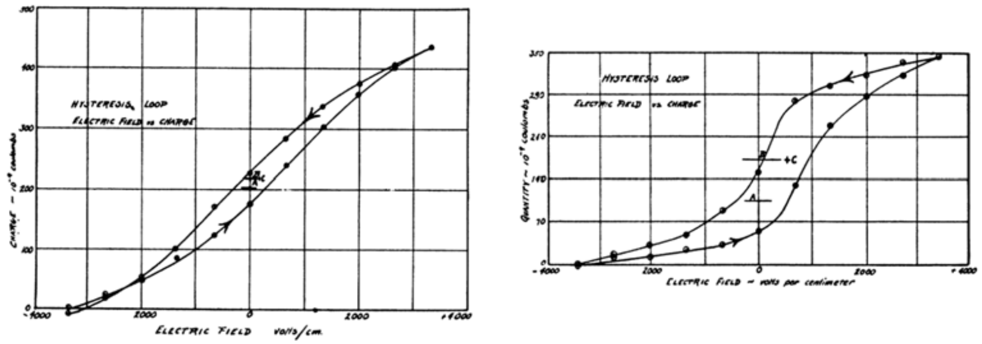

Figure 1.1: (Reprinted with permission from Reference 27. Copyright 2021 by the American Physical Society) Ferroelectric hysteresis loops (see Figure 1.3 for more details) measured by Valasek on Rochelle salt, at 23°C and 30% humidity (left) and at 0°C with a dried sample (right). The charge on the vertical axis is a measure of polarization [29].

States, where interest in barium-doped titanium oxide might have arisen as a result of the need for new dielectric materials to be used in capacitors in view of a possible cut in the supply of mica during the war [30] (this last statement is repeated by several authors with no primary sources given). Barium titanate's dielectric constant turned out to be many times higher than the next competitor; nowadays it is common for many ferroelectric materials to exhibit similarly large dielectric constants. There were observations in barium titanate of a response similar to that found in piezoelectrics of that time, which was difficult to explain due to the polycrystalline nature of this new ceramic. It was known that the piezoelectric response should vanish for samples made of randomly oriented crystallites (large single crystals would not be produced until 1954 [30]). As published for the first time by Roberts [31] in 1947, barium titanate polycrystals would indeed show the piezoelectric effect if they had been poled previously using a sufficiently large electric field. Because of that, and its general stability in ambient conditions, barium titanate was used in the following years not only as a dielectric, but also as a piezoelectric material in a wide variety of applications.

The case of barium titanate led to an increased interest in ferroelectric perovskites, which reached a milestone with the solid solutions between lead titanate ($PbTiO_3$) and lead zirconate ($PbZrO_3$), referred to as lead zirconate titanate, or PZT. While lead titanate is a ferroelectric [33, 34], lead zirconate itself is antiferroelectric at room temperature. The work on doped $PbZrO_3$ by Shirane et al. in the fifties [35, 36] showed how, with sufficient doping, $PbZrO_3$ can be brought to a ferroelectric phase, even down to room temperature [37, 38] , and that the atomic percents of Ti and Zr in the PZT solid solution determine whether the material is rhombohedral or tetragonal [39]. It was found [32] that at the composition boundary between the two crystal stystems, which is usually referred to as a Morphotropic Phase Boundary [40] (MPB), the solution displays enhanced electromechanical properties (see Figure 1.2), including piezoelectric coefficient, dielectric constant and electromechanical coupling factor [41]. It is so much so, that PZT soon became, and still is today, the material of choice for a great number of piezoelectric applications. Never-

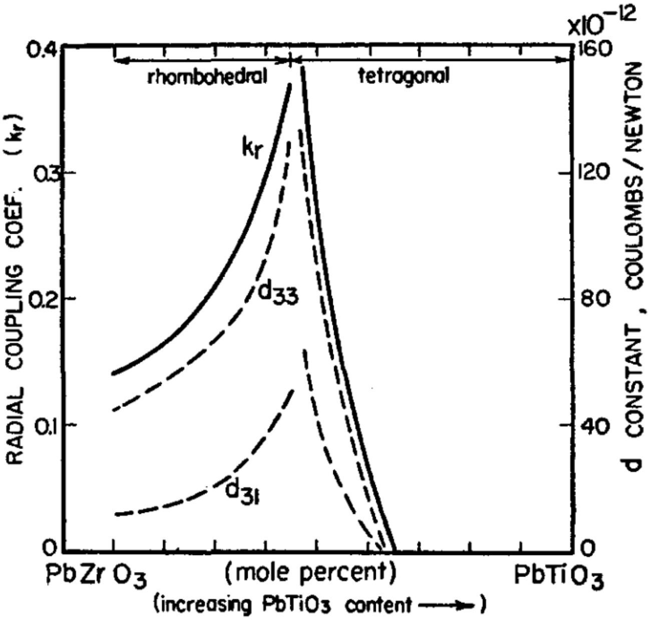

Figure 1.2: (Reprinted from Reference 32, with the permission of AIP Publishing.) Composition dependence of the coupling coefficient and the piezoelectric coefficient of PZT ceramics.

theless, we know now that enhanced piezoresponse near the MPB is not exclusive to PZT [6, 7]. In the recent decades, progress has continued, and materials have been synthesized with much larger piezoelectric response, but PZT can be superior due to other properties which overall make it preferable, such as polarization stability, low temperature-dependence of properties, and the possibility to be used as easily synthesized ceramics rather than single crystals [41]).

1.3. PIEZOELECTRICITY AND FERROELECTRICITY

In the direct piezoelectric effect, a certain material polarization arises from the application of a mechanical stress. In the converse piezoelectric effect, a strain is generated by applying an electric field. In both cases, the response is linear for small stimuli only.

Piezoelectrity is an anisotropic by definition. This means that it strongly depends on the direction along which it is measured. A thorough explanation for this and other anisotropy-related properties is not included here, but can be found in the book Properties of Materials by Newnham [11]. We can start with the following equations, which correspond to the direct and converse piezoelectric effect, respectively.

$$(P) = (d)(X) \tag{1.1}$$

$$(x) = (d)_t(E) \tag{1.2}$$

E and P are the electric field and polarization (first rank) tensors, X and x are the stress and strain (second rank) tensors, and d is the (third rank) tensor containing the small-signal piezoelectric coefficients. This tensor contains 18 independent coefficients, and it is there that any particular material's piezoelectric properties are captured.

From a mathematical standpoint, all non-symmetric objects can have nonzero piezoelectric coefficients. This means that, by applying some stress (respectively, electric field) to the material, it is possible for it to become electrically polarized (respectively, mechanically strained). The piezoelectric coefficient tensor relates the direction and strength of the piezoelectric (respectively, converse piezoelectric) response to the direction and strength of the stimulus that triggered it.

The discussion goes one level deeper when we limit our scope to symmetric crystals, and in particular to those belonging to one of the 32 crystallographic point groups (although it also applies to the Curie groups, which contain one or more ∞-fold axes). Here we must observe Neumann's principle: *The symmetry of any physical property must include the symmetry elements of the point group of the crystal.* What this means in practice is that, because of symmetry in the crystal structure, there are certain rules that the piezoelectric coefficient tensor (among others) needs to follow. We will not dive here into the calculation, but the result is that, for many point groups, one can establish constraints between the various piezoelectric coefficients, such that some of them become equal to others, some become opposites, some become more complicated sums and multiples, and some become *zero*.

This is an important conclusion. There are point groups for which all the piezoelectric coefficients are zero. These include all eleven centrosymmetric point groups as well as group 432, and they are collectively known as the nonpiezoelectric groups. Note that, for piezoelectric materials, algebra cannot predict how large the nonzero piezoelectric coefficients are, and so just because symmetry allows a material to be piezoelectric, it does not mean that piezoelectricity will be measurable or useful.

Of the remaining 20 piezoelectric groups, there are 10 which allow the presence of a permanent electric dipole in the unit cell: these are the polar pyroelectric groups, named so because the polarization reversibly vanishes when heated above their Curie temperature. This transition (either way) generates a current in what is called the pyroelectric effect. In some cases, the permanent dipole in a pyroelectric can be switched by applying an external electric field. Materials with this property are called ferroelectrics.

This, however, can be an extremely unwieldy definition, mainly due to the difficulty inherent in trying to prove whether the polarization of a material has indeed been switched. Electric polarization is not well defined in perodic systems [43], but changes in polarization are accessible. Going forward, I will refer as ferroelectrics to insulators that, when subjected to an electric field sweep of sufficient amplitude, reversibly exhibit two complementary peaks in current additionally to any resistive background current, as shown in Figure 1.3. These two peaks correspond to the switching towards the two stable polarization states, and the field values at which these peaks appear are referred to as the coercive field. We *interpret* the switching peaks as changes in the polarization of the material, and thus a change of sign in its bound charge distribution. Again, we establish ferroelectricity not on the basis of the polarization, which is problematic, but on motion of charges instead.

For a given material, ferroelectricity reversibly vanishes above the Curie temperature

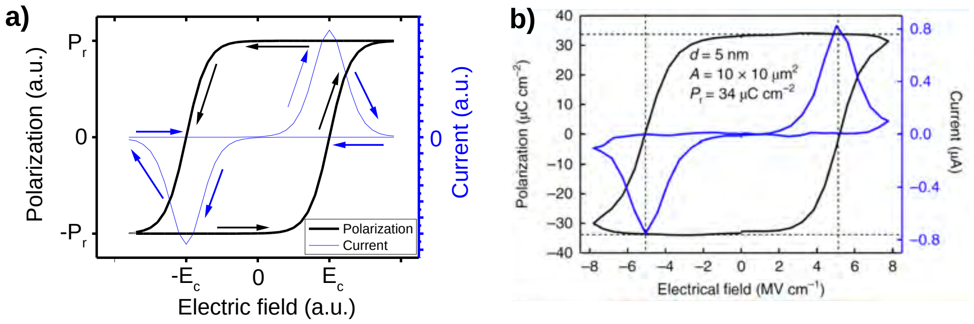

Figure 1.3: a) Ideal ferroelectric loop showing electric polarization vs. electric field (black curve). Polarization is not directly measurable, so instead the current (blue curve) is measured and integrated over the sweep time, then divided by the contact area to yield the change in surface charge, which is then equated to a change in polarization. When the coercive field (E_c) is reached, a current spike appears and the polarization switches. If the field is removed, the polarization takes one of two stable values, which are referred to as remanent polarization (P_r). b) (Reprinted from Reference 42 with permission from Springer Nature Customer Service Centre GmbH) Ferroelectric loop of a HZO 5 nm-thick film.

(pyroelectric effect), which marks the boundary between a low-temperature ferroelectric phase and a high-temperature paraelectric phase. On that note, the distinction between a paraelectric and a dielectric material can be confusing because of the deceptive parallel to paramagnetism and diamagnetism. To avoid misunderstandings, a material is called paraelectric if it has a known low-temperature ferroelectric phase [1], and dielectric otherwise, but let it be stated here that the two different terms in no way signify a difference in their respective electric properties.

1.4. QUARTZ

1.4.1. BRIEF HISTORY

Quartz (together with its more colorful varieties, such as amethyst, onyx or citrine) is one of the oldest materials used by humankind, found in archaeological assemblages predating the first written texts [45]. Quartz has since been important in technological terms, as an abrasive and in toolmaking [46, 47], but it has also often found in jewelry [46]. Quartz can be mined from natural deposits, and in practice these have been the main source of quartz for humankind during most of recorded history.

In more recent times, quartz has become important for its piezoelectricity as well. For applications that exploit the piezoelectric properties of quartz, mining no longer satisfies global demand for high-quality single crystals. Artificial quartz synthesis was achieved already in the eighteenth century and macroscopic crystals were grown in the 1900s by G. Spezia [48] with a hydrothermal method which is fundamentally quite similar to the one in use today. Crucially, the slow synthetic growth rates and abundant supply of natural quartz drowned out further interest in this development at that time. In a rather fitting parallel to the rise of $BaTiO_3$ (see Section 1.2), the starting point of serious interest in

---

[1] There is also the special case, with which we do not deal here, of quantum paraelectrics, of which a common example is $SrTiO_3$ [44].

quartz synthesis can be found in World War II, where Germany was locked out of quartz imports and in dire need for a source of quartz to use in radio manufacturing [17]. This jump-started efforts into hydrothermal growth, which was further pursued by the US and the USSR at the end of the war.

1.4.2. BULK MATERIAL: STRUCTURE AND PHASES

Silica and silicates are some of the most common compounds in the earth's crust, with SiO_2 alone comprising over 66% of the upper crust's mass [49]. Silica, or silicon dioxide, itself has thirteen polymorphs, of which two are noncrystalline. Of the eleven remaining, nine consist of networks of SiO_4 tetrahedra which are interconnected through their vertices, that is, every pair of silicon atoms is bridged by an oxygen atom.

One of these polymorphs is quartz, which in turn has two separate phases, both of them piezoelectric [50]: α-quartz, or low quartz, and β-quartz, or high quartz. α-quartz itself is usually referred to simply as quartz, which could be expected to generate some confusion. In practice, that is usually not the case as β-quartz transforms with no bond breaking into α-quartz below 573ºC at 1bar (to be more precise, the transition takes place over a 1.3^oC temperature range) [51]. This means that at normal temperature and pressure β-quartz will not be present most of the time. α-quartz has two enantiomorphs, one right-handed and one left-handed, which respectively belong to space groups $P3_221$ and $P3_121$ (trigonal, point group 32). The situation is similar for β-quartz, whose two enantiomorphs have space groups $P6_222$ and $P6_422$ (hexagonal, point group 622) [23]. The bulk properties of α-quartz have been extensively investigated, and characteristic values can be easily found in the literature for its elastic, dielectric and piezoelectric coefficients [15, 52, 53].

1.4.3. INDUSTRIAL GROWTH AND APPLICATIONS

When attempting to synthesize quartz, it is necessary to find a method that, with the right parameters, promotes the growth of the quartz polymorph over others, such as tridymite or cristobalite. See Figures 1.4 and 1.5 for a quick look at the phase behavior of low-pressure silica polymorphs.

Do note that these offer a simplified picture [51]: methods that start from amorphous silica and follow high-temperature crystallization steps can yield one polymorph or another depending, in complicated ways, on process parameters such as salts present in the matrix [55], or on temperature itself: see Reference 56, where different polymorphs form at different process temperatures within the stability range of tridymite. These methods are not employed in industry due to their inability to produce large amounts of high-quality quartz.

Large pure quartz crystals are *not* usually grown from the melt, which is the case in the relatively common Bridgman or Czochralski processes [17]. Instead, quartz is usually grown by a time-tested hydrothermal method [57], which uses autoclaves at high pressure to transfer material via an alkali bath from a silica source to a quartz seed crystal. The process takes place with only moderate heating, and temperature gradients between the source and the seed may or may not be applied. The principle of this method has not changed much for the past 150 years [57] and, although it results in relatively slow growth, it provides high-quality commercially viable single crystals which can then be cut and

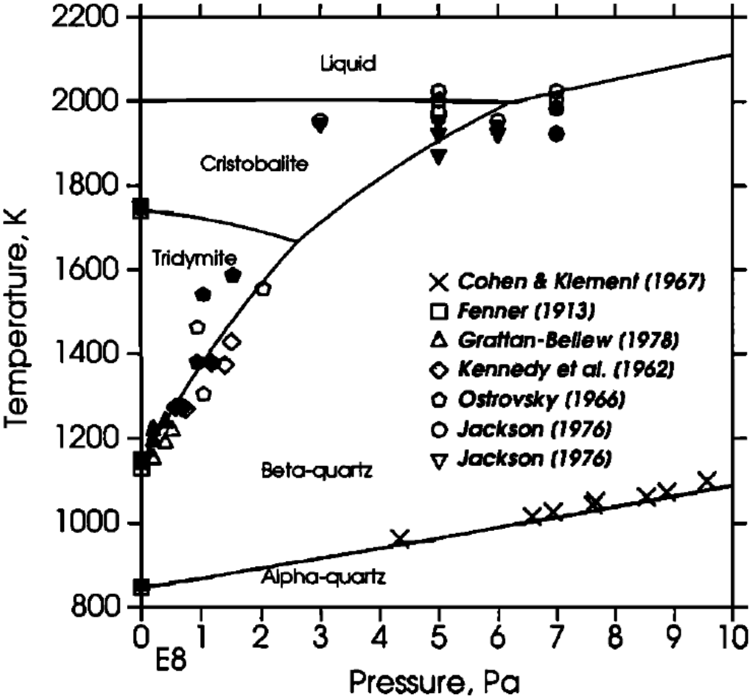

Figure 1.4: (Reproduced from Reference 54 with permission from John Wiley and Sons. Copyright 1994 by the American Geophysical Union.) Silica phase diagram. Only α-quartz is stable at room temperature, but both tridymite and cristobalite are metastable. Note that the temperature scale is in K and that room pressure is about 1 bar, right next to the left vertical axis.

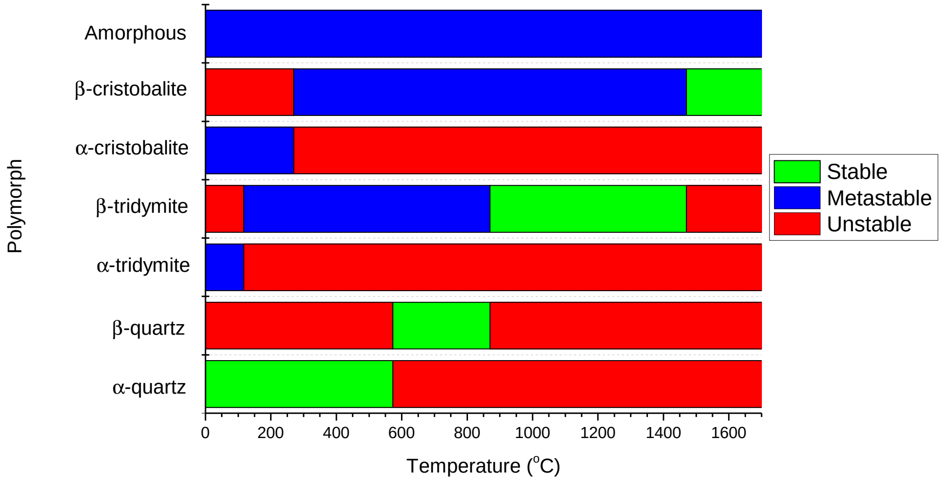

Figure 1.5: (Data from Reference 51) Stability of low-pressure silica polymorphs as a function of temperature (centigrade). Below 870°C, for any temperature there are three metastable phases in addition to the stable quartz phase.

polished for a variety of applications. Moreover, it has been shown experimentally that this method can allow, in some cases, controlled doping of the crystals [58].

Quartz is used, among others, in applications that exploit its piezoelectricity in resonators; these are most interesting to us, and they include such remarkable devices as the Quartz Crystal Microbalances, with which it is possible to track the growth of a thin film to monolayer precision on a quartz resonator using the Sauerbrey relations[59]. By far the most widespread use of piezoelectric quartz crystals is, however, in electromechanical resonators, which are used in electrical oscillator circuits as frequency standards (or clocks)[60] upon which many ubiquitous electronics systems rely, including wireless communication, navigation, and computers [61].

1.4.4. THIN FILMS

It was mentioned in Section 1.1 that thin films are good candidates when piezoelectric transducers need to operate at high frequencies (several tens of GHz for 5G technology [13]). Indeed, in fundamental acoustic modes the wavelength is twice the thickness of the resonator. This means that higher frequencies require increasingly thin devices. For instance, in Reference 18 a resonator with thickness of 650 nm has its fundamental frequency of 1.94 GHz. Devices with such low thicknesses can be quite complex to build if one starts with a bulk piezoelectric crystal, as mechanical polishing alone is not enough, and it needs to be followed by plasma and reactive ion etching.

Therefore, for several decades, piezoelectric thin films have been candidates to build high frequency transducers [62] with simpler fabrication methods. For that application, it is important for the film to have a net piezoelectric response, which means that amorphous silica or polycrystalline quartz are not suitable for this application. Likewise, some films may be composed of non-piezoelectric silica polymorphs, such as many forms of tridymite; although mentioned only sporadically, α-cristobalite itself is piezoelectric [15, 63]. If non-piezoelectric phases are avoided, however, a net response can be achieved. This is the case in the work by Takahashi and his colleagues [64–67] , who were able to grow epitaxial quartz films on sapphire (0001)-cut substrates and prove that they can be used as oscillators. To that end, chemical vapor deposition (CVD) was used, which is easier to upscale than many of its physical counterparts, and therefore it is more suited to industrial production.

There are also a number of reports on the use of ion implantation to promote the crystallization of initially amorphous silica films. An early report was that by Devaud et al. [68], who implanted natural quartz with Si^+ and O^+ ions to amorphize the surface and then showed that annealing the samples in air caused their recrystallization, as evidenced by Rutherford backscattering (RBS) and electron diffraction; this process is commonly known as Solid Phase Epitaxial Growth, or SPEG. Roccaforte et al. achieved similar results by first growing amorphous silica films on quartz substrates [69, 70]. Afterwards, they implanted their samples with Cs^+ ions, amorphizing the films and part of the substrates, and subsequent annealing in oxygen caused the recrystallization of both. These publications also put special emphasis in the fact that not all implanted ions can work for this. As an example, the implantation of Xe^+ ions and annealing results in the formation and of Xe bubbles rather than silica recrystallization. Additionally, the work by Dhar et al. shows how there is an upper temperature limit for the ion-induced amorphization to take place, which likewise depends on the ion species and the target material [71, 72], and that partial recrystallization is still possible when the annealing step is altogether replaced by a pulsed UV laser irradiation [73].

Other groundbreaking, more recent collaborations between Drisko[74, 75], Carretero-Genevrier [76, 77], Zhang [78], and others also took place in the area of nanostructured quartz, including thin films. Their approach uses chemical solution deposition (CSD) growth based on known, well-established processes. In its simplest variation, the CSD approach begins with the preparation of a precursor solution. Using ethanol as the solvent, they add tetraethyl orthosilicate (TEOS), hydrochloric acid, a surfactant, and a strontium salt. Chemists may recognize this as the setup to the Stöber process [79] with acid catalysis [80]. This is a well-known method to obtain monodisperse, spherical silica nano- and microparticles, which are then stabilized in suspension by the surfactant. This suspension is dip-coated onto a Si(100) wafer, allowed to evaporate and then consolidated in an oven. This leads to both the precipitation of the strontium salt and the assembly of surfactant structures [81], which will be embedded in the silica film. The film is subsequently annealed in the presence of oxygen, at which point the strontium acts as a melting agent. This promotes the crystallization of the silica at the Si/SiO_2 interface, and it is the epitaxy with the Si(100) surface that selects the α-quartz polymorph over the others. X-ray diffraction analysis reveals that the resulting quartz films are polycrystalline, with strong preferential orientation resulting in a measurable piezoelectric response.

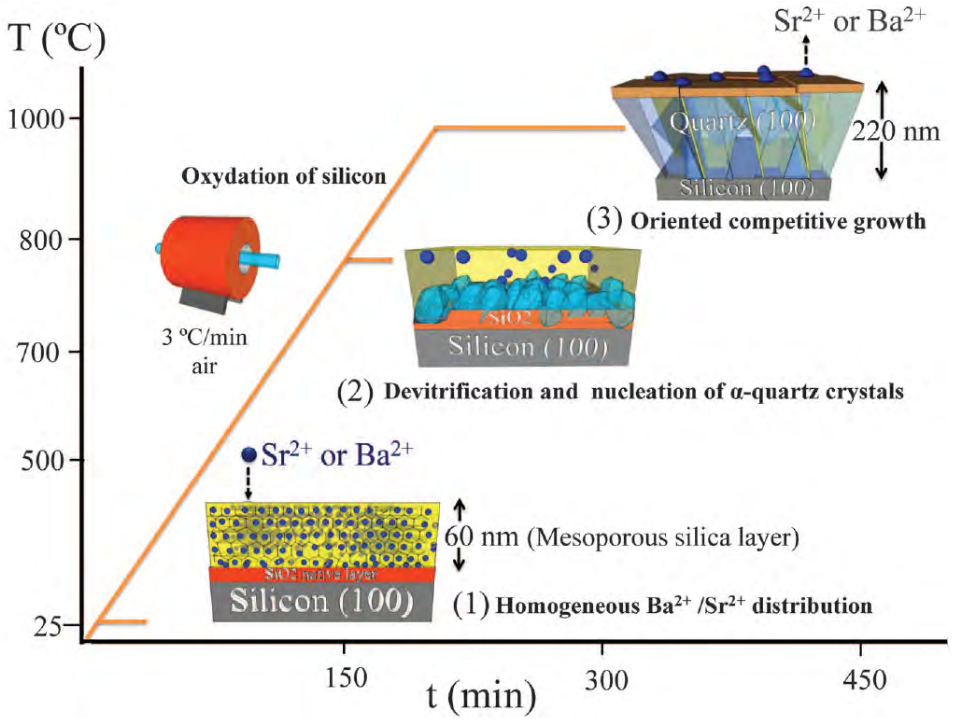

Figure 1.6: (From Reference 76. Reprinted with permission from AAAS.) Sketch of the heating step initially used by Carretero-Genevrier *et al.* to convert an amorphous silica film into textured quartz.

1.5. HAFNIA-ZIRCONIA

1.5.1. OVERVIEW

Part of this thesis is dedicated to the growth and characterization of thin films of a very different, and much more modern material. This is a solid solution of hafnium (IV) oxide and zirconium (IV) oxide, which has the general formula $Hf_{1-x}Zr_xO_2$ and is often referred to with its unofficial acronym (HZO) or simply as hafnia-zirconia.

Hafnium (Z = 72) and zirconium (Z = 40) have very similar chemistry and in nature they are routinely found together in the form of zircon (hafnium zirconium silicate) mineral, where zirconium atoms are about 36 times more abundant than hafnium [82] (both elements indistinctly occupying the same crystal sites). From zircon, the base metal Zr (and its compounds) is produced, with a major Zr consumer being the nuclear energy industry. There it is employed in alloys with low neutron absorption, for which it is important to remove any hafnium impurities (which have high neutron absorption) from it [83]; this activity is the main source of hafnium in the market. Thus hafnium is certainly less readily available to us than silicon is in terms of production per year.

1.5.2. FUNCTIONAL PROPERTIES

Its physical availability notwithstanding, HZO (including its end members) has seen a rise in popularity in the recent years when hafnium dioxide, a fluorite-structure insulator, was proposed as a high dielectric constant gate dielectric replacement in MOSFETs (Metal-Oxide-Semiconductor Field-Effect Transistors) [84]. Materials with higher dielectric constants, compared to that of the prototypical dielectric SiO_2, were necessary for the reduction of the gate oxide thickness in MOS transistors, which in turn could lead to device miniaturization, increasing packing density.

In the field of functional oxides, it is not unusual to read about the "CMOS compatibility" of a compound. Although sometimes used loosely, this is mainly said about materials which are stable in contact with silicon (necessary for reliable and long-lived operation as part of an electronic device), and which have compatible processing temperatures with the rest of the chip fabrication: this means that a CMOS compatible material needs to have synthesis temperatures which are not too high for the rest of the components, while at the same time it must be stable at the temperatures at which those other components are added.

Amorphous HfO_2 crystallizes into its monoclinic phase near 450°C, which can be a challenge in CMOS processing. For this reason, efforts to improve its applicability have included mixing it with silicon or aluminium oxide in order to raise its crystallization temperature, or with zirconium oxide in order to stabilize higher-k phases than the amorphous or monoclinic one [85].

Subsequently, Böscke et al. would go on to stabilize ferroelectric HfO_2 thin films with a small Si doping [86], and other dopants would later be successfully used as well [87, 88]. This is significant because, as mentioned, the common polymorph of HfO_2 is a centrosymmetric (thus nonpolar) monoclinic phase. Both a rhombohedral and orthorhombic polar phase of HfO_2 have been identified since, with each being hailed as the one responsible for ferroelectricity in one case or another.

The phase behavior of HfO_2 and ZrO_2 solid solutions has also been investigated. Owing to the similarity between the two components, these solid solutions can span the entire composition range between them. This allowed Müller *et al.* to observe how the thin film structure went from monoclinic (dielectric) for pure HfO_2, to tetragonal (antiferroelectric) for pure ZrO_2, passing through an orthorhombic ferroelectric phase for intermediate compositions [89, 90] (see Figure 1.7b).

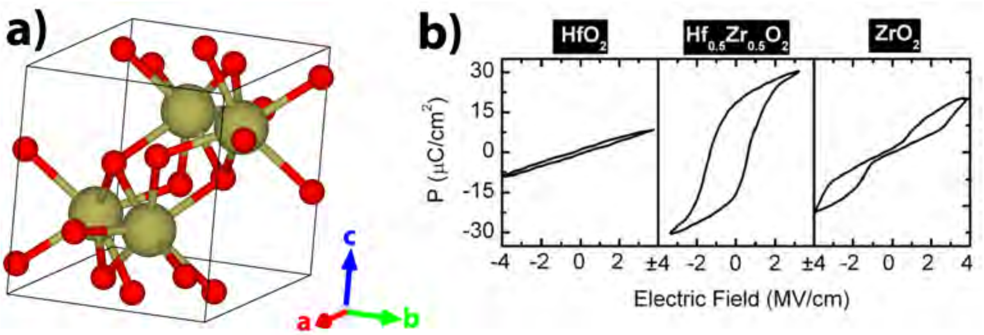

Figure 1.7: a) Unit cell of the monoclinic HfO_2 polymorph [91, 92], with the Hf atoms in yellow and O atoms in red. b) (Reprinted (adapted) with permission from Reference 90. Copyright 2021 American Chemical Society.) Polarization vs. field loops for three compositions of HZO, showing the transition from dielectric to antiferroelectric, through a ferroelectric phase.

It is unsurprising that the MPB between the tetragonal and orthorhombic phases of HZO has also sparked interest. The dielectric constant peaks near this boundary [93, 94], while also being dependent on film thickness.

Ferroelectricity in HZO thin films is currently an area of intense research. Among its main attractives is its unconventional scaling with size [42, 95]. Normally, ferroelectricity vanishes below a certain film thickness, but there is evidence signaling that in HfO_2 the opposite is true, and that the polarization increases in ultrathin films while disappearing at larger thicknesses. This is not just a curious oddity: it makes HZO extremely attractive in ferroelectric nanostructures which would not be possible using other materials.

As a final note, it should be added that HZO solid solutions (including the end members) are not only attractive lead-free ferroelectric materials or high-K dielectrics. There has been some attention for the piezoelectric properties of HZO [86, 89, 96, 97], although these are far from the core of HZO research. They have also been used in a variety of other settings, including as part of multiferroic tunnel junctions [98, 99] or memristive stacks [100].

2

EXPERIMENTAL METHODS

This chapter details the most important experimental methods that have been used in this thesis. For all of them, detailed descriptions exist in reviews and textbooks; references to some of these are given in the text. Included here are also seldom-discussed but important details, such as the correction of AFM images or the precision of XRR parameters. The aim of this chapter is to give a practical but accessible picture of the techniques used.

2.1. SUBSTRATE PREPARATION

This thesis deals with the growth of thin films on single-crystalline substrates. In thin-film research, the choice of substrate (material, orientation) and the quality of its surface have an important effect on thin-film growth. For this project, different substrate types were used at various points, but in the vast majority of experiments the substrates were silicon single crystals. These were typically cut down to 15x15 mm^2 pieces from one-side-polished Si(100) wafers which were purchased from MicroChemicals GmbH. These were 0.5 mm in thickness and 4" in diameter, Czochralski-grown, and (boron) p-doped to 1-10 Ωcm resistivity. The wafers were first scored with a diamond pen and later broken apart either manually or using specially designed pliers.

Then a washing procedure in a fume hood was performed to remove dirt and particles that may remain on the polished surface, as follows: newly-cut substrates were washed in ethanol, then rubbed using an ethanol-soaked optical cloth. Afterwards they were cleaned in an ultrasound bath using several solvents, for 15 minutes each: first ethanol, then acetone, and finally isopropyl alcohol. Subsequently, the substrates were individually withdrawn from the beaker, the ethanol washing and rubbing step was repeated, and they were blow-dried using pressurized nitrogen before being ready to use. The rubbing steps are important to ensure the removal of most large particles. Other approaches exist; a common one is spin-coating a layer of resist, such as PMMA, on a wafer before cutting it and then simply removing it, along with any silicon dust that may have attached to the surface. However, the cleaning steps used in the project are sufficient to ensure a clean enough surface while using very little equipment, chemicals and labor.

2.2. ATOMIC LAYER DEPOSITION (ALD)

2.2.1. OVERVIEW

Atomic Layer Deposition (ALD; occasionally "pulsed metal organic chemical vapor deposition" is used instead of ALD, though in practice both methods are very similar) is a technique for the growth of thin films which was developed, at first independently, in Finland and the Soviet Union in the second half of the twentieth century (see Reference 101 for a more thorough review). This technique is a variation of classic Chemical Vapor Deposition (CVD). Like most CVD processes, ALD uses a reaction chamber with controlled temperature and flowing precursors transported in the gas phase. What sets ALD apart from other methods is that it relies on self-terminating gas-solid reactions and, with the proper choice of precursors, it has much better control over the thickness of the resulting film. Although this thesis deals mostly with binary oxides, ALD is also used to grow metals [102], and recently more complex, multicomponent materials [103, 104], including perovskites [105–109] have been realized as well.

An ALD system needs at least a vacuum chamber with inlets for the precursor and purge gases, and nearly always features temperature control of the chamber. For this thesis, an R-200 Advanced hot-wall ALD System manufactured by Picosun ® was used. The reactor chamber opens to a glovebox containing a nitrogen atmosphere, with controlled oxygen and water concentrations, and the glovebox itself is located inside the NanoLab Groningen clean room (class ISO 6). In this project, the ALD processes use organometallic precursors for Si, Ge and Hf, and ozone as the O precursor, from an INUSA Ozone Generator using Oxygen 6.0. Except for oxygen, the precursors are housed in heated canisters and are delivered to the main chamber using nitrogen as carrier gas. A sketch of the main features of an ALD system is shown in Figure 2.1 .

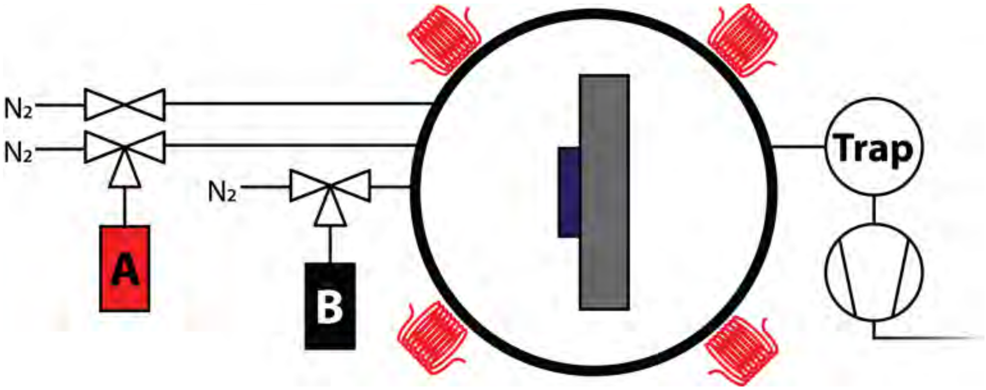

Figure 2.1: Schematic of an ALD system. On the left side, the precursor gas lines (inlcuding three-way valves) for A and B are pictured, as well as a nitrogen purge line. These lead into the heated vacuum chamber, where the sample (navy blue) is located. To the right, a vacuum pump evacuates the chamber, with a trap in between to stop the precursors beforehand.

A regular ALD process involves the sequential repetition of a small number of basic steps. These are illustrated in Figure 2.2. Initially, there is a bare substrate, on the surface of which one wishes to grow a thin film. In the ideal case, the surface of this substrate is flat and it has a single chemical termination. The substrate is placed inside a reaction chamber, in rough vacuum. The chamber walls and the substrate stage are often, but not always, held at a temperature higher than room temperature. Normal operating temperatures do not surpass 600°C, and indeed one of the main advantages of ALD is that, depending on the exact process, it can work at reasonably low temperatures, particularly in the case of Plasma-Enhanced ALD (PEALD). This reduces energy consumption and it allows the use of a wider range of substrates, but most importantly makes it attractive for the electronics industry.

In the first step of an ALD cycle, the chamber is filled with a low pressure of precursor gas. This is accomplished by running an inert carrier gas, often nitrogen, through a line connected to a precursor source. We can call this first precursor gas A. Upon arrival to the chamber, the molecules of this gas can react with the surface groups of the substrate and chemisorb. Importantly, these molecules do not react with each other, so that all the reactions take place at the sample surface. Because of that, once the surface groups all have reacted (this will be rebutted below, but let us assume for now that they all react) the reaction stops by itself and one has achieved the deposition of a single layer of molecule A. The chamber is then evacuated of precursor A, for which an inert purging gas such as nitrogen or argon is used, and then precursor B is introduced. This precursor reacts, again, not with itself, but with the functional groups in precursor A, which are now making up the sample surface. The reaction is allowed to terminate just like the previous one, the chamber is purged again, ending the first ALD cycle. The substrate surface, now with one more layer grown on it, is ready to react once again with precursor A, or any other appropriate precursor.

Because the reaction is controlled by the availability of reactive surface groups, ALD ideally results in the growth of exactly one monolayer of each precursor for every cycle, and it is not strongly affected by small, local inhomogeneities in the surface temperature or in the partial pressure of the precursors. The number of cycles for a growth experiment can be controlled exactly, and so the thickness of the resulting film can be, in principle, also controlled down to the single-atom level, which is why it is called Atomic Layer Deposition.

For long enough exposure times (so that each precursor can travel to all points of a sample's surface), ALD growth is also known for being conformal, meaning that it will uniformly cover any structures previously present on the substrate regardless of their shape. This stands in clear contrast to most other methods, particularly Physical Vapor Deposition techniques, which in many cases tend to result in highly directional growth, generating shadow areas and preventing good coverage of complicated geometries and submicron structures (see Figure 2.3). The conformality of ALD is one of its main advantages for three-dimensional device fabrication, as it allows unprecedented thickness control across samples that have high aspect ratio structures. This includes, for instance, new field-effect transistor architectures, such as the FINFET, which have become increasingly important in the past decade [111] . Also of interest to industry, conformal growth allows the identical processing of a high number of substrates or wafers simultaneously in a single reactor, with the assurance that their position and orientation with respect to the precursor source will not affect the deposited film.

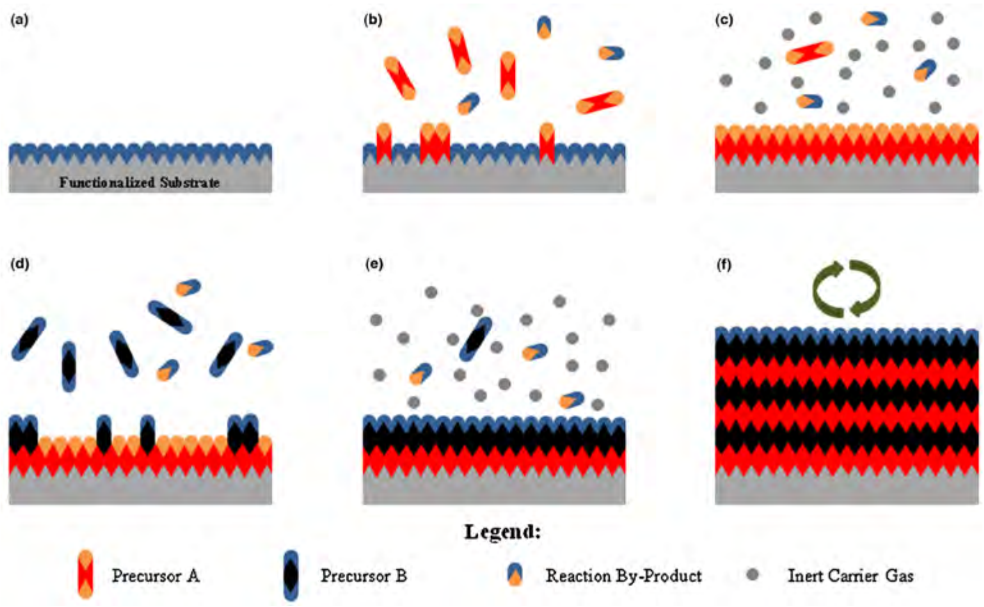

Figure 2.2: (Reprinted from Reference 110, with permission from Elsevier) Sketch of an ideal ALD process. A precursor molecule reacts with the surface groups (b) until saturation, at which point the chamber is purged (c), flushed with the second precursor, which reacts with the new surface (d), and is finally purged again (e) leading to the end of the first ALD cycle, which can be repeated successively (f).

Figure 2.3: Comparison between a) conformal growth, and b) non conformal growth. Conformal films are favorable for applications where uniform coverage is needed to prevent short circuits or other nonuniform behavior, whereas non conformal, or directional growth is preferred when only one side of a feature needs covering, such as in lift-off procedures.

2.2.2. NON-IDEAL ALD GROWTH

The description so far is valid only for ideal ALD processes, and real cases tend to proceed differently. For any single experiment, there are many reasons this might be the case, and some of them are summarized in Figure 2.4. The first necessary condition for ALD-type growth is that the precursors' interaction with the surface is irreversible. This is achieved by using very reactive precursors, normally metal halides or metalorganic compounds, that react strongly with surface sites; elemental precursors, such as tin, gallium and phosphorus, were used in early instances of ALD [112] , but they can have low vapor pressures, and in some cases they show problems with reversible adsorption, complicating the self-termination of the surface reactions. The development of new precursors therefore focuses on molecules that, while inert towards each other, may react at the surface more quickly, at lower temperatures and resulting in less harmful byproducts. This is why metal halides, which may release halogen hydrides onto the sample surface have, in many cases, been phased out in favor of alkoxyde and alkylamine compounds. For common processes the problem of reversible adsorption can be solved by choosing the appropriate reaction conditions for the precursors.

Another problem to solve is that of incomplete surface coverage. So far there was the assumption that the surface is uniformly and completely covered with functional groups that are available to react with the incoming precursor molecules. Not only is this hardly true in general (see Reference 113 for an example), but even if it were, it would still not solve two major issues of real ALD growth. First, the number of reactive surface groups can be strongly affected by the temperature at which the substrate is held, and thus changing the temperature will affect how much surface coverage is provided by each ALD cycle. Second, even if there were sufficient active surface groups for a full monolayer, there is steric hindrance between the precursor ligands to be considered. If a precursor is used that has very bulky ligands attached to a metal atom, it might be the case that, once a molecule reacts with a surface group, it blocks nearby surface groups from reacting with subsequent precursor molecules. Thus, steric hindrance also reduces the amount of material that can be deposited in a cycle.

For these reasons, it is useful to characterize the performance of any given ALD process at a certain temperature by its growth per cycle (GPC), which is the number of monolayers that are grown, on average, by each ALD cycle. This number is usually between 0 and 1 when given in "monolayer" units, but it can also be reported as a thickness value. Inordinately large GPCs of 32 or 52 have been reported for a process known as rapid SiO_2 ALD [114, 115] . These experiments could be loosely described as polymerization reactions from the gas phase which are mediated by a surface-bound catalyst, and they seem to be limited not by the availability of surface sites, but by the diffusion of the precursor molecules to the catalyst sites. Therefore, by some definitions, they do not qualify as ALD and it is still generally correct to state that in *true* ALD all GPC values will be lower than 1.

This is still an excessively simplistic picture, as it fails to consider that the GPC of a given ALD process need not be constant along a single ALD run. In the initial description it was implied that, after precursor B is done reacting, the film surface is chemically identical to how it was in the pristine substrate. This way, with every new ALD cycle, the incoming precursor molecules "see" the same surface, resulting in the same growth for every new cycle. Considering how the original substrate surface is gradually covered with

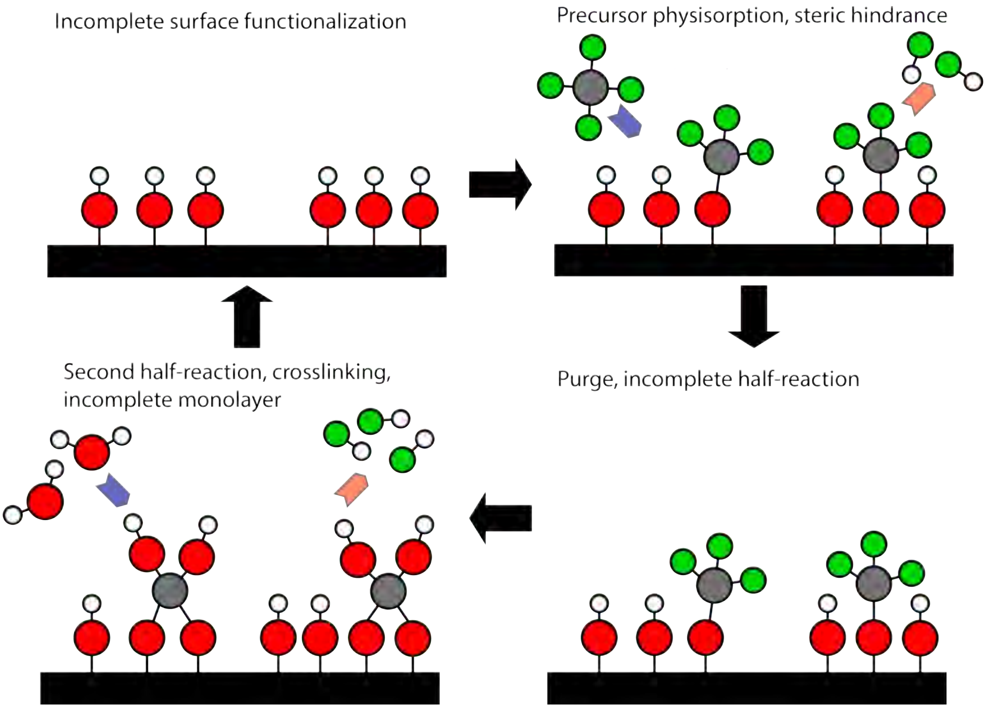

Figure 2.4: Sketch of a few common sources of non-ideality in ALD growth.

new material, possibly changing its chemical properties, it is not difficult to imagine that this is not always the case in real processes. After enough cycles, any ALD process may settle into a steady regime of constant GPC, but this usually only happens after an initial transient regime where the GPC can vary from one cycle to the next (this can be seen in References 116 and 117).

The precise behavior depends on the specifics of the interactions between the precursors, the growing film and the substrate surface; see Figure 2.5 for some of the more common cases. In some cases, the substrate surface may contain fewer active groups than the growing film, in which case the GPC is expected to be initially lower and then increase and saturate as the film completely covers the substrate. This case is known as substrate-inhibited growth of type 1. Substrate-inhibited growth of type 2 shows a peak before reaching the linear regime. A good example of this can be found in Reference 117, where this is caused by an initial 3D growth, which results in islands that have increased surface area, increasing GPC until those same islands coalesce, and the GPC decays to its linear-regime value. Reciprocally, substrate-enhanced growth also exists, where the reaction with the substrate proceeds faster than with the new film.

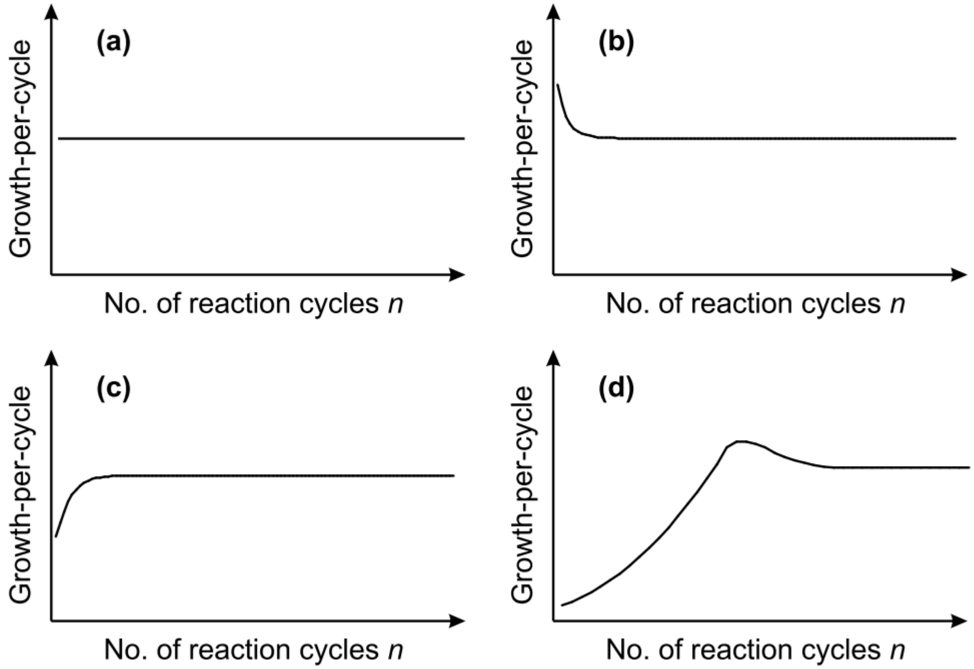

Figure 2.5: (Reprinted from Reference 101, with the permission of AIP Publishing) General classification of ALD growth according to GPC for each reaction cycle: a) linear, ideal growth, b) substrate-enhanced growth; c) and d) correspond to substrate-inhibited growth, respectively of types 1 and 2.

As a final note regarding the actual extent of ALD film conformality, many reports are silent as to how conformal exactly any given ALD process is. Conformality is assumed in the ideal case but not always proven, and real ALD processes usually have some degree of nonuniformity. In the past, this used to be due to the lack of straightforward, specialized test structures for conformality assessment, but this seems to be slowly changing [118, 119], and so in the future this situation can be expected to improve.

2.3. PULSED LASER DEPOSITION (PLD)

Pulsed Laser Deposition (PLD; historically also referred to as Pulsed Laser Ablation or Pulsed Laser Ablated Deposition) belongs to the group of Physical Vapor Deposition (PVD) techniques. In PLD specifically, a film is grown by transferring material from a solid target to a substrate, both of which are located in a vacuum chamber, facing each other. By firing short pulses of a high-power laser at the target, a plasma plume is repeatedly generated that travels outward towards the substrate, depositing small amounts of target material on top of it in the form of a thin film.

The PLD process was pioneered in the sixties by Smith and Turner, who used a ruby laser to eject plasma from powder and single crystal targets and deposit this plasma on a variety of substrates, generating thin films of varying quality [120]. Although it did not see widespread adoption immediately, the method gained serious momentum with its application to the growth of high-temperature superconducting films of YBCO by Dijkkamp *et al.* [121]. It is a valuable thin-film research tool primarily because of its capabilities for epitaxial growth (which happens when a grown film's crystal structure matches that of the substrate) and it has reached its maturity thanks to the addition of RHEED (Reflection High-Energy Electron Diffraction). RHEED is an in-situ growth monitoring technique which uses an electron gun and phosphor screen to monitor the PLD growth in real time[122].

2.3.1. FUNCTIONING PRINCIPLE

The PLD process starts with a pulsed laser. An important characteristic of this laser is that it needs to provide a stable output energy over the duration of an experiment, which can be several hours in some cases. The laser wavelength is important as well: one wishes to employ a wavelength for which common targets have large absorption coefficients. If the target is transparent to the laser, very little ablation will occur. Exciplex lasers (sometimes inaccurately called "excimer lasers") are a popular choice for PLD, as they require relatively little maintenance and often operate in the UV frequency range, at which many common ceramics and metals are opaque.

Downstream from the laser source, a set of optics is used to shape, attenuate (if needed) and focus the laser beam into a small spot of the target surface. The purpose of the optics is to ensure that this spot has uniform intensity and sharp boundaries. Past these optics, the laser enters the vacuum system. The vacuum is, in our laboratory, provided by the common pairing of a turbomolecular pump backed by a roughing pump. PLD chambers are often rated for ultra-high vacuum pressures near 10^{-9} mbar (10^{-7} Pa). PLD processes often take place not in vacuum but, among others, in inert noble gas atmospheres or, commonly for oxide growth, an O_2 partial pressure, so PLD chambers also are equipped with gas inlets. In these cases, common operating pressures are closer to 10^{-2} mbar (1 Pa).

When a laser pulse reaches the target surface, some target material is vaporized, and part of that is in turn ionized and expands in the form of a plasma plume. The target is often moving along its surface plane so that successive pulses ablate a large area rather than a single spot, thus avoiding the formation of deep holes in its surface. A short distance from the target, a substrate is placed, normally on a heated stage. When the plasma plume expands, it will reach the substrate, depositing small amounts of material on it. Normal operating pressures confine the plasma plume so that it does not travel all the way to the chamber walls and windows, and the film is deposited on the substrate mostly. This deposited material may desorb again, or diffuse along the substrate surface and take part in nucleation and growth of the new layer.

The area of the laser's footprint at the target surface can often be measured ex-situ with an optical microscope, and the laser energy can be measured as well, even if it is outside the chamber (in which case a correction is needed for the absorption through the chamber windows). The energy of a single pulse divided by the area it ablates is the laser fluence, which is an important process parameter. Other process parameters that are often critical are the laser pulsing frequency or repetition rate, the chamber gas type and pressure, the target-substrate distance and the substrate temperature.

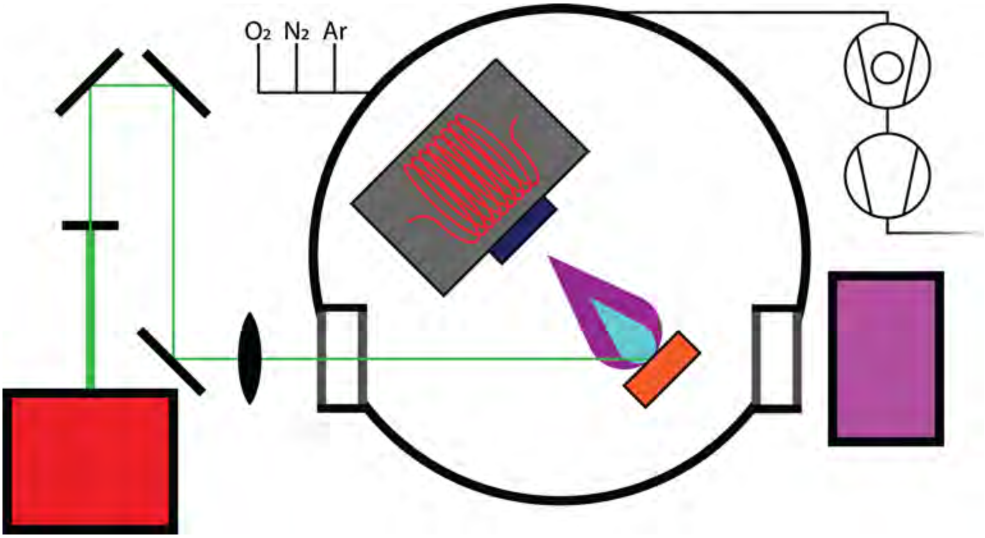

Figure 2.6: Top-view sketch of the PLD system used in this project. The laser beam (green) leaves the laser source (red box), crosses the optics and finally reaches the target (orange box) inside the vacuum chamber, where it generates a plasma plume. This plume travels towards the substrate (dark blue box) which is mounted on a heated stage. Also pictured schematically are the energy meter outside the chamber(pink box), the gas inlets and the pumping line on the top right.

2.3.2. SYSTEM

The system that was used (sketch in Figure 2.6) in this project uses a KrF exciplex laser (Lambda Physik COMPlex Pro 205 KrF) source which has a wavelength of 248 nm. This source is followed by a number of UV mirrors, a 60 mm^2 slit, and a converging lens with a focal length of 50 mm. The energy per pulse can be measured by a pyroelectric energy meter both before it enters the chamber and after it exits it at the opposite end (provided no target is in the way), enabling a straightforward correction for absorption in the windows.

The substrate inside the chamber can be heated using a resistive coil, measuring the temperature with a thermocouple. In this case the maximum operating temperature is 850ºC. Alternatively, the substrates can be heated to above 1100ºC with an IR diode laser (980 nm wavelength), in which case the temperature is measured with a pyrometer. The system is connected to oxygen, nitrogen, and argon gas lines, all of 5.0 purity (99.999%).

2.3.3. TARGET PREPARATION

The targets used in this project were pellets made in-house with standard solid-state synthesis equipment. For the $Si_{1-x}Ge_xO_2$ targets, the starting powders of SiO_2 α-quartz (99.995%, -40 mesh), GeO_2 (99.9999%), and $SrCO_3$ (99.99%), all purchased from Alfa Aesar, were weighed, then mixed with agate balls inside an agate mortar using a Fritsch Pulverisette ball mill at 150 rpm for 30 minutes. The mixed powder was then pressed uniaxially under 10 tons inside a 20 mm steel die. The resulting pellet was sintered in air at 900ºC for 5 hours and it was used as a target after that. This procedure is common in our group for the synthesis of ceramic targets.

For the metallic Sr target, dendritic strontium (MANUFACTURER) was rinsed with petroleum ether under an inert N_2 atmosphere, transferred to the 20 mm steel press and pressed under 10 tons as well, keeping it in a N_2 atmosphere when not in use as a target. Strontium metal quickly reacts with oxygen, water and carbon dioxide in the air to form its oxide, hydroxide and carbonate [123]. This makes the synthesis and survival of a powder-based Sr target very difficult. By using dendritic metal instead, handling becomes much easier while the target quality suffers in terms of roughness and density.

2.4. ATOMIC FORCE MICROSCOPY (AFM)

Atomic Force Microscopy (AFM) is a routinely used surface imaging method that was developed by Gerd Binnig in 1985 [124], and which allows the characterization of the topography of sample surfaces down to the nanometer resolution. AFM was closely preceded by Scanning Tunneling Microscopy [125](STM), the practical implementation of which netted Binnig and Rohrer the 1986 Physics Nobel Prize. AFM and STM belong to the category of Scanning Probe Microscopies (SPM). These techniques have in common that they rely on bringing a probe to a very close distance to the sample surface. This probe can be electrical, optical, or in the case of AFM, a sharp solid tip at the end of a cantilever. Once it is near (i.e. close enough to interact with) the sample, the probe is scanned across the surface plane while recording the relevant signal, so that a 2D picture can then be put together. For AFM in particular, the signal that is recorded is the tip deflection. This section contains an explanation of the method of operation for this technique, as well as details of the particular system that was used here, and remarks on the treatment of AFM data.

2.4.1. BASIC FUNCTIONING AND MODES OF OPERATION

The earliest analog to AFM would be the use of stylus profilers, which started in the early 20th century and continues to this day [126]. The basic idea in both cases is to bring a relatively sharp probe, which is called "tip" to interact with the sample surface. This tip is then scanned over the sample surface (or the surface is scanned under the tip, depending on the particular system) while maintaining contact, meaning that it will have to move up and down as it encounters peaks and valleys in the surface, respectively. This deviation, or deflection, in tip height, is recorded along the scan, allowing one to map the height (Z) as a function of in-plane position (X, Y). When one wishes to image very small features, a very sensitive feedback system is needed to avoid tip-sample crashes and loss of contact.

In AFM, this starts with placing the tip at the end of an elastic arm, commonly called a cantilever, which is itself at the end of a positioning system that uses piezoelectric actuators (see Figure 2.7a). By scanning the ensemble in contact with an uneven surface, one can imagine that the cantilever will twist and bend as the tip encounters features of the sample topography. It is then necessary to detect this bending and turn it into an electrical signal that the control system can use. Though there have been several proposed ways to do this, one of the most robust and the one used throughout this project is reflecting a laser off the top of the cantilever, in such a way that it reaches a four-quadrant photodiode. If the tip encounters a particle on an otherwise flat surface, the cantilever will bend upward, causing the reflected laser beam to move up in the photodiode. If the tip goes over a hole in the sample, the cantilever will bend downward, and the reflected laser will go down as well. The movements of the laser spot over the photodiode can be converted into voltage, which the control system uses in its feedback loop to manage the piezoelectric positioning elements and keep the probe close to the surface.

This is a rough explanation of how 1D scans are acquired. In its most common application, AFM can then generate 2D images by utilizing adapted raster scans (see Figure 2.7b), albeit different to those found in the old cathode-ray tube monitors: first, a line scan is taken, and we say that the direction of this scan is the "fast scan" direction. For ease of reference, I will call the fast scan direction X. A second scan is taken, on the same line in the reverse direction. These two scans are respectively referred to as "trace" and "retrace". After that, the tip moves a short distance perpendicularly to the direction of this fast scan; this movement takes place in the "slow scan" direction, or Y. At this point another trace scan is taken, parallel to the first, followed by another retrace. By repeating this process several times, it is possible to obtain a stack of parallel, contiguous line scans that together form a complete 2D image of the sample height.

2.4.2. SYSTEM AND MODE

AFM systems come in a wide variety of geometries, but in general they all have a stage, where the samples are placed, and what is commonly referred to as the AFM head: this part contains both the tip and the feedback system. The probes used in this project were made of silicon and they had an aluminum top reflective coating. Common values for their force constant were near 40 N/m, and their resonance frequency, though it varied as measured from one tip to the next, was close to 300 kHz. The system used was a Dimension Icon microscope by Bruker, on damped supports and placed in a housing to reduce ambient noise. Measurements were performed in air at room temperature.

The system has been used exclusively in tapping mode for this project. In this mode, the tip is brought to a short distance from the sample surface, but not in physical contact with it. Then, the cantilever is oscillated at a frequency close to its resonance frequency. Interactions between the tip and the sample change this resonance frequency which, as the actual oscillation frequency remains constant, results in changes to the am-

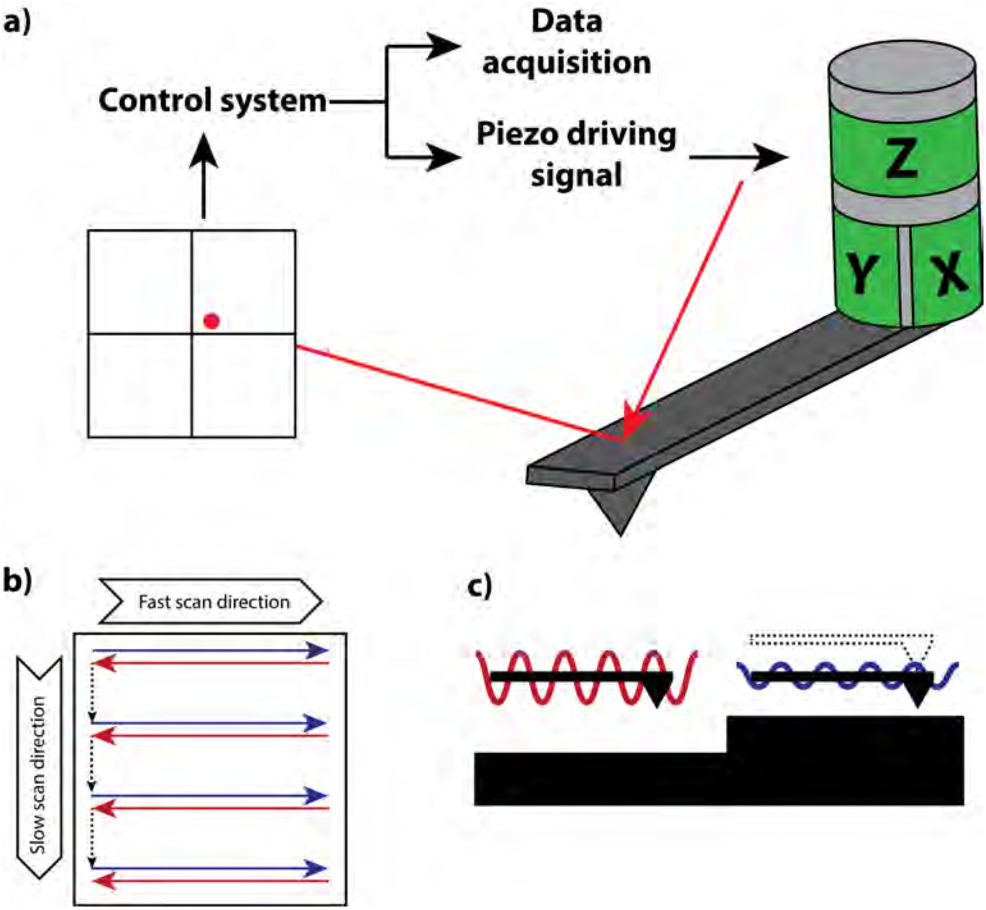

Figure 2.7: a) Sketch of a common AFM system principle. A laser (red) is reflected off the cantilever (dark grey); the reflected spot position is tracked by a photodiode and fed into the control system, which uses it to adjust the piezoelectric actuators (green) and record the tip oscillation amplitude and phase. b) AFM rastering pattern. The trace scans are indicated by blue arrows, whereas the red arrows represent the retrace scans. The dashed lines are probe motions in the slow scan direction, where no data is recorded. c) Basis of the AFM tapping mode. When the distance between the tip and the sample is reduced (e.g. the sample crosses a surface step as in the figure), so is the oscillation amplitude [127]. The dotted lines show the new probe height that is required to maintain constant amplitude.

plitude (and phase) of these oscillations [127] (see Figure 2.7c for a sketch). The control system of the AFM is able to detect this change and adjust the probe height so that the amplitude (or phase) of the oscillations *also* remains constant. The probe height is thus recorded as it changes along the scans, giving the topography of the surface. The tapping mode allows relatively fast scans while avoiding strong forces between the sample and the tip, meaning that both of them are less damaged than in contact mode.

2.4.3. IMAGE TREATMENT

Image treatment is an important part of research involving AFM. It is unusual to find exclusively raw AFM data in published media, and this is the case in this thesis as well. For this reason, it is appropriate to dedicate a subsection to the treatment of the AFM images that is normally done after capturing them. Here an explanation will be given of the most commonly used methods to treat images from AFM. The purpose of the treatment depends largely on the particular method, so this shall be discussed individually. A more complete explanation, including methods not used in this project, can be found in Chapter 5 of Eaton and West's comprehensive textbook [128].

The first step many images undergo is row alignment, sometimes called horizontal levelling. This is required as consecutive horizontal scans often have some stagger between them; in other words, even if a surface is very flat, it is possible that one scan and the next are slightly offset (see Figure 2.8a). With the horizontal levelling, each consecutive scan is individually offset up or down. This levelling step (and other types of image correction) can, however, introduce new artifacts to the image if not done carefully. The most common way this can happen is when there are particles present in the imaged area. In that case, under non-optimal imaging conditions a particle will generate very characteristic streaks in the horizontal direction which interfere with the horizontal levelling afterwards. An easy way of avoiding this is to start the image treatment by applying a mask to the image which selects particular "defect" regions (based on height difference and defect radius), in this case the particles themselves, that can be left out of the image treatment later on.

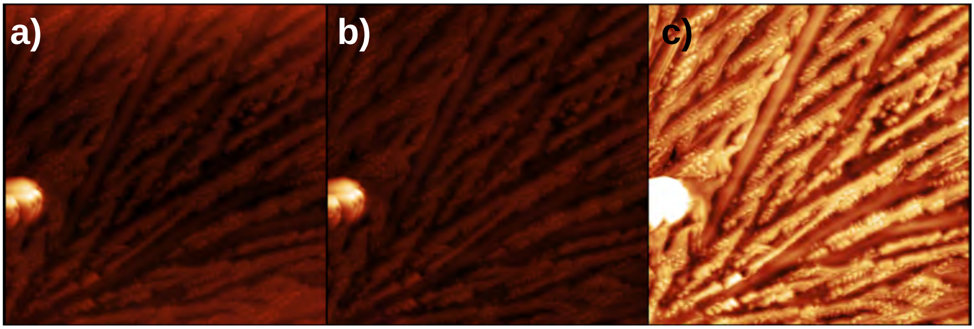

Figure 2.8: Steps in the processing of AFM data (scales removed for simplicity). a) AFM image as recorded. b) Image after background subtraction. The large particle on the left was masked out for this step. c) Image after scale correction. The particle now appears saturated, but the new scale offers better contrast for the rest of the image.

Additionally, a polynomial background subtraction takes place. This entails applying an offset to every pixel of the image. The offset is a function of position in X and Y, and this function can be a polynomial of arbitrarily high order in X and Y. Choosing a zeroth or first order polynomial results in an offset that is simply a flat plane, but for higher orders it becomes a curved surface. One must consider what exactly it is that is being removed from the picture or, in other words, if the corrections are removing a measurement artifact or a physically meaningful feature of the surface. With a first order polynomial, it is possible to correct sample or stage tilt. With a second order polynomial, the greater part of sample curvature can be eliminated. Additionally, it is not uncommon for curvature artifacts (sometimes referred to as *bowing*) to appear in the fast scan direction which are reasonably countered with a parabollic offset. As a rule of thumb, corrections of third and higher order should only be applied if there is a clear, physical reason to do so, as the subtraction of a high enough order polynomial background will unphysically flatten any image.

Finally, before presenting data it is customary to adjust the height scale bar to show height zero at the lowest point of the image, and to end at the highest point of interest. Normally this means that big particles present in the image will exceed the scale value and appear saturated, but that important features will be within the color range of the scale. For ease of comparison, normally images presented together of analogous samples are given with scale bars of the same size. Adjusting the scale does not technically change the data being presented, but it is included here because it is used to emphasize some features at the expense of others (see Figure 2.8c).

2.5. X-RAY DIFFRACTION (XRD)

X-ray diffraction is a physical phenomenon rather than a technique in itself. In this section, a number of X-ray measurements are explained, also including X-ray reflectometry. These measurements were all performed in thin-film X-ray diffractometers, described in further detail below. Again, for a more detailed description of the physics and methodology behind these (and other) X-ray measurements the reader is directed to the textbooks by Als-Nielsen and McMorrow [129], and by Pietsch, Holý and Baumbach [130].

2.5.1. X-RAY DIFFRACTION

X-ray diffraction can be described as the interference between X-ray photons scattered by a sample. For the purposes of our discussion here, we limit ourselves to the kinematical approximation of X-rays which, in short, makes the assumption that the incident X-ray beam is diffracted by the sample once and detected afterwards. We also assume that this scattering is largely elastic, so the wavelength of the diffracted beam is the same as that of the incident beam.

In the electromagnetic spectrum, the X-ray regime is located between the extreme ultraviolet ($\lambda \approx 1$ nm, E≈1 keV) and gamma rays ($\lambda \approx 0.01$ nm, E≈100 keV). At these energies, most of the scattering is done by the electrons in the sample. The strength with which an electron scatters is given by its scattering length, which for free electrons is independent of the photon energy and is named the Thomson scattering length.

The scattering length of an atom is found by adding up all of its electrons' scattering lengths, times a phase coefficient that depends on the electron density and the reciprocal vector Q, which is the difference in wavevectors between the scattered and the incident beams. The scattering length of a group of atoms is similarly found by adding up each atomic contribution, times a phase coefficient that depends on the atomic positions and again Q.

For a molecule or an atomic cluster, this is a sum of relatively few terms. However, for a macroscopic sample, there may be of the order of N_A ($\sim 10^{23}$) atoms, which would result in a difficult calculation save for two extreme cases: in the first one, the atoms are completely disordered so on average their contributions cancel out; we call this an amorphous material and in the simplest descriptions it does not diffract with measurable strength. In the second case, the atoms are ordered in crystalline arrays: this means that they are organized in a unit cell, which can be roughly of the size of a molecule, repeated in space at periodic intervals in all three dimensions. Then the diffracted intensity can be calculated by summing the contribution from each cell (molecule case), together with its phase coefficient, which is simplified by the periodicity of the crystal lattice.

In practice, the consequence of this treatment is that, when diffracting X-rays off of a crystalline sample, we will sometimes see constructive interference, which constitutes intensity peaks, depending on the angle of incidence of the primary X-ray beam and the angle at which we measure the intensity of the diffracted beam. These peaks will have relative intensities and angular positions that depend on the structure of the sample being measured. Each peak can be associated to a lattice plane (identified by its Miller indices: h, k, and l) of a crystal lattice, but not all planes diffract with the same strength and some may not diffract at all: these are systematic absences. It is easy to calculate approximate diffraction patterns for a crystal with a certain structure, but calculating a structure from a diffraction pattern is a lot more difficult. This is because the phase information of the diffracted beam is usually lost during the measurement.

In this thesis, X-ray diffraction is not used to resolve structures directly from measured diffraction patterns. Instead, we measure X-ray spectra while already having an approximate idea of which phases might be present in the sample. Then, the intensity peaks are compared with the simulated peaks for those phases, and assigned accordingly. An important tool to this end is Bragg's law, given by:

$$2d_{hkl}sin(\theta) = n\lambda \tag{2.1}$$

where d_{hkl} is the interplanar spacing for crystal plane (hkl), θ is half of the angle between the incident and primary beam, n is the diffraction order (natural numbers above zero) and λ is the wavelength being used in the diffraction experiment.

This law relates the interplanar spacing for a given family of planes to the angle between the incident and primary beam that is required in order to obtain constructive interference when diffracting X-rays of a given wavelength off of that plane, assuming the sample is oriented properly (i.e. the plane normal must bisect the supplementary of the 2θ angle). Bragg's law does not give information about peak intensity, as that would require details of the atomic types and positions in the unit cell, but it helps relating a measurable angle directly to an interplanar distance. At this point it is important to make a clear distinction between the diffraction (or scattering) plane, which is a plane in space that contains both the incident and the detected beam, and a plane which is said to be "diffracting", which is made up of points of the sample's crystal lattice.

In the particular case of thin films, X-ray data can also have encoded in it information about properties of the film other than its crystal structure. This appears as small intensity modulations, best observed around diffraction peaks of the film phases (Laue fringes), and at small angles, close to the critical angle for total reflection (Kiessig fringes). Because in this work many of the thin-film samples are amorphous, we focus here on the analysis of the reflected intensity at low angles.

2.5.2. X-RAY REFLECTION

For the simple case of the interface between air and a bulk material, the reflected intensity reaches a maximum near the critical angle for total external reflection, and then decays quickly at larger incident angles. In this range, it scales as Q^{-4}, which itself is proportional to $\sin(\theta)^{-4}$, or just θ^{-4} at small angles. When there is a thin film present there are two interfaces that play a role in reflection: between the film and the air, and between the substrate and the film (this goes on for the case of several films on top of one another). X-rays reflected from the bottom and top interface interfere, and this results in the appearance of evenly spaced intensity oscillations, the Kiessig fringes, superimposed on the original polynomial decay. These oscillations themselves decay in amplitude at larger angles. The periodicity of the oscillations is determined by the film thickness, and the decay constant for the oscillation amplitude depends on the interface roughness. The critical angle (θ_c) can be used to estimate the scattering length density (SLD), with the following relation:

$$SLD \approx \frac{\pi {\theta_c}^2}{\lambda^2} \tag{2.2}$$

The SLD can be roughly understood as the electron density of the film, and given its elemental composition this can be turned into mass density. θ_c is the critical angle, understood as the angle between the source and the *surface*, and λ is, again, the wavelength used in the experiment.

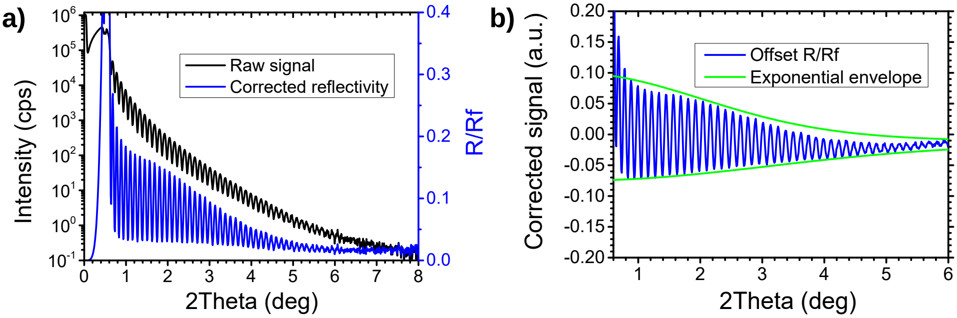

Figure 2.9: a) Raw X-ray reflectivity plotted against reflected angle (black) and the same scan but with the R_f (Q^{-4}) envelope removed (blue). b) R/R_f curve, normalized, offset and leveled with a first order polynomial. The amplitude of the oscillations decays exponentially in Q, as shown by the green delimiters.

2.5.3. SYSTEM: THE PANALYTICAL X'PERT PRO MRD

For most of this work we have used a Panalytical X'Pert Pro MRD (Materials Research Diffractometer), which is a four-circle diffractometer. This system is sketched in Figure 2.10. It consists, first, of an X-ray source, which in our case is a copper tube. This is a vacuum tube containing a heated tungsten filament cathode and a copper anode. Between these electrodes there is a large bias, 40 kV in our system, and as a result electrons that are thermally emitted from the cathode are accelerated towards the copper anode. The accelerated electrons may remove core electrons of atoms in the anode, which leads to the decay of electrons in an outer shell into the newly generated empty states, accompanied by the emission of photons of energies, and thus wavelengths, characteristic to the anode material. Downstream from the source we place a four-bounce Ge(220) hybrid monochromator to filter out unwanted wavelengths so that we can isolate and use the Cu Kα emission line[1], which has a wavelength of 0.154184 nm.

After the monochromator, and sometimes an incident slit, the X-ray beam reaches the sample, which in our system is normally glued to a stage with six degrees of freedom. They are listed here in hierarchical order. Three degrees of freedom are rotational. The ω motor rotates the sample stage around the axis perpendicular to the scattering plane. The χ (sometimes named ψ) motor rotates the stage around the axis perpendicular to the ω rotation axis and the sample normal. The ϕ motor rotates the sample about its surface normal. The remaining three degrees of freedom are translational, with the X and Y motors moving the sample within its plane and the Z motor moving perpendicular to the sample surface. A graphical, and perhaps less confusing, summary can be found in Figure 2.10.

After the sample, the beam arrives to the detector optics, mounted in the 2θ motor, which can move the detector along the scattering plane. Together with the sample's three rotational degrees of freedom described above, this makes four angles, giving the "four-circle" name to the diffractometer. In our case the diffracted beam optics may begin with a narrow receiving slit, which is then followed by a Soller slit. This slit is composed of many parallel metal plates, which are oriented in such a way that the diffracted beam needs to also be parallel to the plates in order to pass, thus eliminating off-angle components and collimating the beam. After these two elements, the X-ray beam arrives to the detector itself. In our system this is either a point detector or a PIXcel3D area detector. This area detector is composed of a square of 255x255 channels, which can record intensity separately.

2.5.4. X-RAY DIFFRACTION MEASUREMENTS

In the measurements performed during this project, X-ray photons arriving to the detector are counted as one or several of the motors described above are scanned. The number of photons per position of the motor is plotted in a histogram, which is known more commonly as a diffraction "scan" or "pattern". It is common to divide the number of photons, or counts, by the time spent at each step, resulting in a diffracted intensity, in counts per second. This allows us to more easily compare different measurements from the same setup. Measurements from different setups can have wildly different intensities, and many times the results are reported simply in "arbitrary units" (a.u.), hiding their

---

[1] "Kα" uses the Siegbahn notation for emission spectra. See Reference 131 for the correspondence to IUPAC nomenclature.

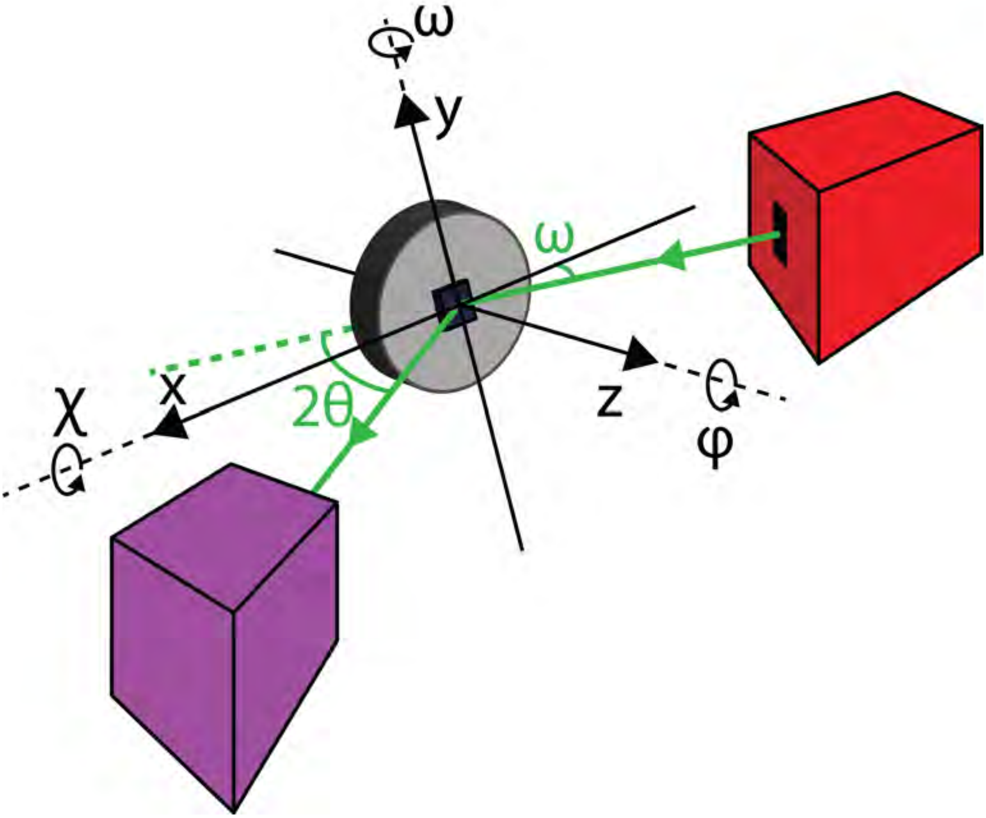

Figure 2.10: Sketch of the degrees of freedom of the goniometer used in this thesis. The X-ray beam (gren) is shown departing from the source (red), interacting with the sample (dark blue) and reaching the detector (violet). The diffraction plane here is that which contains the two green arrows, and does not necessarily coincide with the XZ plane. Note that the ω motion is displayed twice, and that the 2θ motor positions the detector with respect to the primary beam only, independently of the other degrees of freedom, which belong only the sample.

magnitude altogether.

It is also worth noting that in some measurements, the relevant signal may appear at very different intensity scales. This is the case when observing Kiessig fringes (as explained above), or in measurements that show both film and substrate diffraction peaks. In these instances, it can be useful to plot the data in logarithmic, rather than linear intensity scale. In some cases, like in texture measurements (or reciprocal space maps, not discussed here) different motors are successively scanned, resulting in data which is more easily viewed in 2D maps than as a bundle of 1D scans. The intensity is then shown with a color plot.

SYMMETRIC $2\theta/\omega$ SCANS

In a symmetric $2\theta/\omega$ scan, the detector often uses only the middle 5 channels in 0D mode (that is, all channels get integrated together into a single angle) preceded by a slit, or a point detector is used instead. These settings give good resolution and they are appropriate if relatively strong intensities are expected. The 2θ angle is scanned within a certain range, and the ω angle is also scanned following the reflection condition. In this way, as the scan proceeds it probes the lattice planes of progressively smaller spacings (see Equation 2.1), but which are all oriented in the same direction. This makes it very useful for certain kinds of epitaxial thin films, but it can also be very sensitive to the substrate Bragg peaks, which are orders of magnitude more intense than the film signal. If the film and substrate peaks are sufficiently spaced in 2θ, this does not necessarily constitute a problem, but if the opposite is true, or if the film orientation is not favorable, a different type of measurement is required.

COPLANAR GIXRD

GIXRD stands for Grazing Incidence X-Ray Diffraction. For this type of measurement, the 2θ motor is also scanned but in this case ω is kept at a value close to, but larger than, the film's critical angle for total external reflection. The result of this, in short, is that as 2θ is scanned, both the spacing and the orientation of the probed planes changes, meaning that in principle GIXRD should be used in samples formed by crystallites with uniformly random orientation. The main advantages of this technique are that, due to the small incidence angle, and the coupling between spacing and orientation of the diffracting planes, the recorded signal comes largely from the thin film, eliminating the substrate contribution. However, because of the requirement for the lack of preferential orientation, this type of scan often achieves fantastically low diffracted intensities. In the lab, we address this by using the detector in 2D scanning slit mode, which means that we remove the receiving slit and we use the entire width of the detector, with each channel counting for a different value of 2θ. This adds some off-angle noise but it also increases counting time for each 2θ step by up to a factor of 255 compared to a similar 0D receiving slit measurement. Even then, diffraction peaks are very weak and rather long counting times are required.

TEXTURE MEASUREMENTS

In texture measurements, the 2θ and ω motors are locked at the position for a particular [hkl] reflection, whereas ϕ and χ are scanned. Each step in χ, up to 90º, is followed by a full 360º scan in ϕ. In this way, while searching for a particular reflection, the sample orientation goes through an entire hemisphere. The intensity is plotted in an equal-area projection which is often referred to as a "pole figure". This pole figure shows, for the relevant family of reflections, the orientation in space of their corresponding lattice planes, giving key information on the presence and nature of grains and domains in crystalline samples. For texture measurements, we use a point detector instead of the PIXcel3D. The signal to be measured is rather weak, so there is a number of changes in the configuration, like the use of a single-bounce monochromator before the detector. The incident optics include slits but no monochromator, and the source is used in point focus, which means that the X-ray beam has a larger footprint and intensity.

2.5.5. X-RAY REFLECTOMETRY

X-ray reflectometry (XRR) measurements are quite similar to a regular $2\theta/\omega$ scan, with the peculiarity that the angles scanned are normally much smaller, between 0º and 8º, which is where we typically find strong enough intensity oscillations that we can use to extract information about a thin film. Very high intensities are sometimes recorded in this method, either because the direct beam is included in the measurements or because the region near the critical angle is often very intense as well. This can result in blinding, and sometimes permanent damage, to a point detector if it does not have automated slits, which means that in some of our measurements the lowest angles are either not included in the scan or are measured separately using a thin (0.1 mm) copper attenuator at the source, which makes the primary beam weaker approximately by a factor of 100.

The initial analysis of XRR data described earlier in this section provides estimates for some of the sample parameters in simple cases. However, when dealing with more complicated cases, the pattern quickly becomes more difficult to analyze. If the layer has a lower SLD than the substrate, it is possible to observe more than just one critical angle. Having a stack of different layers of different thickness results in superimposed oscillations with different periodicity and possibly different amplitude and decay constants. In practice, analyzing these measurements requires building a model. This means that the sample parameters are only indirectly determined.

There are several ways to do this, but they often have common fundamental traits: a model is used that reflects the most relevant sample properties, then a XRR spectrum is simulated using this model. The simulated spectrum is compared to the measured data with the help of some error metric, and then the model parameters are gradually modified in a way that reduces the difference between real and simulated data. When a minimum in the error metric is reached, the fitting stops and one needs to see if the model is a close match to the real sample.

For this project we have used the GenX software[132] , which is a free, Python-based fitting tool for X-ray and neutron reflectivity. GenX uses models that include layer thicknesses, densities and roughnesses, as well as other variables, such as the primary beam intensity profile, sample size and background intensity. With these, it creates a profile of scattering length density against sample depth, and this is used to work out the simulated spectrum. The figure of merit (to be minimized) used here is the difference between the logarithms of the measured and simulated intensities, integrated over the whole spectrum and normalized with the scan length. This figure of merit is effective in comparing scans with large dynamic ranges, such as those commonly found in XRR. GenX uses a genetic algorithm, which means that at any point it is considering of the order of 100 different models, and after one "generation" it takes only the most successful models of the current set and uses them to create the following set of candidates. This is often successful in avoiding stagnation problems that can occasionally be found in other approaches such as the segmented fit.

As with other model-based parameter determination methods, it is very difficult to determine the error associated to these parameters. For relatively simple heterostructures, the thickness resolution is determined by the maximum 2θ of an XRR scan, and the error in film density can be propagated from the uncertainty in the critical angle for total external reflection, which can be the step size of the scan. In the case of even slightly more complicated samples, the number of parameters quickly increases, and these methods no longer work. Fitting software is often able to provide error bars for each parameter. Alas, these can be unphysically low numbers which are more related to fitting statistics of the model. This is why XRR fitting results are to always be treated with caution, especially when no comment is found about error bars or significant figures. Actual determination of parameter errors requires validation with an additional, direct observation, for instance Atomic Force Microscopy or Transmission Electron Microscopy.

2.6. ELLIPSOMETRY

2.6.1. SPECTROSCOPIC ELLIPSOMETRY

Spectroscopic ellipsometry is an optical technique that is capable of determining film properties such as the thickness, refractive index and absorption coefficient by using polarized light. What follows is a brief description of Rotating Analyzer Ellipsometry (RAE), but a better one is given, among others, in the textbook by Fujiwara [133]. The technique itself relies on a source of monochromatic, polarized light, that is, with X and Y electric polarizations, with a known phase shift (which can be zero, but is not always). In the measurements, this light is reflected off the sample surface, passed through a rotating analyzer and collected in a detector. Transmission mode measurements exist as well but we do not deal with them here as they require transparent samples. Because of the reflection geometry, it is more common to refer to the two orthogonal polarization vectors as s and p, with the s polarization parallel to the sample surface and the p polarization contained in the plane defined by the incident and reflected beam axes.

When light reaches the air-sample interface, part of it is reflected and part of it is transmitted. The transmitted component travels within the sample, suffering attenuation dictated by the sample's absorption coefficient, until it reaches the next interface. At that point, again some of it is reflected back and some of it is transmitted. It can quickly be seen that there is no limit to how many times light can be reflected back and forth within the sample before it escapes and reaches the detector. Due to absorption in the material, light that is reflected more times will have vanishingly smaller intensity; likewise, due to its longer optical path, it will also accumulate a phase lag that depends on the refractive index and thickness of each layer. Therefore, the reflected beam will have encoded in it information about thicknesses, refractive indices (n) and absorption coefficients (k). The observable that is usually referred to in ellipsometry is the complex reflectance quocient (ρ) between the incident and reflected beams:

$$\rho = \frac{R_p}{R_s} = \frac{|R_p|e^{i\phi_p}}{|R_s|e^{i\phi_s}} = tan(\Psi)e^{i\Delta} \tag{2.3}$$

Where R_p and R_s are the complex reflectances for the p and s components of the beam, later expressed in polar notation, and Ψ and Δ are quantities calculated by rearranging the factors of this polar notation. tanΨ is the modulus ratio between R_p and R_s, and Δ is their phase shift.

A point that is often not stressed enough is that the detectors used in ellipsometry can measure intensity alone (which is a real number. An intensity ratio is also real), and thus the complex reflectance quocient is not *actually* an observable quantity in RAE. Determining the reflected amplitude ratio between the s and p reflected waves is trivial with a rotating analyzer, which allows us to isolate each of the two polarizations and measure them one after the other. Determining the phase shift between them without using a phase modulator is less obvious, but it is how RAE works. In a few words, while rotating the analyzer angle (A) over half a turn, the measured intensity for a given wave will show an approximately sinusoidal behavior with A. Intensity extremes appear at A = Ψ. The intensity ratio between maxima and minima (not to be confused with the intensity ratio between the s- and p-components) gives Δ, so a ratio of 1 (constant intensity) indicates circular polarization, or $\Delta = 90^o$, and an intensity ratio of infinity indicates linear polarization, or $\Delta = 0^o$. Elliptical polarization, which as the technique name indicates is the one present most of the time, will have values in between. Ψ and Δ are the actually recorded measurement data.

2.6.2. SYSTEM: THE J.A. WOOLLAM CO. WVASE

The system used in this project was a vertical spectroscopic ellipsometer. Unlike laser ellipsometers, which are commonly locked to a single wavelength, spectroscopic ellipsometers use a polychromatic light source. In our case this is a Xe discharge tube followed by a grating monochromator and polarizing optics. Most measurements were done at detector angles of 70º and 75º, and with wavelengths spanning from 300nm to 1700nm. Other than the rotating analyzer, a variable aperture and the detector, no other optics were used (see Figure 2.11). The sample stage is simpler than that described in Section 2.5, and can be manually adjusted for ω, χ and Z.

2.6.3. FITTING THE DATA

In spectroscopic ellipsometry, Ψ and Δ are collected for many different wavelengths, and normally for a few different incident angles close to the Brewster angle. Then, a model is built in a similar way to the ones used in XRR: several layers are specified including their thicknesses and optical properties, generating a plot of n and k versus depth (for any given wavelength). Then a theoretical Ψ and Δ are plotted against wavelength, per incident angle. In the work presented here, the free parameters of the model were optimized by fitting the simulated Ψ and Δ to the experimental results using a Levenberg-Marquadt (damped least squares) algorithm.

Because this procedure relies on optical parameter contrast, there are materials, such as Si and SiO_2, which are very easily distinguishable even though they are almost identical when observed with XRR. However, there is an added limitation to SE: it only works in films

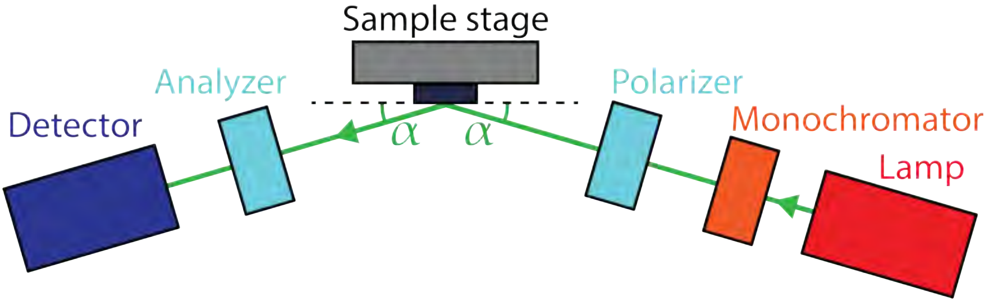

Figure 2.11: Sketch of the WVASE system, viewed from the top. The p polarization vector is in the page plane, and the s polarization is perpendicular to the page. The incident and reflected angle are kept equal and constant (α)during a single wavelength scan.

as thick as about 5 times the light penetration depth, due to absorption losses in the signal. Many materials, including metals, are opaque near the visible range, so films of these materials can only be measured if they are extremely thin. Parameters determined using SE have generally unclear uncertainties, much like in XRR. Also like in XRR, the treatment of interface roughnesses is not straightforward, especially when roughness length scales are much larger than the radiation wavelength.

2.7. ELECTRON MICROSCOPY

The first electron microscopes were built in the 1930s with the aim of surpassing the resolution of optical microscopes, which is, following Rayleigh's criterion, of the order of the wavelength of the light being used. As electrons can be accelerated to hundreds of keV, this potentially gives them a wavelength of a few picometers, well below visible or UV light, leading to enhanced resolution imaging. In the systems used for this thesis, we can comfortably reach acceleration voltages of 15 kV, which results in resolutions of the order of 0.1 Å. This section is intended to be a brief, concise introduction to the types of measurements that will appear later in this thesis, without going into extensive detail about the underlying physics behind them. For that, readers are directed to the book by Egerton [134].

There are several configurations for electron microscopes, and it is not unusual for a single system to be able to perform measurements in more than one configuration. All electron microscopes have fundamentally similar designs, with a vacuum system that includes the electron source, electromagnetic lenses and the sample stage, as well as detectors. In some cases, the electron beam is made to be rather sharp (we say that the spot size is small) and rastered, or scanned, over the sample surface, composing full images out of several scans, similarly to AFM. In other cases, the beam is kept in place, much like in common optical microscopes. Perhaps the most intuitive distinction between different measurements is *what* precisely is being detected. Here follows a very brief rundown of some types of electrons and radiation that are used in this thesis, and it is schematichally summarized in Figure 2.12. In this project we have used a Fei NovaNanoSEM 650 microscope for SEM and EBSD, and a Fei ThemisZ FEG (S)TEM for STEM measurements.

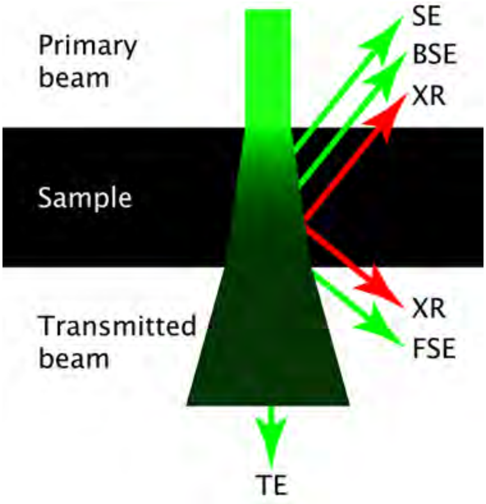

Figure 2.12: Simplified sketch of the interaction between the electron beam and a sample. On the top side of the sample, secondary electrons (SE), back-scattered electrons (BSE) and characteristic X-rays (XR). On the bottom side, transmitted electrons (TE) and forward-scattered electrons (FSE) and more characteristic X-rays. Not all outgoing electron and radiation types are mentioned in the figure.

Secondary and back-scattered electrons usually come from a small interaction volume close to the sample surface, and they are detected on the same side of the sample that the primary electron beam comes from. These are the most common signals that are used in Scanning Electron Microscopy (SEM), and they respectively carry information about sample topography and composition (back-scattered electron intensity depends strongly on atomic number in the sample).

Transmitted electrons are at the center of Transmission Electron Microscopy (TEM) and Scanning Transmission Electron Microscopy (STEM). These electrons are the part of the primary beam that gets transmitted through the sample, which therefore needs to be below ~ 100 nm in order to avoid excessive attenuation. Although occasionally grouped together, transmitted electrons can carry different information as well. We say that the transmitted beam forms an illumination cone after exiting the sample. A detector placed in the axis of the cone can take Bright-Field (BF) images, whereas by placing a ring-shaped (annular) detector outside of this cone it is possible to measure forward-scattered electrons in Annular Dark Field (ADF) and High-Angle Annular Dark Field (HAADF) imaging. The HAADF mode is particularly useful for providing images with atomic resolution which *also* have contrast in atomic number.

Diffracted electrons from the primary beam can be found when measuring samples with some crystallinity, and these electrons are used in Electron Back-Scatter Diffraction (EBSD) and Transmission Electron Back-Scatter Diffraction (t-EBSD). These electrons can form a diffraction pattern that carries information about the crystals in the sample. If the spot size is close to, or below the size of the crystalline domains, these diffracted electrons can be used to determine the structure and orientation of each domain, which can in turn be represented as a pole figure or an inverse pole figure, which in practice is an orientation map.

X-rays are commonly generated in electron microscopy measurements as well. Acceleration voltages of 10-30 kV are already enough to generate characteristic X-ray fluorescence out of most known elements, and an X-ray spectrometer can detect this fluorescence in a technique known as Energy-Dispersive X-ray Spectroscopy (alternatively EDS or EDX). The analysis of spectra thus collected can help identify and quantify elements in the sample; again, this can be turned into a composition map by scanning the electron beam and collecting spectra at different points of the sample.

3

ALD GROWTH OF SiO_2 AND GeO_2

The growth of thin films of SiO_2 and GeO_2 is the first step to the realization of nanostructures of their functional crystalline polymorphs. In this chapter, the ALD growth of SiO_2 is put in its well-established context, as a prelude to the significantly less abundantly reported ALD growth of GeO_2. GeO_2 amorphous thin films are themselves interesting for electronics applications, so this chapter next addresses the optimization of the GeO_2 growth. Finally, SiO_2-GeO_2 multilayers with increasing periodicity are also grown, showing the thickness resolution of the ALD process.

3.1. BASICS OF SiO_2 ALD GROWTH

As one of the most important materials involved in silicon electronics, SiO_2 is unsurprisingly one of the most widely studied materials in the ALD literature, with several approaches that have been studied and optimized over the years [135]. The first reports of SiO_2 grown by ALD date back to the early 1970s, and many of them utilize halides, such as SiH_2Cl_2 [136] or $SiCl_4$ [113, 116, 137–139], as a silicon source. Sometimes they include a catalyst such as pyridine [140, 141] or ammonia [142] (both through similar reaction mechanisms) to reduce the process temperature and exposure times. This allows the use of a wider range of materials and makes the process more appealing from a commercial standpoint. The base-catalyzed processes faced similar problems with the hydrochloric acid that was released during the process, as both pyridine and ammonia tended to complex it, remaining adsorbed on the surface and potentially interfering with later ALD cycles.

Later on, halogen-free precursors were investigated, such as $Si(NCO)_4$ [143, 144] or $CH_3OSi(NCO)_3$ [145, 146], which can be used at lower temperatures than their halide counterparts. Currently, it is common to use compounds of silicon with organic ligands. These organometallic precursors also have the advantage of not releasing hydrogen halides

---

This chapter includes content published as:
Jordi Antoja-Lleonart, Silang Zhou, Kit de Hond, Sizhao Huang, Gertjan Koster, Guus Rijnders, Beatriz Noheda. Atomic Layer Deposition of SiO_2-GeO_2 multilayers, *Applied Physics Letters*, **2020**, *117*, 041601.

as a reaction product, meaning that no salts are formed with amine catalysts anymore, improving the results over the $SiCl_4$ process. This is the case for ALD using tetraethyl orthosilicate (TEOS) and water, catalized by ammonia [147]. This process, which requires relatively large exposures, was elegantly taken one step further by Bachmann *et al.* by switching the TEOS for 3-aminopropyltriethoxysilane [148]. In doing that, they replaced the ammonia, which is corrosive, by an amino group which was already bound to the precursor molecule. The main disadvantage of this method is that it needs an additional oxidation step with ozone to remove the 3-aminopropyl group (see Figure 3.1). On the other hand, it does yield high growth rates with a precursor that is relatively stable, all while simplifying the gas pulsing scheme, avoiding corrosive compounds, and preventing salt formation at the sample surface.

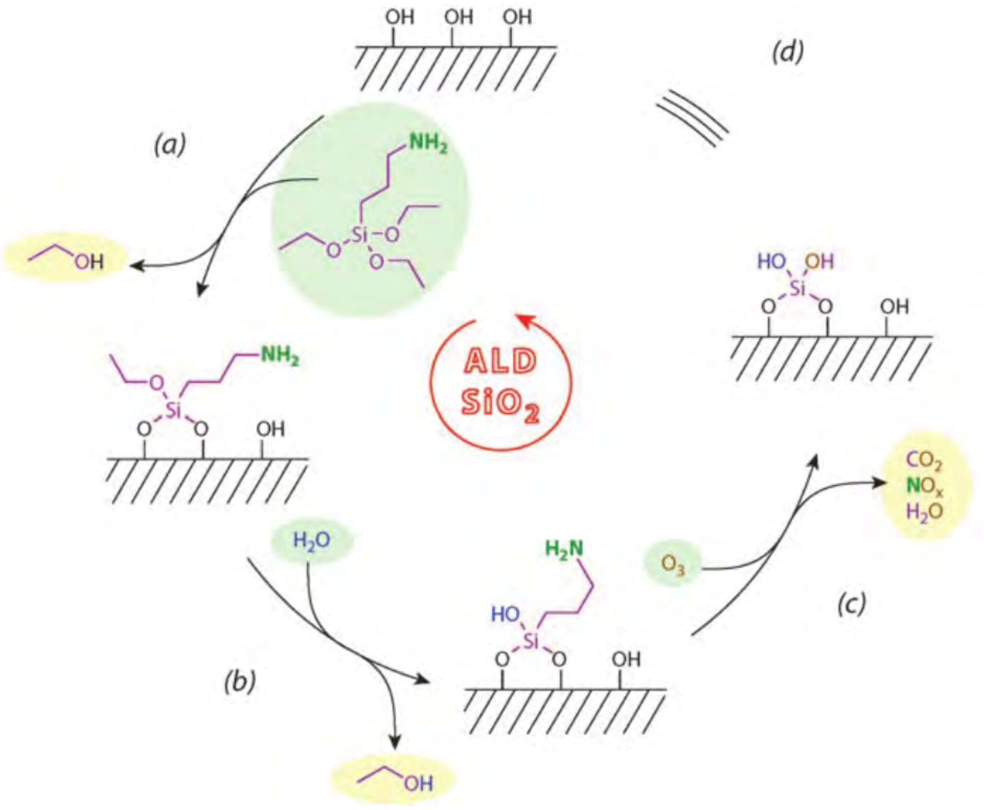

Figure 3.1: Self-catalytic ALD scheme. In steps a) and b), the ethoxy groups in the precursor are exchanged, respectively, with surface hydroxyls and water molecules. These steps are catalyzed by the side alkylamine. Step c) has the last side chain oxidized, leaving an OH-covered surface ready for the following cycle. (Reproduced from Reference 148 with permission from John Wiley and Sons. Copyright © 2008 WILEY-VCH Verlag GmbH & Co. KGaA, Weinheim)

The current landscape of SiO_2 ALD is dominated by alkylaminosilanes and related compounds. Examples of this are tris- and bis(dimethylamino)silane [149, 150], or cyclic azasilanes [151], all of which incorporate amine groups as part of the ligands. It is also possible for some precursors to contain more than one Si atom, which can succeed in increasing the GPC and purity of the films [152].

Many of these aminosilanes react very weakly, or not at all, with water at room temperature, so there is a need for stronger oxidizers, such as ozone [153]. Some of the currently relevant compounds in the field are compared in References 154 and 155 . In the first, experimental and theoretical arguments are given that show bis(alkylamino)silanes to be more effective than their tertiary counterparts. In the second, regular (thermal) and plasma-enhanced ALD results are compared for a single precursor. Both publications also provide a look at parameters such as GPC, refractive index, water contact angle and nonuniformity in thickness (or, conversely, conformality), for a range of temperatures and exposure times. At the time of writing this text, it appears that the next generation of SiO_2 precursors may comprise mono(alkylamino)silanes, which might enable even lower temperature processing with high growth rates [156, 157].

Of few compounds mentioned so far, bis(diethylamino)silane, referred to from here on as BDEAS, is of special interest to this project. BDEAS, sometimes sold under the commercial name SAM-24, is a liquid at room temperature, but it has a reasonably high vapor pressure of 4 kPa at 70°C [158]. Its optimal growth temperature, in terms of GPC and thickness uniformity, seems to be near 350°C with ozone as the oxidizer, as determined by Picosun ®[159], or even lower when used with O_2 plasma, as shown in Reference 158. As is the case with bis(ethyl-methyl-amino)silane [153] , BDEAS does not fully react with water. The Si-H bonds in the precursor are not reactive enough, which results in decreased growth rate and, possibly, the presence of impurities in the films.

In the work detailed in this thesis, BDEAS is the ALD precursor of choice for SiO_2 films given its robust performance at accessible experimental parameters, and its relatively widespread use in academic research [135, 154, 156, 158, 160, 161]. The SiO_2 growth from BDEAS was optimized in collaboration with Picosun ®. The reactor temperature was set to its maximum value of 300ºC. The BDEAS pulse length was 0.1 s, followed by a 6.0 s N_2 purge. The precursor bottle was kept at 38ºC. The ozone pulse length was 8.0 s, also followed by a 6.0 s N_2 purge. In our system, SiO_2 grown in this way shows a growth per cycle (GPC) of about 0.7 Å.

3.2. GEO$_2$ ALD GROWTH

GeO_2 is similar to SiO_2 in many aspects, but in ALD it is relatively unexplored, with only a handful reports on its precursors [162–165]. Thin films of GeO_2 have been proposed as a buffer between Ge substrates and high-K dielectric films to reduce the concentration of interface states in MOSFETs [166–168]. In these cases, thermal oxidation, plasma oxidation and vapor growth were used [84, 169], with vapor precursors being alkoxy and halide based. Here we use tetrakis(dimethylamino) germanium (IV) (TDMAGe) instead, which incorporates the lessons learned from SiO_2 ALD. This precursor is mentioned in the patent by ASM [163] but no growth parameters are reported.

In this work, we use a Picosun R-200 Advanced hot-wall ALD system whose chamber opens to a glovebox containing a nitrogen atmosphere, with controlled oxygen and water concentrations. We grow oxide thin films using organometallic Si and Ge precursors. Respectively, these are BDEAS and TDMAGe, both of them purchased from Air Liquide. The precursors are housed in PicohotTM 300 and PicohotTM 200 canisters, which allow heating up to 260ºC and 200ºC, respectively. The organometallic precursors are delivered into the reaction chamber, through heated valve blocks, using nitrogen as carrier gas.

The oxidizer used in this work is ozone, which is produced from an INUSA Ozone Generator using Oxygen 6.0. Our valves allow a minimum opening time of 0.1 s. Accessible process temperatures range from 100ºC to 300ºC, and the typical process pressure is 17 hPa. A temperature of 38ºC for the BDEAS precursor bottle was established to give acceptable delivery rates. The TDMAGe bottle needed to be heated to 80ºC to achieve similar precursor delivery rates to the reaction chamber. The gas lines downstreaming from the bottles were heated to 10-20ºC above the temperature of their respective bottle to avoid precursor condensation taking place before reaching the reaction chamber.

The films reported here are grown on 15x15 mm^2 square pieces of Si(100) wafers purchased from Microchemicals GmbH. Even though the precursors used for GeO_2 and SiO_2 are quite different, both of them use alkylamine ligands. This allowed us to optimize the GeO_2 growth, using as starting parameters those of the SiO_2 growth.

In the case of the combined SiO_2/GeO_2 multilayer growth, there are practical constraints to the process. First, the well-known SiO_2 precursor BDEAS [135, 154, 156, 158, 160, 161], requires ozone or oxygen to function properly in thermal ALD. For this reason, it is highly desirable to simplify the process by using ozone as the oxidizer in GeO_2 growth as well, even though this may lead to combustion-like reactions and less gentle oxidization. The ozone pulse length was fixed at 8 s, sufficient to ensure a complete half-reaction.

Second, the SiO_2 growth is optimal at or above 300ºC. When growing subsequent layers of different materials by ALD, it is in principle possible to change the reaction temperature when switching from one oxide to the next. However cooling and heating the reactor, even for relatively small temperature differences, are slow processes, making the growth time prohibitively long if the temperature needs to be changed repeatedly. For this reason, while the optimal growth temperature for pure GeO_2 may turn out to be different, if GeO_2 growth is still acceptable at 300ºC, this temperature needs to be maintained in the multilayer growth.

Our system minimum operating temperature is, for this process, about 100ºC. This is necessary to avoid condensation of the precursors or their reaction products in the chamber. Its maximum operating temperature is 300ºC in its current configuration. Within this range, the growth rate of pure GeO_2 increases with increasing temperature, remaining approximately invariant above 150ºC (Figure 3.2b). One explanation for this behaviour is that below 150ºC the chemisorption reaction rate for TDMAGe is too low for proper ALD behavior, resulting in a decreased GPC. It could be argued that the stabilization of the GPC up to 300ºC is an indication that precursor decomposition is still not significant at that temperature.

The GPC dependence on pulse length was analyzed as well. The purge times were kept constant for this series. We can see that the GPC at 300ºC increases for longer TDMAGe pulses (Figure 3.2d), while displaying approximately constant values for the short pulse lengths of 0.1 s and 0.2 s. This could indicate that this temperature is, in fact, sufficient to cause noticeable precursor decomposition, but that this has no noticeable effect in the growth provided that the TDMAGe pulses are short enough. This was confirmed by growing a film at 200ºC using TDMAGe pulses of 0.5 s. In that case the GPC was 0.53 Å. This shows that the effect of precursor decomposition on thickness can be minimized either

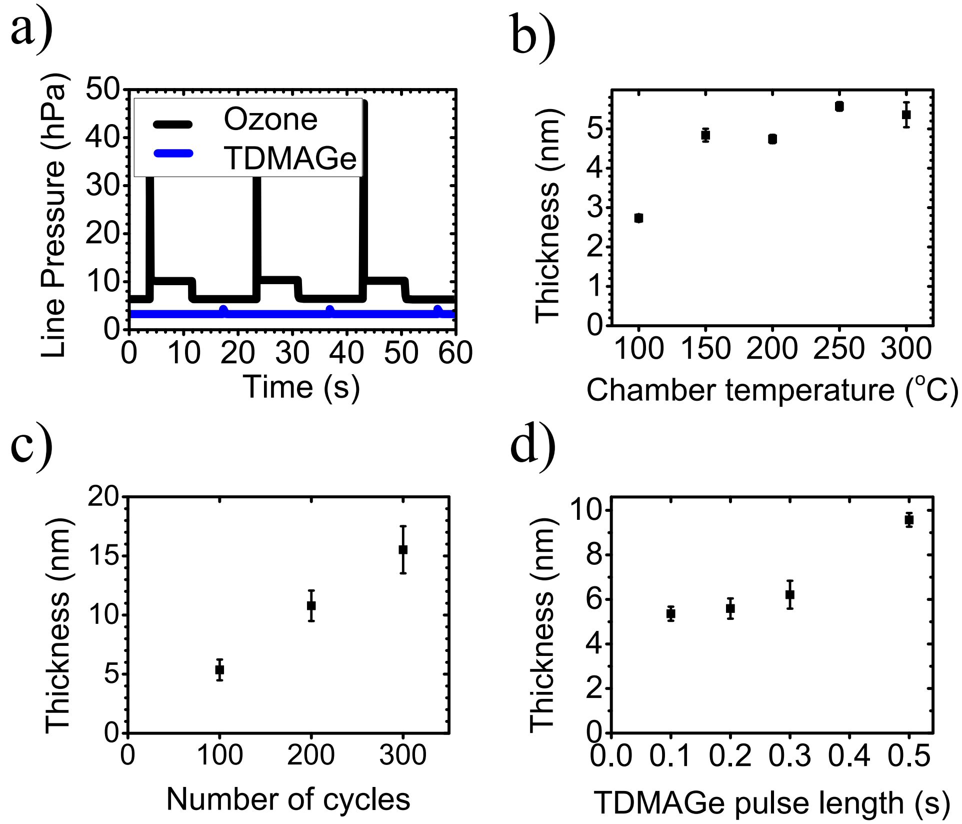

Figure 3.2: a) Sketch of the pulse trains of the two precursors. b) GeO_2 film thickness after 100 cycles at various reactor temperatures. c) GeO_2 film thickness for different cycle numbers, at 300°C. A linear regression for this regime yields a GPC of 0.51 Å. d) GeO_2 film thickness for 100 cycles and at 300°C for different TDMAGe pulse lengths. Error bars are estimated based on sample dispersion.

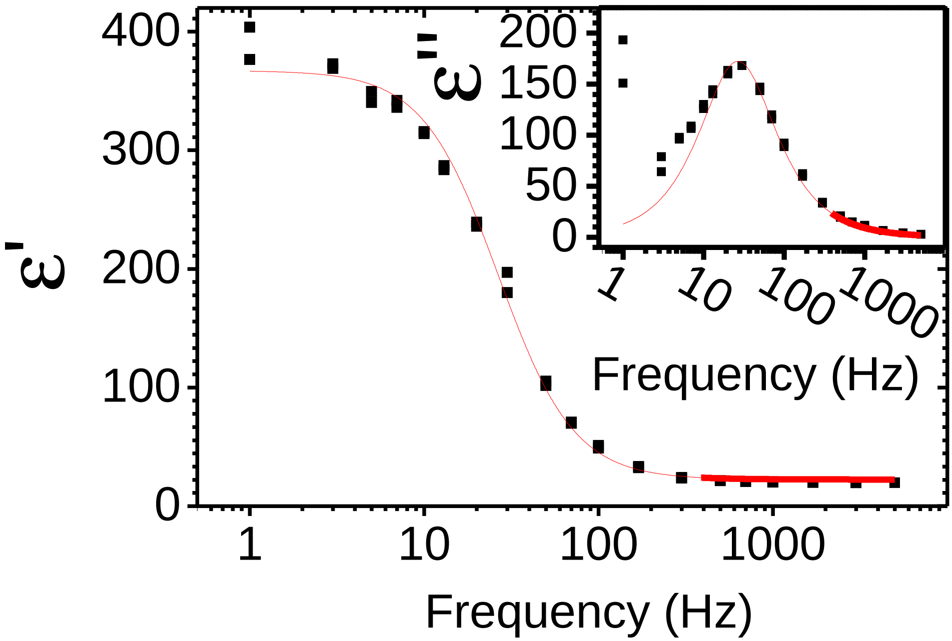

Figure 3.3: Relative permittivity for a 12 nm GeO_2 film as calculated from C-V measurements between 1 Hz and 5 kHz. The imaginary permittivity is plotted in the inset. Dispersion between successive measurements is most visible at low frequencies. The red lines are a Debye fit with $\tau = 6$ ms. A Cole-Cole plot of this dataset yields $\alpha = 0.0346 \pm 0.0001$, which is close to the ideal Debye model ($\alpha = 0$) and suggests a relatively narrow distribution of relaxation times in this frequency range.

by growing at sufficiently low temperatures, which is difficult in our case, as discussed before, or by keeping the pulse length short. Therefore, the shortest pulse length of 0.1 s was chosen. We further show, for large pulse numbers, the dependence of the film thickness with the number of pulses (Figure 3.2c).

3.3. GeO_2 DIELECTRIC MEASUREMENTS

The dielectric properties of GeO_2 films grown with the optimized parameters were also investigated. Figure 3.3 shows the result of several capacitance measurements on one of these films. At low frequencies, we observe a Debye relaxation with a characteristic time of 6 ms, which was determined from fitting the real component of the permittivity (ϵ'_r) [170]. This likely corresponds to space charge relaxation. The relative dielectric constant at 1 kHz is $\epsilon'_r = 22$.

The dielectric constant value that we have determined at 1 kHz is significantly larger than those available in the literature, such as the extrapolated theoretical value of $\epsilon'_r \sim 2.8$ by Walker et al.[171], the experimentally-determined static ϵ'_r between 5 and 7 for GeO_2 grown by Ge oxidization [172, 173], or the near-static value of $\epsilon'_r \sim 8.5$ for vacuum-evaporated films [174]. Some GeO_2 crystalline phases have also been explored [175–177], with their ϵ'_r being significantly different for different phases.

We have also determined the dielectric constant with spectroscopic ellipsometry in the 300-1700 nm range, as can be seen in Figure 3.4. We used thickness values from XRR measurements and then, for GeO$_2$ films of different thicknesses, we fitted the real and imaginary dielectric constant with a single Lorentz oscillator, with a constraint of $\epsilon_{r,inf} = 1$.

The imaginary dielectric constant values were found to be close to zero, as expected for GeO$_2$, and we have not plotted them here. We can compare the real dielectric constants to the values by Fleming[178], Nunley[179], Devyatykh[180], and Pajasová[181]. For all our measured samples the real dielectric constant was found to be consistently lower (between 79% and 85% of Fleming's value at 1600 nm), which is consistent with the relative densities (compared to the bulk values) obtained from the reflectivity fits, see Table 3.1.

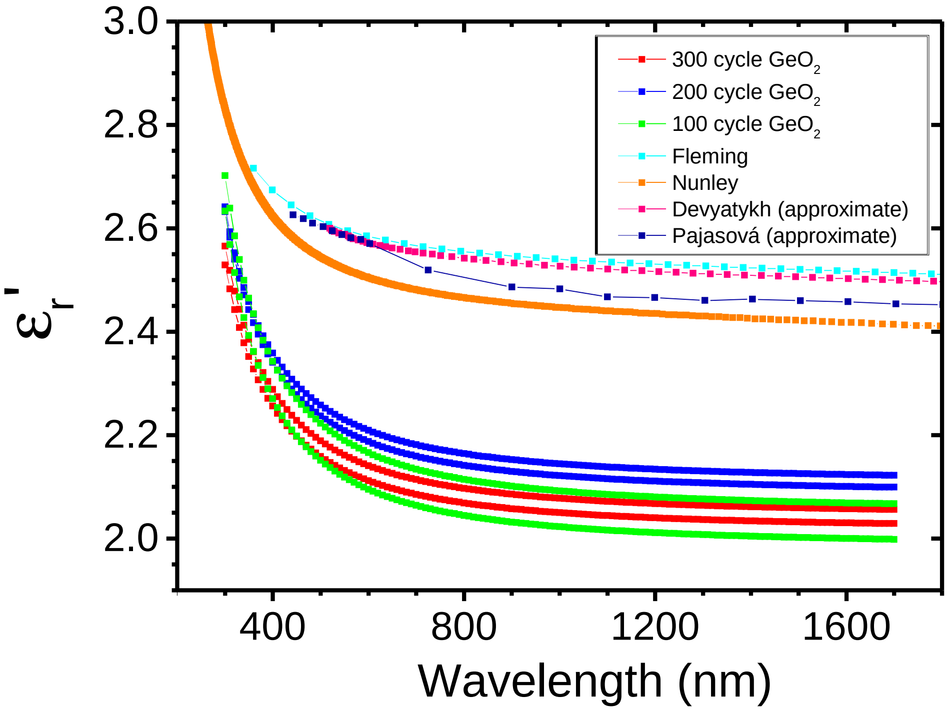

Figure 3.4: Real electric permittivity for six GeO$_2$ samples. Samples with the same growth scheme are plotted in the same color, showing some dispersion. The values found in the literature are also shown for reference.

The electric measurements up to 5 kHz show dielectric permittivities of over 20, whereas the values determined at 1600 nm (187 THz) are near 2. This suggests at least one more relaxation process between 5 kHz and the NIR range. This relaxation can be of the dipole polarization of small amounts of absorbed water, as GeO$_2$ is known to be hygroscopic [182].

3.4. SIO$_2$-GEO$_2$ ALD GROWTH

Thin films consisting of SiO$_2$ and GeO$_2$ multilayers have been investigated in the past, both from solution and vapor deposition methods[183–185], with the focus being mostly on their optical properties. In this work, we show that using tetrakis(dimethylamino) germanium (IV) (TDMAGe) as precursor, it is possible to deposit GeO$_2$, as well as SiO$_2$/GeO$_2$ multilayers by thermal ALD. Proper intermixing between SiO$_2$ and GeO$_2$ in ALD multilayers is a key goal of this growth experiment. Achieving intermixing via post-annealing is not an option, given that these two compounds are known to phase separate, rather than mix, upon heating [186, 187].

The growth of multilayered thin films is, although not the only one, a very common approach to ternary (and more complex) compounds [103]. There are some precedents of SiO$_2$ and GeO$_2$ multilayers in the literature grown from either solution or vapor methods [183–185]. Here we have grown these multilayers by ALD, with two main objectives: first, test the thickness control of our ALD process, and second, achieve a mixed oxide ($Si_{1-x}Ge_xO_2$) through intermixing of the two binary oxides.

For the experiments here, we set the total number of cycles to 300, of which half will be GeO$_2$ and the other half SiO$_2$. Note that, assuming that the behaviour displayed in Figure 3.2c can be extrapolated to lower cycle numbers, the expected thickness for the GeO$_2$ and SiO$_2$ layers would be 8 nm and 11 nm, respectively, taking into account our previously mentioned GPC values at the optimized process parameters. Thus, assuming ALD linear regime, we expect a total thickness of 19 nm approximately, without accounting for the native oxide present on the wafer.This is in good agreement with the values obtained from the fitting of the XRR patterns, which give total thicknesses ranging between 19.2 nm and 20.1 nm (see Table 3.1).

The first experiment, with 150 cycles of TDMAGe/O$_3$ followed by 150 cycles of BDEAS/O$_3$ is denoted as "one repetition" (see Figure 3.5). One repetition, thus, contains a GeO$_2$ sublayer and a SiO$_2$ sublayer. In the following experiments, the number of cycles in each sublayer is subsequently halved, while the number of repetitions is doubled in order to keep the total number of pulses constant. The XRR patterns of these films, their fits and an illustration of the models used in the fits, are plotted in Figure 3.6 (the actual parameters of the model can be found in Table 3.1). By differentiating the experimental data (which has been obtained with a step size of 0.01° in 2θ) at low angles and smoothing it with a Savitzky-Golay filter [188], we determined the critical angle for all the films to be 0.235° ± 0.005°, independent of the number of repetitions (or the periodicity of the multilayer), close to the bulk value for SiO$_2$ (0.234° for a density of 2.65 g/cm^3).

The XRR patterns show clear thickness oscillations in all cases, indicating the good homogeneity of the films and the quality of the top and bottom interfaces. In addition, the patterns corresponding to the films containing from 2 up to 15 repetitions, all display superlattice reflections, attesting for the presence of chemical contrast between the SiO$_2$ and GeO$_2$ sublayers.

The XRR pattern of the film with 15 repetitions shows its superlattice signature peak at about 7.1°, corresponding to a period of 12 Å, which is approximately the size of two unit cells in SiO$_2$ and GeO$_2$ quartz polymorphs. In the case of the 15 repetitions sample, despite the clear superlattice peak, the model is not able to provide a reliable value for the thickness of the individual SiO$_2$ or GeO$_2$ sublayers. This can be understood looking at the

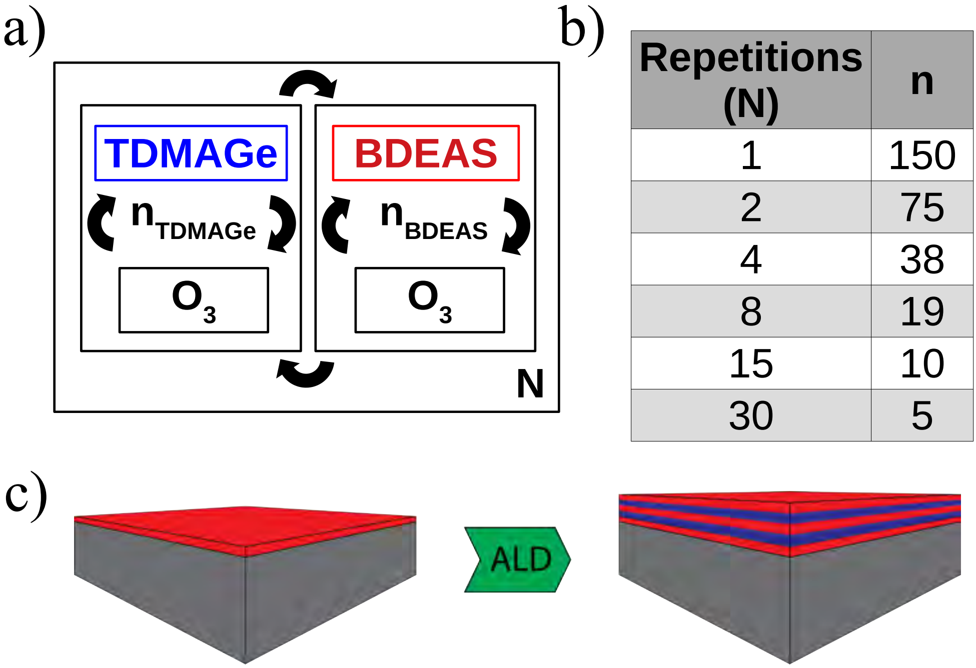

Repetitions (N)	n
1	150
2	75
4	38
8	19
15	10
30	5

Figure 3.5: a) Schematic representation of the synthesis method for the mixed oxide films. In our study, the pulse trains for the two precursors contain the same number of pulses: n_{TDMAGe}= n_{BDEAS}= n, and it varies from film to film. b) Table detailing the number of precursor pulses in each train (n) per sublayer and the total number of cycles (N) in the different films. For the 1:1 pulse ratio used in this work, the total number of cycles (2 n N) was kept to approximately 300 for the whole series. This means that for the 1 repetition case, 150 cycles of TDMAGe/O_3 were done, and after that came 150 cycles of BDEAS/O_3, for a total of 300 cycles in two layers. c) Sketch of the expected layered structure after growth.

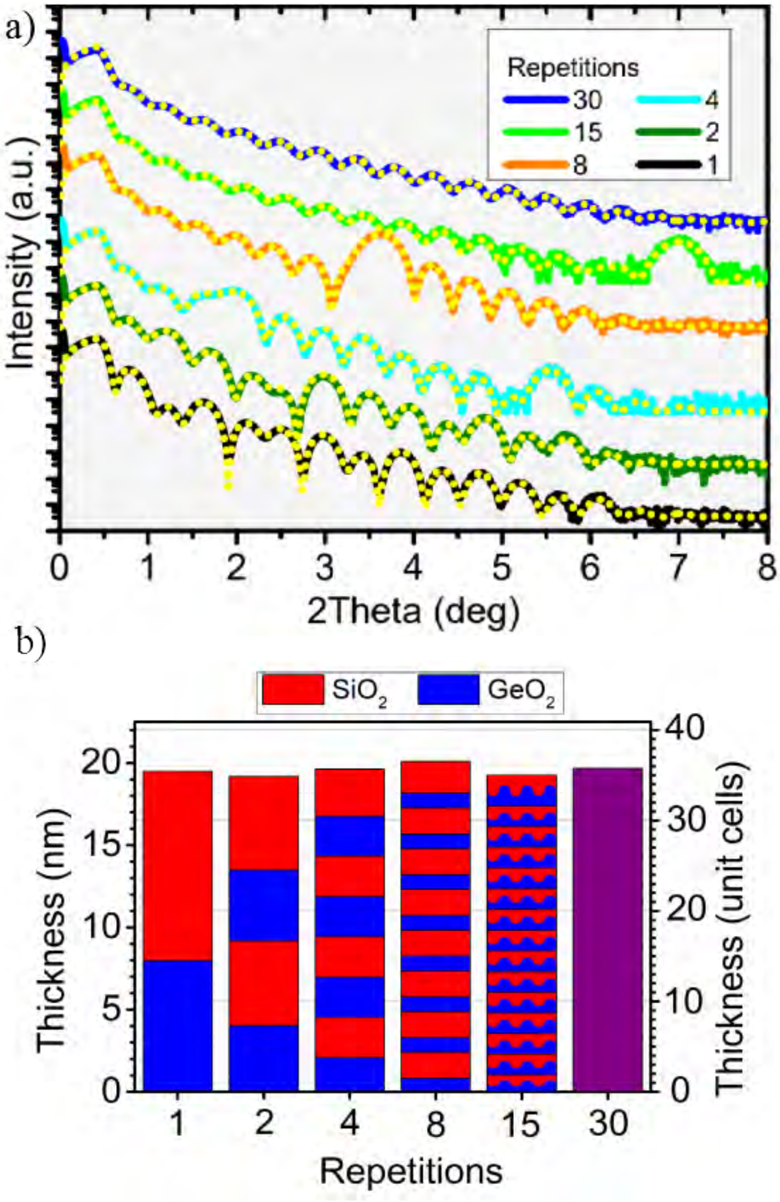

Figure 3.6: a) XRR scans and fits (yellow dashed lines) for the six films, from which the thicknesses were extracted. Superlattice fits (parameters in Table 3.1) add the constraint that all SiO$_2$ layers and all GeO$_2$ layers in a single heterostructure have respectively the same thickness, but this constraint is relaxed for the top SiO$_2$ and the bottom GeO$_2$ layer in each case. b) Sketch of the side view of the grown films, showing the actual layer thicknesses as determined by the XRR fits. The red and blue stripes indicate layers made of different oxides, whereas the purple stripe is used for a layer of mixed oxide. The native SiO$_2$ layers, though both measured by ellipsometry prior to the ALD process and accounted for in the models, are not depicted here. Note that the models do include interface roughnesses. The right axis shows the thickness in multiples of 0.55 nm, which is approximately the average between the SiO$_2$ and GeO$_2$ α-quartz form c-parameter, an it is used as a characteristic length scale of the material (although it is amorphous in this case).

roughness values (see Table 3.1), which are of the order of the estimated sublayer thickness (6 Å). For the 30 repetitions film, only 5 pulses were provided, alternately, for each SiO_2 and GeO_2 sublayer, until completing the total of 300 pulses. Therefore, the superlattice periodicity is expected to be half of the value of the periodicity displayed by the 15 repetitions films, 6 Å. This value is similar to the roughness values obtained with the reflectivity fit and, thus, no chemical contrast is expected. Indeed, in this case, the superlattice model also gives unreliable results but, unlike in the case of the 15 repetition film, the 30 repetition XRR pattern can be modelled by a uniform layer (see Table 3.1), consistent with the absence of superlattice peaks up to an angle of 14°.

It must be pointed out that, as directly visible in Figure 3.6, the SiO_2:GeO_2 thickness ratio, and therefore the atomic ratio, changes from one film to the next, even though the pulse ratio for all of them is maintained as a 1:1. This dependence of the composition on the precise pulsing sequence, and not only on the pulse ratio, has been previously observed [189].

More properly, X-ray Photoelectron Spectroscopy (XPS) was used to perform elemental analysis of the SiO_2/GeO_2 multilayers. An Omicron XM-1000 monochromated Al-Kα source was used with a pass energy to the detector of 20 eV. As shown in Figure 3.7, a full spectrum and individual scans for each element were performed in a SiO_2/GeO_2 multilayer. These scans were recorded with a step size of 0.1 eV and 0.05 eV, respectively. The recorded core-level spectra of the elements were then analysed by decomposition into Gaussian peak components after background subtraction using a Shirley type signal. The sample surface was previously cleaned with an Ar plasma. After 1 minute of etching, the top 1-2 nm of surface material is expected to be removed. The Pt, Au and Ag peaks originate from the holder. It can be seen that no Nitrogen from the precursors is to be found and only a weak C signal can still be found after etching for 1 min.

The topography of the samples was analyzed with a Bruker Dimension Icon Atomic Force Microscope (AFM). The microscope was used in tapping mode, with Tap300Al-G silicon probes from BudgetSensors, which have approximately a 40 N/m force constant and 300 kHz resonant frequency. Subsequent image correction included row alignment and background subtraction, using second-degree polynomials in both cases. The AFM results for the as-grown ALD films are shown in Figure 3.8 here. The RMS roughness values, given in Table 3.1, are in agreement with those used in the XRR data modeling.

3.5. SiO_2-GeO_2 FILM CRYSTALLIZATION

GeO_2 can crystallize in the α-quartz polymorph which, like in the case of the ubiquitous SiO_2-based quartz, is piezoelectric. There are, up until now, few reports of crystalline $Si_xGe_{1-x}O_2$ [58] and only one in thin film form [190]. These nanostructured quartz-structure solid solutions are attractive for a number of applications because they could achieve higher electromechanical coupling than regular SiO_2 quartz [191, 192] as well as higher temperature stability [191].

For this reason, an attempt is warranted to crystallize the amorphous SiO_2/GeO_2 multilayers. Given the relative ease to tune the cycle ratio in ALD, a success here could be followed by a thorough exploration of the concentration range between pure SiO_2 and GeO_2. Nevertheless, the main hurdle remains to crystallize the amorphous oxide films into quartz and avoid other polymorphs [51]. In SiO_2, a common polymorph found by

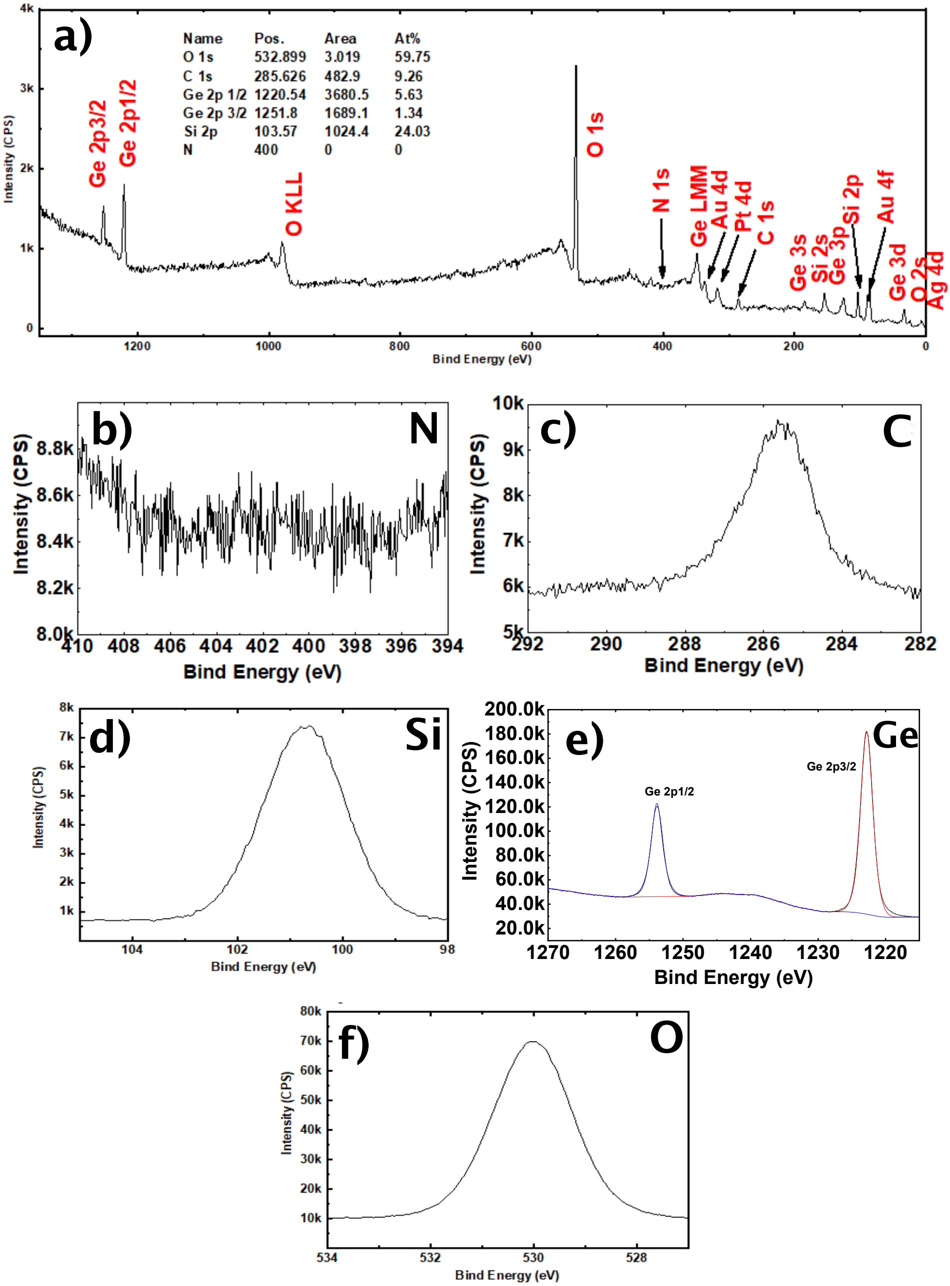

Name	Pos.	Area	At%
O 1s	532.899	3.019	59.75
C 1s	285.626	482.9	9.26
Ge 2p 1/2	1220.54	3680.5	5.63
Ge 2p 3/2	1251.8	1689.1	1.34
Si 2p	103.57	1024.4	24.03
N	400	0	0

Figure 3.7: XPS of an 8-repetition SiO$_2$/GeO$_2$ multilayer sample surface after Ar etching. a) survey spectra with characteristic core levels, including elemental quantification; b)-f) high-resolution spectra of elemental characteristic peaks. Note that the N feature is not visible in b).

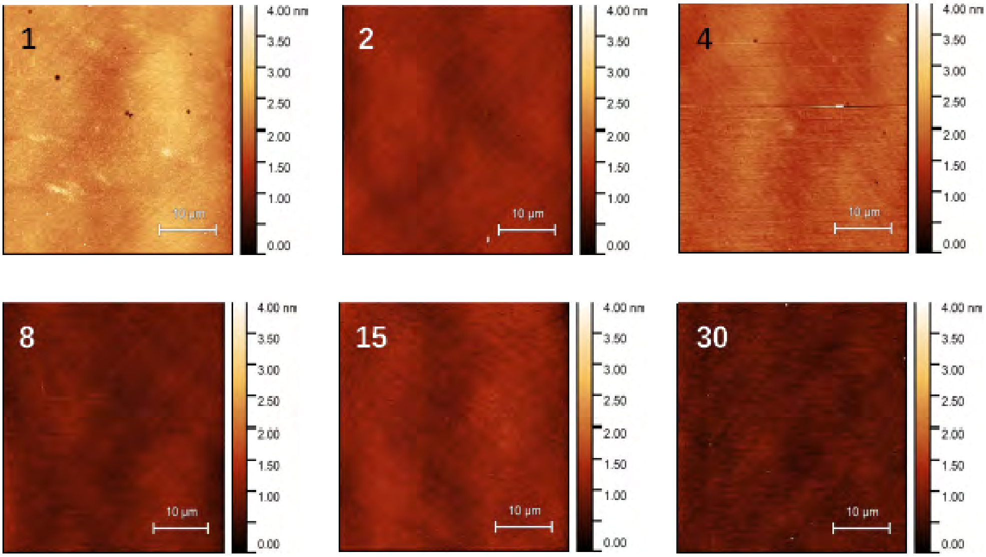

Figure 3.8: AFM topography of the mixed oxide pristine films, with the number of repetitions indicated in the top left image corners. The RMS roughnesses of all films was between 200 pm and 1.5 nm.

simple annealing is α-cristobalite. A proven strategy in order to avoid that is the use of devitrifying agents: metal cation impurities present in the glass which disrupt the silica matrix, leading to the formation of nonbridging oxygen atoms [193]. This lowers the crystallization temperature, potentially avoiding the formation of non-quartz crystallites entirely, as has been demonstrated [76], and more recently exploited in device fabrication [194], in solution-based films.

Our strategy uses existing ALD-grown $Si_xGe_{1-x}O_2$ and the melting agent of choice was strontium. It is possible to intercalate this element with ALD as SrO by adding pulses of the appropriate Sr precursor [189, 195, 196] to the procedure described earlier for SiO_2/GeO_2 multilayer growth. As a preliminary test, we instead used a Pulsed Laser Deposition (PLD) system to grow metallic strontium particles (from a target made out of dendritic Sr metal) on top of the ALD-grown films.

To keep the process simple, we grew these particles at a sample temperature of 100ºC, which is quite low for PLD, and an Ar pressure of 0.01 mbar in the chamber. 90 laser pulses were shot, in order to ensure that the Sr layer remains a set of loosely spaced Sr particles rather than forming large islands or a continuous film. In practice, the moment the samples exited the vacuum chamber, the Sr particles quickly reacted with the air in the room, probably becoming SrO, $Sr(OH)_2$, and eventually settling into $SrCO_3$. This was followed by annealing in a Nabertherm tube furnace ramping at 20ºC/min to 1000ºC and staying there for 5h, powering down afterward. The annealing was done under 200cm^3/min oxygen flow, at atmospheric pressure.

The annealed samples were characterized with Grazing Incidence X-ray Diffraction (GIXRD), and the results are displayed in Figure 3.9. Two control samples were also measured: a pristine silica film with no strontium and an anneald silica film with no strontium.

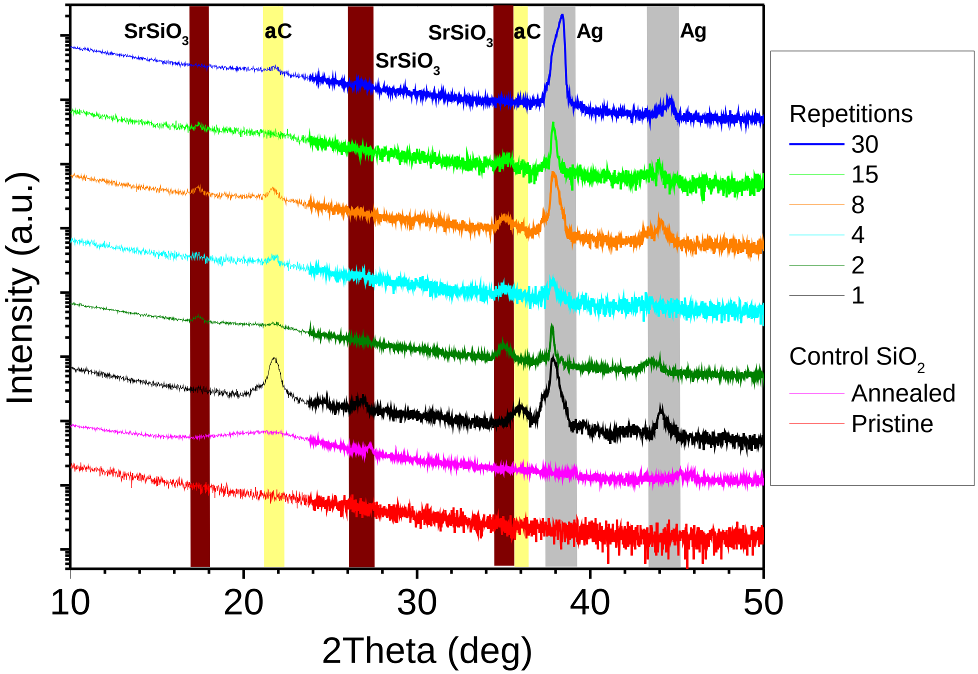

Figure 3.9: GIXRD spectra of six multilayer samples annealed after Sr deposition, and two control SiO_2 samples without Sr. Pristine SiO_2 and SiO_2/GeO_2 multilayers (not shown here), with and without Sr particles, all have very similar GIXRD spectra. The annealed Sr-containing samples display, with varying intensities, diffraction peaks for $SrSiO_3$ and α-cristobalite (marked as αC). There are also two diffraction peaks belonging to silver. This suggests that some of the silver has (200) orientation, as attested by specular scans, and the rest does not. The samples that did not contain added Sr have qualitatively different spectra, which supports the need for devitrifying agent in the crystallization process. The 1-repetition scan cristobalite peaks rise higher above the background than in the other scans, possibly indicating a larger volume of cristobalite formation. However, no clear trend is present as the number of repetitions increases.

In both cases the GIXRD spectra were largely featureless, which suggests that no cristallization took place. On the contrary, Sr-containing samples showed diffraction peaks for α-cristobalite [197] and monoclinic $SrSiO_3$ [198]. We also performed 2θ-ω specular scans which did not return any film signal other than the (200) diffraction peak for silver [199], which we deduce diffused from the backside of the sample during the annealing step.

The GIXRD measurements were followed by SEM observation (Nova NanoSEM, FEI) combined with Energy Dispersive X-ray Spectroscopy (EDS, Octane SDD detector by EDAX) and electron backscatter diffraction (EBSD, using EDAX system equipped with Hikari Plus CCD camera). Team v.4.5 and OIM Analysis 8.1 software were used to perform semi-quantitative elemental and crystal orientation analysis, respectively. Different acceleration voltages for the primary electron beams were used for EDS (5 kV) and EBSD (15 kV) in order to maximize depth and lateral resolution in the former, and provide a reasonable quality of Kikuchi patterns in the latter. EBSD observations were performed in low vacuum mode (0.5 mbar of water vapor) to suppress charging and SEM image drift effects during the lengthy data collection.

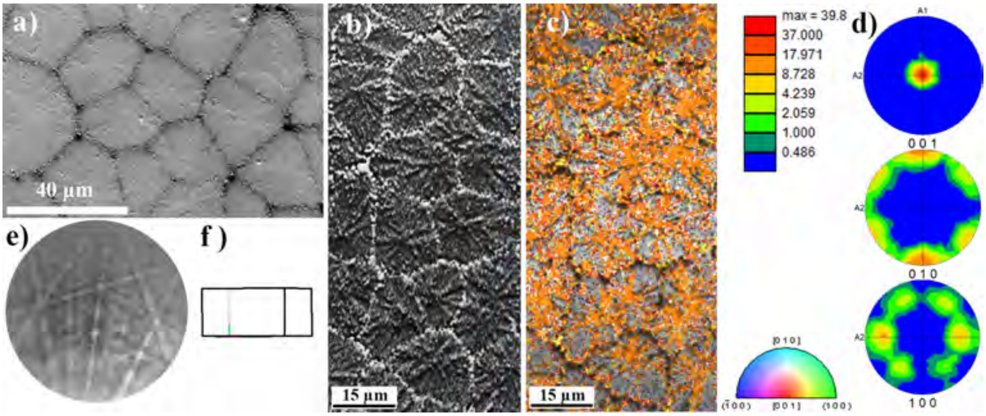

Figure 3.10: Scanning electron microscopy characterization of crystal domains formed after crystallization of a 4-repetition SiO_2/GeO_2 ALD multilayer. a) Secondary electron image; b) Forward scattered electron image of area studied by EBSD; c) [001] IPF+IQ map showing the crystal direction parallel to the sample surface normal; d) (001), (010) and (100) sample texture plots using scale of multiples of random distribution (MRD); e) example of Kikuchi pattern and f) corresponding crystal orientation (axonometric projection in top view).

As the SEM image in Figure 3.10a clearly demonstrates, individual crystal domains create a feature resembling a 2D Voronoi polyhedral tessellation formed by i) nucleation in randomly distributed points followed by ii) stellular 2D growth until impact with crystal growing in neighbor domains. Typical dimensions of these domains vary between 20 and 100 μm and their boundaries are rich in Sr, as EDS measurement confirmed (not shown in Figure 3.10). In Figure 3.10b we are showing a forward scattered electron image map from the area studied by EBSD. This area has size of 46 x 99 μm^2 and contains 41181 mapping points arranged in hexagonal grid with a mutual distance of 0.36 μm. Pixels located close to domain boundaries show a bright contrast due to stronger electron scattering from Sr atoms. The orientation imaging microscopy map in Figure 3.10c is a [001] Inverse pole figure (IPF, color) combined with an Image quality (IQ) map (B&W). Pixels that return low quality EBSD signal, which was not possible to index properly, are not colored, and they represent approximately 34% of all mapping points. Figure 3.10e is an example of a high quality Kikuchi pattern that was possible to index properly using a monoclinic $SrSiO_3$ structure [198]. The IPF map clearly demonstrates a strong preferential direction of the indexed crystal phase presented in the observed domains. This is confirmed by the texture plots shown in Figure 3.10d. We also point out that the indexing is most successful near the center of these domains, with signal quality noticeably decreasing closer to the boundaries. This could indicate that the boundaries have an overlying layer of amorphous material. The (001) crystal plane is parallel to the sample surface in all domains. One of few typical crystal orientations detected in this sample is shown in Figure 3.10f.

The fact that a $SrSiO_3$ phase appears to be predominant in the EBSD IPFs can mean that either the amount of Sr deposited by PLD was too large, or that it was too concentrated near the top of the film. It is not straightforward to control the uniformity of Sr particles grown by PLD, and it is all deposited at the same stage (in this case, entirely on top of the ALD multilayers). For these reasons, a likely improvement over the current technique is the integration of Sr deposition with the $Si_{1-x}Ge_xO_2$ layer, be it by intercalation during ALD growth or by integration of all components into a single PLD target.

3.6. CONCLUSIONS

In this chapter the optimization of GeO_2 layers grown by ALD is demonstrated for conditions similar to those used in SiO_2 growth. This information is subsequently used in the growth of SiO_2/GeO_2 multilayers.

From this series of experiments it becomes clear that electron density, or composition, contrast between the SiO_2 and the GeO_2 sublayers is present down to the atomic level (close to a unit cell of their stable polymorphs). On the one hand, these results attest the excellent capabilities of ALD in general, allowing the growth of heterostructures with atomic-scale thickness control. On the other hand, they nicely illustrate a potential pitfall of the layered approach to compositional tuning in ALD, in that extremely short supercycles are needed in order to achieve a uniform composition rather than a superlattice.

An attempt at ex-situ crystallization results in the strongly oriented growth of $SrSiO_3$. The cristobalite phase is seen to coexist with the strontium silicate, highlighting the difficulties to stabilize the α-quartz phase of SiO_2 on Si substrates. To that end, a procedure is needed that offers more reliable distribution of the melting agent within the film.

3.7. AUTHOR CONTRIBUTIONS

This work is a collaboration between the University of Groningen (UG) and the University of Twente (UT) under the NWO TOP-PUNT programme "Searching for the Si of piezoelectrics". J. Antoja-Lleonart (UG) and B. Noheda (UG) coordinated the work. J. Antoja-Lleonart carried out the sample synthesis, characterization and modelling, wrote the manuscript and took part in discussions. K. de Hond (UT) performed the multilayer X-ray reflectometry scans (Figure 3.6a) with a rotating anode diffractometer, and took part in the discussion of the results. S. Huang (UT) measured and analyzed the X-ray photoelectron spectra and did the Ar plasma etching. S. Zhou (UG), G. Koster (UT), G. Rijnders (UT), and B. Noheda all took part in discussions and text revisions.

The EBSD data was measured and analyzed by Václav Ocelík of the Nanostructures of Functional Oxides group at the University of Groningen.

Table 3.1: Summary of the parameters resulting from the fitting of the XRR data of the different films. The AFM-obtained RMS roughnesses are tabulated, filtering out large particles, averaged over several locations in each case and rounded down to the nearest Ångstrom. Each model is made up of at least one bottom GeO_2 and one top SiO_2 sublayer. Models for films with more than one repetition also contain alternating SiO_2 and GeO_2 sublayers in the middle of the film. These middle layers are repeated N-1 times in the model and their parameters are optimized separately from those of the top and bottom sublayers. Due to the model-based determination of all of these parameters, and the relative complexity of the models, the uncertainty for most of them is difficult to estimate. Sublayer thicknesses have been rounded to a tenth of an Ångstrom and roughness values have been rounded to the nearest Ångstrom. Densities are reported with three significant figures. The sublayer densities are also indicated as a percentage of the bulk SiO_2 and GeO_2 densities. For each fit we also indicate the Figure of Merit (log), which is calculated by integrating the difference between the logarithms of the experimental and simulated XRR intensities. We also include in each case the total thickness and average density calculated from the results of the models. The spectra for 15 and 30 repetitions were difficult to model, and the true layer thicknesses could not be uniquely determined. The parameters for those models are added in blue font to indicate that more than one solution produced similar figures of merit, and as such those values are not as reliable as those of the previous four models. The single layer fit for the 30 repetitions pattern uses a stoichiometry of $Si_{0.58}Ge_{0.42}O_2$, averaged from the first four fits.

Model parameters							
Repetitions	**1**	**2**	**4**	**8**	**15**	**30**	**30 (single layer fit)**
AFM roughness (Å)	7	3	1	2	2	3	3
Top SiO_2							
Thickness (Å)	115.4	57.0	28.6	19.3	6.5	0.2	
Density (g/cm^3)	2.22 (83%)	2.25 (84%)	2.14 (80%)	2.17 (81%)	2.15 (80%)	2.01 (75%)	
Roughness (Å)	6	6	6	5	5	5	
Middle GeO_2							
Thickness (Å)		43.0	24.4	9.0	12.1	1.9	
Density (g/cm^3)		3.76 (89%)	3.57 (84%)	4.23 (100%)	3.17 (75%)	3.60 (85%)	
Roughness (Å)		6	6	6	4	10	
Middle SiO_2							
Thickness (Å)		51.6	24.6	15.8	0.5	5.0	
Density (g/cm^3)		2.20 (82%)	2.21 (83%)	2.04 (76%)	2.11 (79%)	2.47 (92%)	
Roughness (Å)		6	6	8	9	6	
Bottom GeO_2							$Si_{0.58}Ge_{0.42}O_2$
Thickness (Å)	79.7	40.3	20.8	8.3	9.8	1.0	199.9
Density (g/cm^3)	3.75 (89%)	3.76 (89%)	3.59 (85%)	4.08 (97%)	3.17 (75%)	3.80 (90%)	3.92
Roughness (Å)	6	6	6	6	5	9	5
FOM (log)	0.0798	0.0725	0.108	0.0591	0.114	0.0425	0.0701
Total thickness (nm)	19.5	19.2	19.6	20.1	19.3	20.1	20.0
Average density (g/cm^3)	2.85	2.89	2.85	2.82	3.10	2.78	3.92

4

PLD GROWTH AND CRYSTALLIZATION OF $Si_{0.7}Ge_{0.3}O_2$

The growth of α-quartz based piezoelectric thin films opens the door to higher-frequency electromechanical devices than those available through top-down approaches. We report on the growth of SiO_2/GeO_2 thin films by Pulsed Laser Deposition and their subsequent crystallization. By introducing a devitrifying agent uniformly within the film, we are able to obtain the α-quartz phase in the form of platelets with areas above 100 μm at accessible temperatures. Films containing different amounts of devitrifying agent are investigated, and their crystallinity is ascertained with X-ray diffraction and Electron Back-Scatter Diffraction. Our work highlights the difficulty in crystallization when competing phases arise that have markedly different crystalline orientation.

4.1. INTRODUCTION

α-quartz is a well-known piezoelectric phase of SiO_2, thus composed of abundant, inexpensive and nontoxic elements. It finds use in several electromechanical devices, including resonators [60] in oscillator circuits and Quartz Crystal Microbalances[59]. The highest frequencies that can be attained when using a quartz resonator as a frequency standard are limited by current industrial top-down methods of quartz production [13]. These often start with the hydrothermal synthesis of macroscopic quartz crystals, which has not evolved much in the recent decades [17, 48, 57]. After this, the crystals are machined, polished and etched down to the desired resonator size. Until recently, this process has had a lower size bound of the order of a few micrometers, which in turn limited the natural resonator frequency below 1 GHz. In the last two decades, this has been pushed to the sub-micron range, achieving resonance frequencies in the GHz regime [18, 200].

This chapter includes content published as:
Jordi Antoja-Lleonart, Václav Ocelík, Silang Zhou, Kit de Hond, Gertjan Koster, Guus Rijnders, Beatriz Noheda. Growth and crystallization of SiO_2/GeO_2 thin films on Si(100) substrates, *Nanomaterials*, **2021**, *11(7)*, 1654.

It is interesting to grow quartz as a thin film, bypassing all the downscaling and transfer steps and allowing lower resonator thicknesses. This has already been explored with chemical vapor techniques [64–67] and chemical solution methods [74, 76–78, 201]. Most recently, it was shown by Zhou et al. that GeO_2 films can be grown with the the α-quartz structure homoepitaxially on single-crystal Al_2O_3 substrates by Pulsed Laser Deposition [190].

Here we aim to grow quartz thin films on Si(100) substrates. The films are deposited first in the amorphous state and are crystallized following a post-annealing process. This route is chosen because crystallizing amorphous silica films from the melt is not possible. The phase diagram of SiO_2 imposes significant constraints: firstly, because silicon substrates melt at a lower temperature than SiO_2 and, secondly, because other SiO_2 phases are expected to become kinetically trapped [51, 54]. A way around this constraint is to consider α-quartz isostructural materials with a lower melting point, such as GeO_2, by itself or in solid solution with SiO_2, an approach we have followed in this work. The relative disadvantage of the lower abundance of GeO_2 compared to SiO_2 is somewhat compensated by its larger piezoelectric response [202]. In addition, a common way of lowering the process temperature is weakening the strong silica network through the introduction of certain metal impurities. These are alternately referred to as devitrifying agents, melting agents, or network modifiers [193, 203]. This has been successfully applied to various thin films [74–78, 204], including amorphized layers on quartz [69, 70, 73] and GeO_2 structures [56]. In this work, we introduce a Sr salt to the films to act as the melting agent.

4.2. EXPERIMENTAL

For this study, we used Si(100) substrates, which were cut down to 15x15 mm^2 squares from 4" Czochralski-grown, boron p-doped ($\rho \sim$ 1-10 Ωcm) wafers manufactured by Microchemicals GmbH. The cut substrates were washed with ethanol absolute, acetone, and isopropyl alcohol as described in our previous work [205].

Thin films were grown using Pulsed-Laser Deposition (PLD) with home-made own ceramic targets. The process started by mixing SiO_2 α-quartz (99.995%, -40 mesh), GeO_2 (99.9999%), and $SrCO_3$ (99.99%) powders, all purchased from Alfa Aesar. We used an agate mortar and balls in a Fritsch Pulverisette ball mill, rotating at 150 rpm for 30 minutes. The powders (2 g in total) were then recovered and pressed into a disk of 20 mm diameter and about 3 mm thickness under 10 tons in a hydraulic uniaxial press. The pellets were annealed in air at 900ºC for 1 hour. We used a UHV-capable vacuum chamber to house the PLD process. The samples were heated resistively and placed 5 cm away from the targets, which were ablated with a 248 nm KrF exciplex laser. For the ablation of these targets we used a spot size of 1.36 mm^2 and a fluence of 2.5 J/cm^2. The sample temperature during growth was kept to 100ºC and the process pressure was 0.1 mbar O_2.

After PLD growth, the samples were cut to 5x5 mm^2 squares prior to annealing. The annealing step was carried out in an alumina crucible inside a Nabertherm tube furnace, ramping at 20ºC/min to 1000ºC and maintaining it for 5 h, powering down afterward [1].

---

[1] There were slight variations in the furnace temperature over time. For the 0%, 0.625%, 1.25%, 2%, and 3% samples (mole percent) a temperature setpoint of 1050ºC was used as the equivalent of the original annealing conditions.

The annealing was done under 200 cm^3/min oxygen flow, at atmospheric pressure.

Coplanar grazing incidence X-ray diffraction (GIXRD) was used to characterize the crystalline films. For this work, we used a Panalytical X-pert Pro MRD thin film X-ray diffractometer, with a 1/16º divergence slit and a 4-bounce Ge(220) monochromator for the incident beam. We kept the incident angle of the primary beam on the sample to 0.55º, and we scanned only the 2θ angle. A PIXcel3D area detector was used in Scanning Line (1D) mode to improve counting statistics. Symmetric $2\theta/\omega$ scans were recorded in the same setup as the GIXRD scans, only adding a 1/16 slitº and changing the area detector to 0D (receiving slit) mode. For X-ray reflectometry (XRR) measurements, we use a 1/16º divergence slit and a Ge(220) hybrid monochromator for the incident beam, and the detector is a proportional counter fitted with a 1/8º slit.

The topography of the samples, before and after film growth and crystallization, was analyzed with a Bruker Dimension Icon Atomic Force Microscope (AFM). The microscope was used in tapping mode, with Tap300Al-G silicon probes from BudgetSensors, which have approximately a 40 N/m force constant and 300 kHz resonant frequency. Subsequent image correction included row alignment and background subtraction, using second-degree polynomials in both cases.

The optical microscopy images were captured with an Olympus Vanox-T microscope. Images were auto white balanced during acquisition, to correct for the lamp color temperature.

After crystallization, the surfaces were observed using scanning electron microscopy (SEM, Nova NanoSEM, FEI) combined with Energy Dispersive X-ray Spectroscopy (EDS, Octane SDD detector by EDAX) and electron backscatter diffraction (EBSD, using EDAX system equipped with Hikari Plus CCD camera). Team v.4.5, OIM Analysis 8.1, and MTEX[206] software were used to perform semi-quantitative elemental and crystal orientation analysis, respectively. Different acceleration voltages for the primary electron beams were used for EDS (5 kV) and EBSD (15 and 20 kV) in order to maximize depth and lateral resolution in the former, and provide a reasonable quality of Kikuchi patterns in the latter. EBSD observations were performed in low vacuum mode (0.5 mbar of water vapor) to suppress charging and SEM image drift effects during the lengthy data collection. The texture analysis parameters were as follows: Harmonic texture, using a Harmonic series expansion (series rank 34), a Gaussian smoothing of 5.0 degrees, and triclinic sample symmetry.

XPS measurements were carried out in a UHV system with a background pressure below 10^{-10} mbar. The source was an Omicron XM-1000 monochromated Al Kα source. A pass energy to the detector of 50 eV was used. All scans were recorded with a step size of 0.1 eV and a time per step of 1 s. The elemental compositions were extracted by applying a Shirley background subtraction to the peaks and utilizing a Gaussian fit.

4.3. RESULTS AND DISCUSSION

4.3.1. SIO_2/GEO_2 FILM GROWTH

Five different targets, with a Si:Ge atomic ratio of 7:3 and varying amounts of $SrCO_3$ (x), were used, with x = 0, 0.625, 1.25, 2, 2.5, 3, 5, 10 and 20 mole %. The 0% samples were grown as a control experiment. This concentration range is similar to that used by Zhang et al. in their recent CSD report [78].

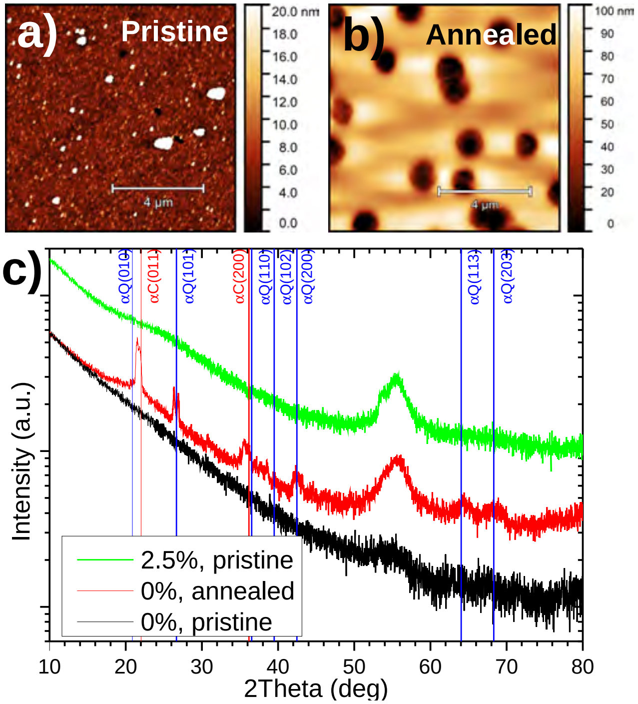

Figure 4.1: a) AFM images of a sample without Sr before annealing (R_{RMS} = 21 nm). b) AFM after annealing (R_{RMS} = 21 nm). c) GIXRD scans of both the as-deposited and annealed x = 0% samples, together with a pristine x = 2.5% sample for comparison.

The mixed SiO_2/GeO_2 films were all grown with the same parameters, described in Section 4.2. Because of the low growth temperature, the pristine films grew in the amorphous state. Supporting evidence of this can be seen in Figure 4.1, which includes images and GIXRD patterns of thin films that did not contain any $SrCO_3$ (see Reference 78 for a similar control). Although large particles remain visible in spots, the RMS roughness appears not to change through annealing. In some regions, AFM clearly shows the appearance of holes in the sample, which we attribute to bubbles formed due to Ge or O loss (see Reference 186). In the GIXRD scans of annealed Sr-less samples, there are small peaks below 30º which we have attributed to α-cristobalite and α-quartz. Figure 4.1 also shows the GIXRD spectrum for an as-grown x = 2.5% sample, confirming the absence of film diffraction peaks before the anneal step *including* in samples that do contain $SrCO_3$.

The pristine films were characterized with AFM and XRR. Through AFM results, shown in Figure 4.2, we determined that these films were relatively rough (RMS roughnesses of 3-15 nm), containing visible particles with sizes in the few hundreds of nanometers, which probably originate from the target. We attribute this to the low thermal conductivity of SiO_2 and GeO_2 and/or poor target density, which all contribute to local heating and particle ejection [207].

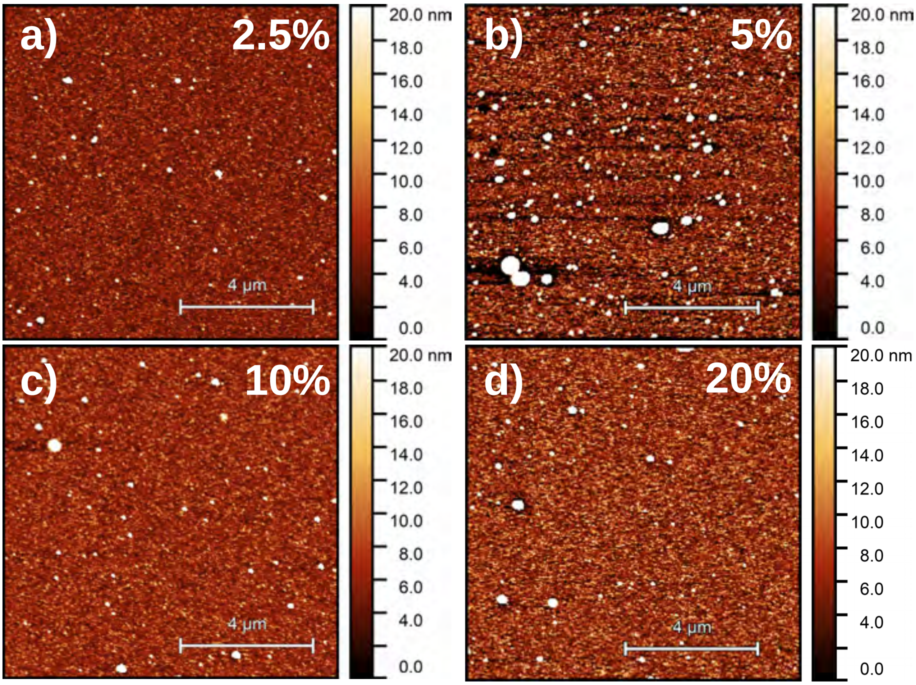

Figure 4.2: AFM pictures of the pristine films. The RMS roughnesses are 3 nm (a), 15 nm (b) 4 nm (c), 7 nm (d).

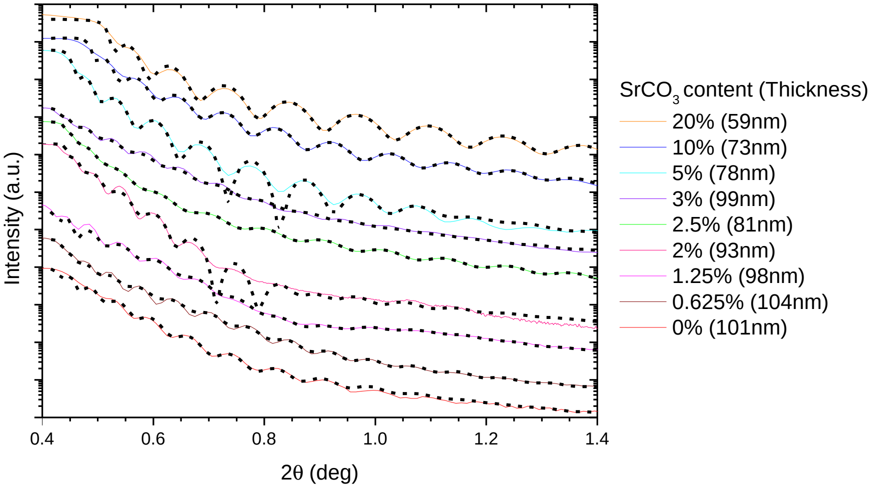

Figure 4.3: XRR scans (solid lines) and fits (dotted lines) for samples with x = 0-20% grown with 1800 laser pulses. The legend shows the $SrCO_3$ content as well as the thickness rendered by the fit.

We performed X-ray reflectometry (XRR) measurements of the pristine PLD-grown samples for an indirect estimation of the film thicknesses. The results are shown in Figure 4.3, where it is evident that the XRR spectra displayed only weak oscillations, possibly also as a consequence of the sample roughnesses. We have overcome this problem by measuring thinner films, and then extrapolating the growth to the films we used for annealing. The XRR scans shown here correspond to films grown with 1800 laser pulses. The films used for annealing in the main text were grown with twice as many laser pulses, 3600, and thus we expect that they will be approximately twice as thick. Therefore, our thickness estimate ranges between 120 nm and 210 nm (prior to annealing) for the $SrCO_3$-containing films described in the rest of this chapter.

We used the GenX software to fit the experimental data [132]. In Figure 4.3 we show the XRR fits superimposed on the scans, and the SiO_2/GeO_2 layer thicknesses are shown for each sample. For the aforementioned reasons, the results are approximate, and we use them only as an estimate for the film thicknesses. We have also extracted the critical angle values for each of those scans by differentiating the intensity and fitting the area near the critical angle with a Gaussian function. For each case, the calculated value (from the theoretical density and composition of the target) is compared to the center of that Gaussian in Figure 4.4. The error in the critical angle data is comparable to the differences between the samples, which makes it difficult to draw strong conclusions. However, it can safely be said that the experimental critical angle values are generally lower than expected from our calculations.

The calculated mass density and the calculated scattering length density (SLD) of the films both increase with $SrCO_3$ content following approximately linear trends. Translating the measured critical angle data to SLD (SLD $\propto \theta_c^2$), we can say that, past x = 5%, the experimental SLD also increases with $SrCO_3$ concentration, although the increase seems to be more dramatic in the experimental data than in our previous calculation. In glassy GeO_2

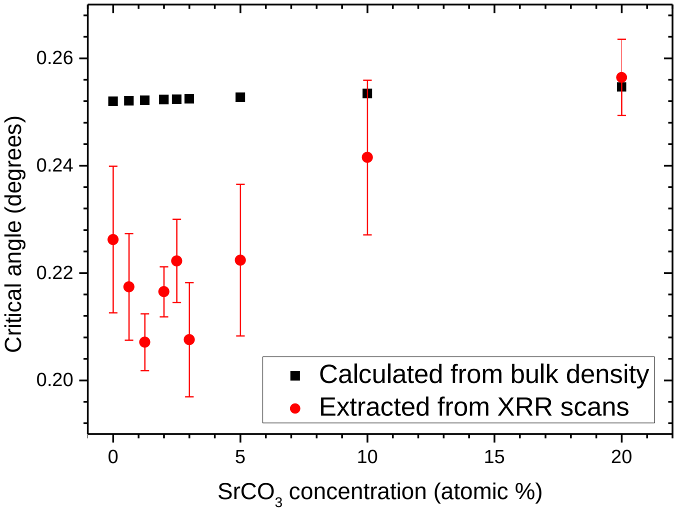

Figure 4.4: Plot of the critical angle for total external reflection of the sample series. The values calculated from the bulk densities (assuming stoichiometric transfer and additive volumes of $Si_{0.7}Ge_{0.3}O_2$ and $SrCO_3$) are shown in black and the experimentally-determined values are in red. The error bars are based on the width of the Gaussians used to obtain the experimental values, which is larger than the scan step size for all measurements.

containing alkali ions, it has been observed that density has an anomalous dependence on increasing alkali concentration, showing a maximum around x = 15-20% [208]. This increase occurs due to a progressive change of the Ge atom coordination. Although this anomaly may not apply equally to Sr ions, a similar behavior could explain the disparity between the experimental results and our predicted data, which is a weighted average of the bulk densities for SiO_2, GeO_2 and $SrCO_3$, therefore not capturing the details of possible structural changes in the silica-germania matrix.

4.3.2. FILM CRYSTALLIZATION

After annealing the PLD-grown films at 1000ºC, they showed changes in topography. From AFM measurements, we can observe the formation of micrometer-scale crystalline features in all $SrCO_3$-containing films, as shown in Figure 4.5. The lateral size of some of these crystallites often exceeds the capabilities of our AFM (> 40 μm). We note that the crystallization patterns change depending on the films $SrCO_3$ content. The differences in crystallization behavior become much clearer with optical microscopy, as seen in Figure 4.6. In films with x = 2.5% and 5%, dendritic crystallization appears to have taken place, while for x = 10% and 20% a less orderly pattern arises.

The elemental composition of the films was measured by X-ray photoelectron spectroscopy (XPS). We did this for x = 2.5 and 20% films, both before and after annealing. One could expect imperfect stoichiometry in the transfer of SiO_2/GeO_2, due to preferential ablation and differences in sticking coefficient [207], which would lead to Ge-poor films. Additionally, a loss of Sr might take place from the film bulk to the surface across the annealing process [76].

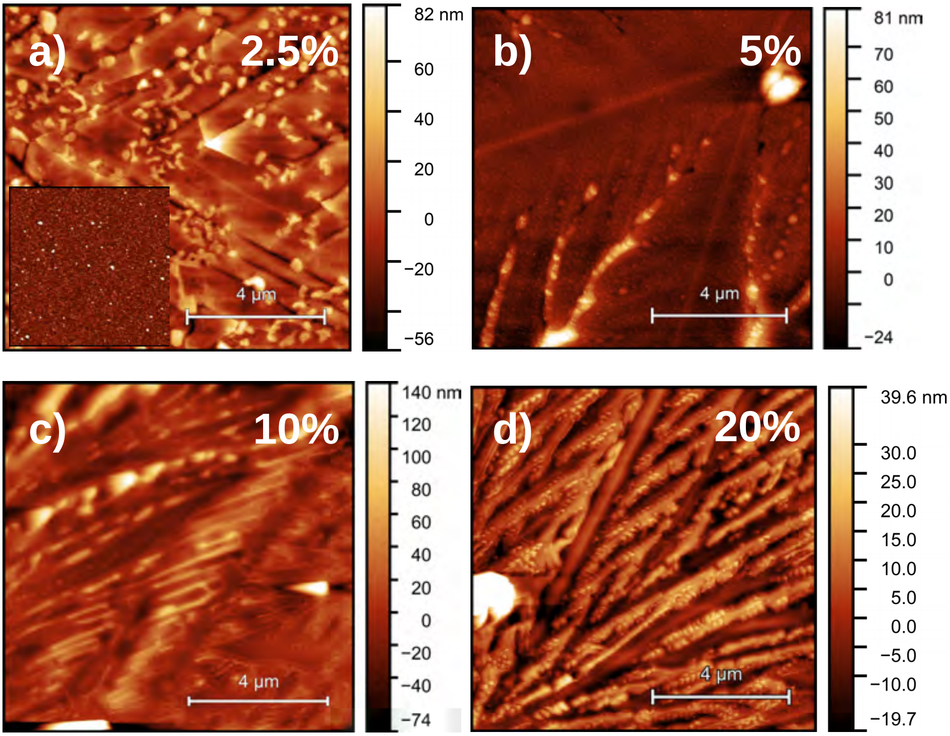

Figure 4.5: AFM pictures of the films after annealing. The RMS roughnesses are 18 nm (a), 8 nm (b), 12 nm (c), and 31 nm (d). Note that, while the image size is identical for all of them, the Z scale is not. Inset: image of the pristine 2.5% sample (RMS roughness = 3nm).

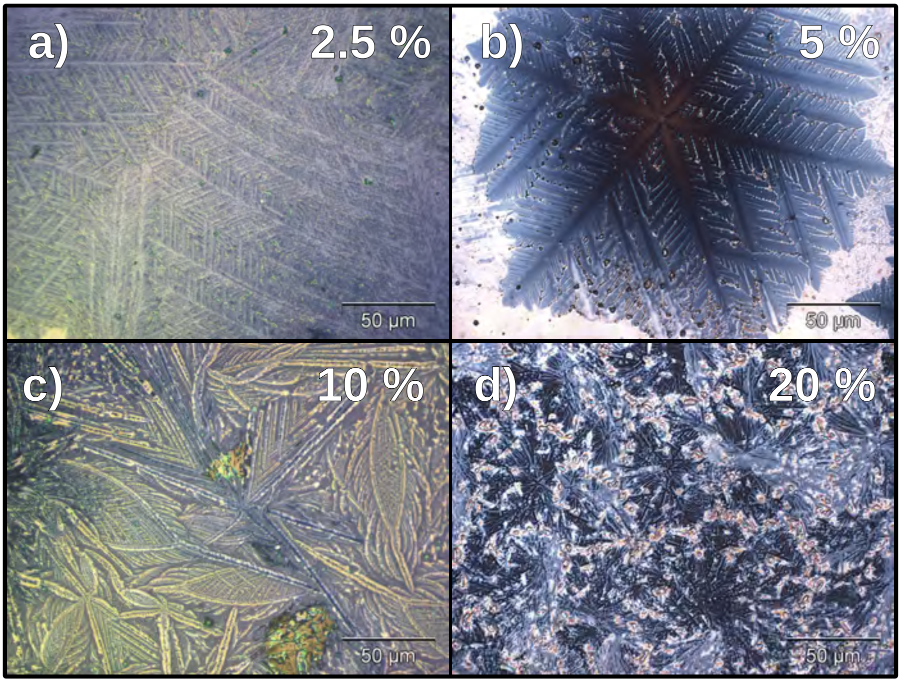

Figure 4.6: Optical microscopy pictures of $SrCO_3$-containing $Si_{0.7}Ge_{0.3}O_2$ samples after annealing. a) and b) show the growth is dendritic at low Sr content. c) shows the formation of long needles, and d) displays small, disorderly crystalline features. Images of the remainder of the concentration series are available in Figures S6 and 4.1.

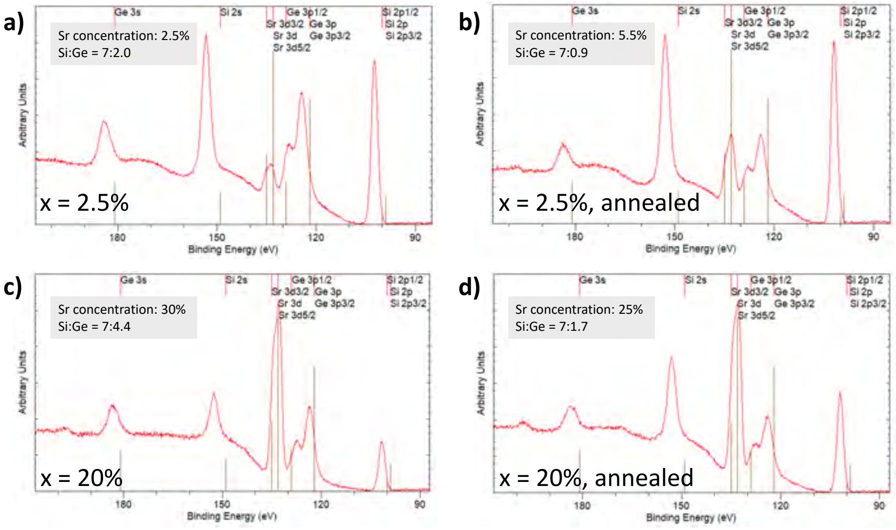

Figure 4.7: a,b) XPS spectra of x = 2.5% samples before and after annealing. c,d) XPS spectra of x = 20% samples before and after annealing. The grey insets show the concentrations of Sr and the ratio of Si to Ge that were extracted from the spectra. We estimate the error in the individual elemental amounts to be ±0.5%.

As the results in Figure 4.7 indicate, the Si:Ge ratio is indeed higher than the one used in target synthesis (which is 7:3) in all but the first panel, which corresponds to the as-grown x = 20% sample. The rest are consistent with the preferential Si transfer. After annealing, the ratio is further increased, which we attribute to the higher volatility of Ge compared to Si in the oxide matrix. The as-grown Sr atomic content is consistently larger than expected for the x = 20% sample, and it decreases after annealing. In contrast, the Sr atomic % is correct within error for the as-grown x = 2.5% sample, but it nearly doubles after annealing.

We know from the work by Carretero et al. that annealing Sr-doped SiO_2 films causes the Sr to be expelled to the film surface as crystallization takes place [76]. Hence, a decrease in the film Sr content was expected. However, the increase of Sr content for the x = 2.5% sample seems, in a first approach, to contradict such behavior. We therefore performed angle-dependent XPS in order to gain more information about the elemental composition of the x = 2.5% films as a function of depth. We show in Figure 4.8a that, after annealing, the Sr content increases across all measured angles, becoming highest at larger angles, which indicates an accumulation closer to the sample surface, in agreement with Carretero et al. [76]. Figure 4.8b further shows that, while annealing lowers the Ge content as well, its angle dependence is much weaker, and in fact the data at different angles show the same composition within error. We are limited here by the probing depth of XPS (which is about 5 nm at normal incidence and decays with the cosine of the incident angle), though it stands to reason that the film is Sr-depleted further from the surface. In the case of the annealed x = 20% film, annealing seems to reduce the Sr concentration at normal incidence, rather than increasing it.

Figure 4.9 shows the specular $2\theta/\omega$ XRD measurements done on six annealed samples

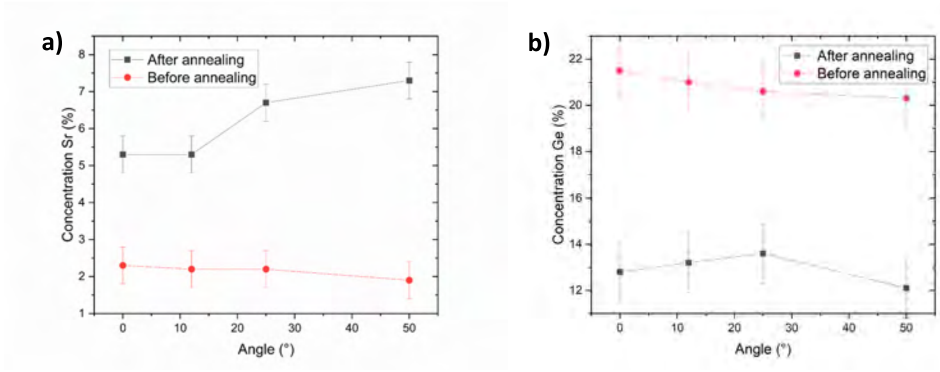

Figure 4.8: Angle-dependent XPS-determined elemental concentrations of the x = 2.5% samples before and after annealing. The Sr and Ge concentration are shown in (a) and (b) respectively. The angle is defined with respect to the surface normal of the samples.

of different Sr content. The only clear feature of these scans is a Si diffraction peak near 33°, which is often visible in specular measurements on Si(100) substrates, regardless of the presence and nature of thin films grown on them. This peak occasionally gets mislabeled as Si(002), which itself is a forbidden reflection with F *exactly* equal to zero [209]. Instead, the peak we observe originates from multiple scattering in the Si lattice, and its intensity varies strongly with misalignment in ϕ (which is further evidence that it does not belong to a plane parallel to the sample surface), thus it is not identical in all five scans. With the exception of the 2% sample (where some peaks appear that we have attributed to $SrGe_4O_9$), no film signal appears in the scans, which suggests that either the crystalline phases either are very minoritary, or they are not suitably oriented for specular measurements. Even if neither of those is the case, oriented crystalline areas with sizes smaller than the coherent length of the X-rays could still be present.

GIXRD measurements are shown in Figure 4.11. All scans show a characteristic broad feature near 55°. This peak is also present in films with no $SrCO_3$, and it can also appear when measuring non-annealed films and pristine Si(100) substrates. Although scantily reported, this feature has been observed by other authors, who conjecture that the peak is from the Si(113) family [210]. GIXRD of a pristine Si(100) substrate also reveals this same signal, which means that it does not originate in the PLD-grown film and that it is not a result of annealing. As shown in Figure 4.10, we have simulated a pole figure of the Si(113) plane family (whose Bragg peaks we expect at 2θ = 56.13°) for the case of a Si(100) substrate, with its [011] axis at 0°. There are, among others, four poles at χ near 25.24° and ϕ = (0+90n)°. During the XRD measurements shown here, the substrate edges (along their [011] direction) are approximately parallel to the beam, which means that two of these poles are at, or very close to the scattering plane during the XRD scans shown in Figures 4.11 and 4.1. During a GIXRD scan, these planes come near the diffraction condition. Weiss reports an additional, much sharper peak near 51°, which is precisely where it should be expected if we account for the incident angle being nonzero[210] and including the χ angle reported in Figure 4.10. However, 51° lies several degrees off of the expected 2θ value from the Si(113) plane spacing. Conversely, the signal at 56° has the

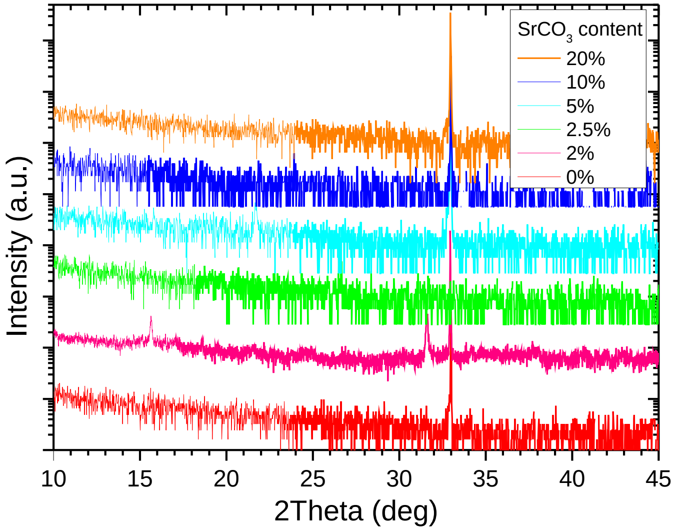

Figure 4.9: Symmetric $2\theta/\omega$ scans for the film series. The multiple diffraction signature is visible near 33°. In the 2% scan, weak reflections from $SrGe_4O_9$ are visible above the noise.

correct position in 2θ but the wrong orientation in χ, and it is tentatively explained by Weiss as a consequence of beam divergence.

We have aditionally performed GIXRD while rotating a sample along the ϕ direction, shown in Figure 4.10, which reveals that this signal appears, sometimes weakly, at multiples of $\phi = 90°$ and vanishes otherwise. This shows with more conclusiveness that, even though it appears in a GIXRD scan, this signal does not come from a randomly oriented phase, and agrees with the Si(113) origin hypothesis. Due to the imperfect match between 2θ and χ for this reflection, its intensity is diminished, bringing it to approximate parity with thin film reflections.

Besides this substrate signal, we identify several diffraction peaks from the films, which are consistent with the presence of α-quartz [212] and α-cristobalite [197]. The α-cristobalite peaks are more widely present than those of α-quartz, appearing in all samples with Sr content between 0 and 10%. The relative fraction of α-quartz phase is largest for the 2.5% sample. Using the integrated peak area for α-quartz and α-cristobalite low-angle reflections, we roughly estimate the quartz-to-cristobalite molar ratio to be 1.9 in the $x = 2.5\%$ sample, and 0.6 in the $x = 2\%$ sample, which has a visibly weaker quartz peak.

There are also other peaks, most obvious below 20°, which do not belong to the common SiO_2 phases, but most likely to strontium silicate and strontium tetragermanate. Specifically, the peak at 17.4° for $x = 20\%$ is close to the position where we would expect to see signal in the case of the (002) peak of monoclinic $SrSiO_3$ (strontium metasilicate[198]). Using this as a starting point, we were able to assign all the peaks in the $x = 20\%$ scan to the strongest reflections of this one Sr compound. We have seen the same phase in crystallization experiments of SiO_2/GeO_2 multilayers grown by ALD (see Figure 3.10 and Reference 205 for growth details). Some of these peaks are also present for $x = 5\%$, albeit much weaker.

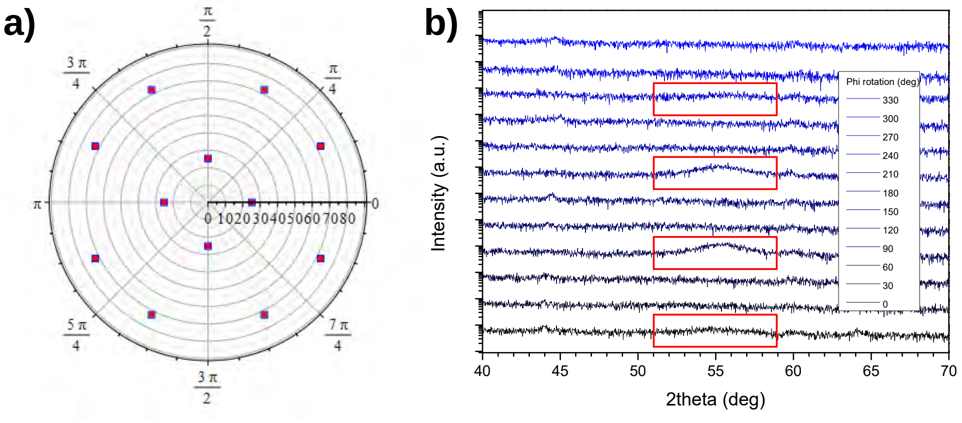

Figure 4.10: a) Simulated pole figure for the (113) reflections of a Si(100) substrate. Note that this is a polar plot, with χ in the radial direction (equidistant ticks) and ϕ in the circumference, increasing counter-clockwise. Red squares indicate poles in the upper hemisphere, and blue boxes are for poles in the lower hemisphere, thus outside the measurement range. For Si(100), the projections overlap for the upper and lower hemispheres. Simulation details available at Reference 211. b) GIXRD scans taken on a sample on Si(100) at various ϕ rotation values. The sample was realigned prior to each scan. The red rectangles highlight the signal near 56°, which is present in the 0°, 90°, 180°, and 270° scans.

With the exception of the 3% film, the remainder of the strontium-containing samples show a weak diffraction peak near 15.6°. This peak is accompanied by others, including those at 31.6° and 33.5°, which we cannot assign to strontium silicate. Similar features have, however, been observed recently on GeO$_2$ films grown on SrTiO$_3$ substrates [190], and they were assigned to a strontium germanate phase. We therefore conjecture that the diffraction peaks in our spectra belong to crystalline SrGe$_4$O$_9$ (strontium tetragermanate [213], trigonal), which matches quite well most of the observed peaks, even though we would expect a stronger signal near 24.4°.

The x = 0% scan shows weak peaks for α-quartz and α-cristobalite. Our GIXRD measurements do not, in principle, allow us to quantitatively compare the amount of crystalline phases in different samples, but AFM images of the 0% sample (Figure 4.1) reveal no obvious signs of crystallization, which hints to a much smaller crystal size than in the SrCO$_3$-containing samples. This discrepancy between micrographs and GIXRD spectra can also arise if the crystal growth begins close to the substrate-film interface, in which case it will not be immediately visible in AFM.

From GIXRD results alone a trend has not been found across the sample series. The 20% sample displays SrSiO$_3$ peaks only. The remaining Sr-containing samples show a less straightforward behavior, with the SrGe$_4$O$_9$ and SrSiO$_3$ peaks vanishing and reappearing along the series. We know that phases with uniformly random orientation are overrepresented in GIXRD with respect to oriented phases, and thus, Figure 4.11 shows an incomplete picture. Therefore, to obtain more reliable information about the crystallinity of different samples in the series we performed EBSD measurements.

The 20% sample shows electron diffraction patterns at certain points, but they do not

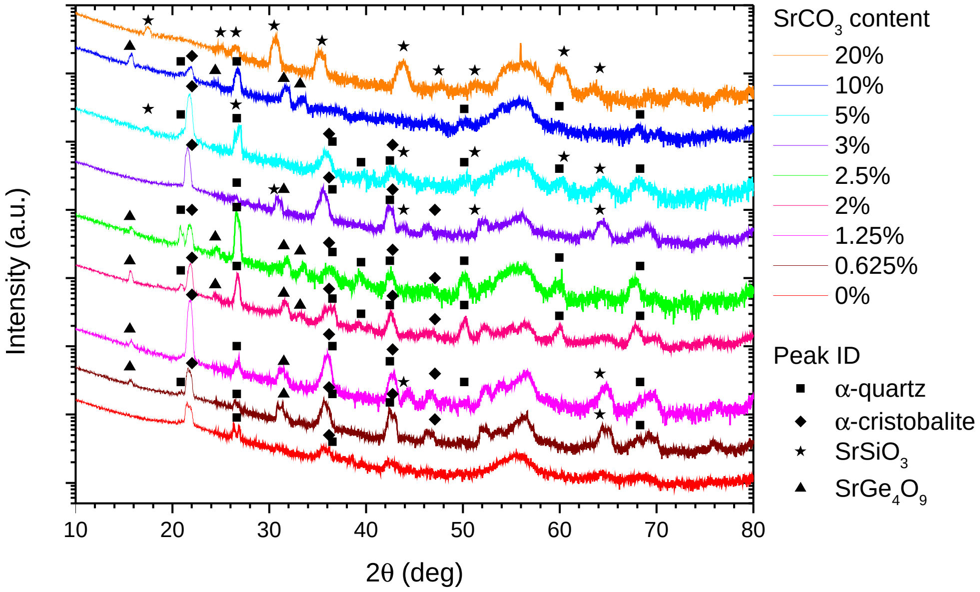

Figure 4.11: GIXRD scans of the annealed sample series.

belong to α-quartz. With this, we have no evidence of a crystalline silica phase in this sample, which suggests that the high Sr content in this sample results in the preferential formation of Sr compounds, such as $SrSiO_3$. We note that the weakly diffracting domains appear to be spherulitic [190, 214]. Figure 4.12 shows the topography and composition maps of this sample.

Lowering the Sr content, the most noticeable features of the 10% sample are long needles (see Figures 4.13 and 4.14), which also yield diffraction patterns that do not correspond to either α-quartz or α-cristobalite. However, patches of α-quartz can be found elsewhere on the sample surface. Therefore, we conjecture that the Sr concentration can locally be low enough to preclude the formation of silicate or germanate crystals, but still high enough to promote α-quartz crystalization in selected locations.

The 5% sample shows dendritic crystals, as seen in Figures 4.6b and 4.15. EBSD analysis reveals that these crystals are made of α-quartz, and that the area around them does not produce any diffraction pattern. Some Dauphiné twinning[215] is observed in the dendrites, but orientation is otherwise close to uniform within the twins, with only very small lattice rotation being present. Dauphiné twinning in α-quartz is detrimental to piezoelectric properties, and therefore to performance in many applications. Faster cooling through the β-to-α-quartz transition may reduce the extent of this twinning[215].

The dendrites have six-fold symmetry (in agreement with the α-quartz structure) and their arms longitudinal axes coincide with the <a> directions, $\langle 11\bar{2}0\rangle$. In some cases, we have observed two dendrites sharing a center and growing outward with different orientation, resulting in the apparent growth of dendrites with more than six arms.

In the 2.5% sample, we observe the formation of quartz dendrites very similar to those

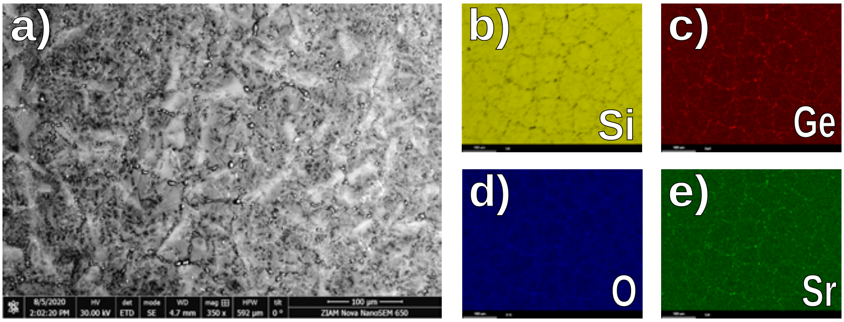

Figure 4.12: a) SEM image of a x = 20% annealed film. Annealing has a clear effect on sample topography, which suggests the growth of spherulites whose crystallinity we were not able to ascertain. b-e) EDS composition maps for the main elements in the films. From these maps, it appears that the grain boundaries are Si-depleted, which can be attributed to increased sample thickness in those regions. EDS is sensitive to signal from the Si substrate in the case of relatively thin films, and likewise if a part of the film is thicker, EDS will display proportionally higher contributions from elements in the film (which includes Si, but at a much lower atomic percent than the substrate does).

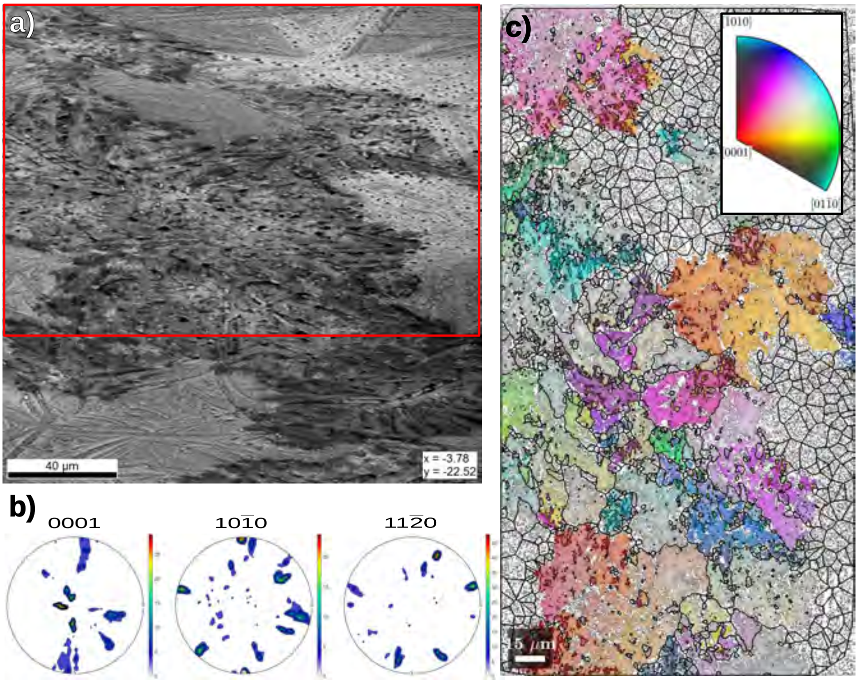

Figure 4.13: EBSD analysis of the x = 10% sample of the series. Indexing is made with the α-quartz unit cell. a) 71°-tilted SEM image of a region containing both crystalline needles and spherulites. The red rectangle shows the area analyzed with EBSD. b) ODF plotted in three different pole figures. The intensity scale is in multiples of random density (MRD). c) [0001]- IPF (Inverse Pole Figure) of the region. There is no preferred orientation overall, but the patterns show that there are quartz regions in addition to the non-quartz, long needles, which we have been unable to index.

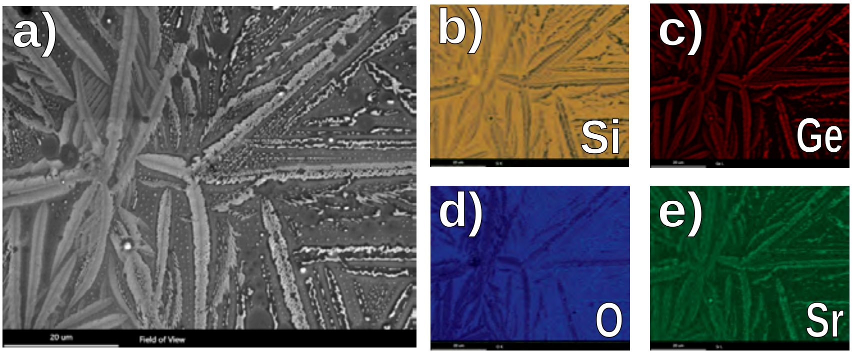

Figure 4.14: a) SEM image of an x = 10% annealed film. After annealing, needles (in light grey) of length in the tens of micrometers become visible. In regions of this type, EBSD indicates that there are no crystalline SiO_2 phases, therefore the needles might correspond to a silicate or germanate phase. b-e) EDS composition maps for the main elements in the films. The needles appear to be not only silicon poor (which can be explained by their added thickness, see Figure 4.12), but also oxygen defficient.

of the 5% sample. Interestingly, there are also non-dendritic crystalline α-quartz regions. These contain some grain boundaries and many Dauphiné twin boundaries. One of these regions is shown in Figure 4.16.

The main distinction between the dendritic and non-dendritic formations can be made on the basis of their respective ODFs (see Figures 4.15b and 4.16b). These show that a region identified as a single dendrite (Figure 4.15) has close to uniform orientation. In particular, all the dendrites that we have analyzed have their c crystal axis closer to the film normal than to the film plane. For the non-dendritic growth, it is apparent that, within a single grain formation, there can be preferred orientation for the c axis with relatively large local misorientations inside one grain (Figure 4.16b). When extending the measurement to include several spherulites, the c axis show an orientation rather uniform around the hemisphere (see Figure S13 of the Supplementary Material).

It is possible that the differences in crystallization mode are caused by inhomogeneities in the Sr concentration in the film. We propose that areas with larger concentrations of melting agent have their devitrification onset at lower temperatures. This results locally in a larger supercooling in regions with lower Sr concentration. We know that increased supercooling leads to spherulites forming preferentially over single crystals [214, 216]. Therefore, nonuniform distribution of Sr impurities can result in local variations in the crystal growth mode.

In this complex material, symmetric $2\theta/\omega$ scans, GIXRD, and EBSD together are needed to give insights about the crystallinity of the films. The lack of features in specular $2\theta/\omega$ is an indicator that no strong out-of-plane texture is present in any of the films. GIXRD scans show some α-quartz and α-cristobalite signal in the control (0% $SrCO_3$) sample after annealing, which suggests that temperature alone is enough to induce *some* crystallization.

The GIXRD cristobalite signal clearly increases with the addition of $SrCO_3$, only decreasing at 10% $SrCO_3$. The presence of quartz peaks in GIXRD is also determined by the devitrifying agent, with these peaks becoming more intense for intermediate concentra-

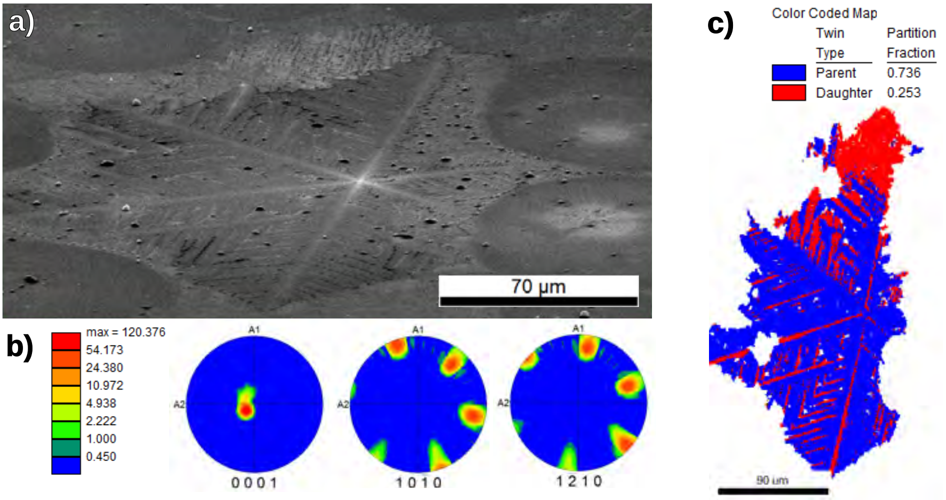

Figure 4.15: EBSD analysis of the x = 5% sample. Indexing is made with the α-quartz unit cell. a) 71°-tilted SEM image of one of the dendrites. b) Orientation Distribution Function (ODF) plotted for three different poles in scale of Multiple of Random Distribution (MRD) indicates a single crystal with [c] direction almost perpendicular to the sample surface (A3 axis). c) EBSD map of the dendrite from a), whose lateral size is a few hundred micrometers. Map demonstrates the presence of two Dauphiné twin-related orientations inside dendrite. No other grain boundaries (>3° misorientation between neighboring pixels) are present.

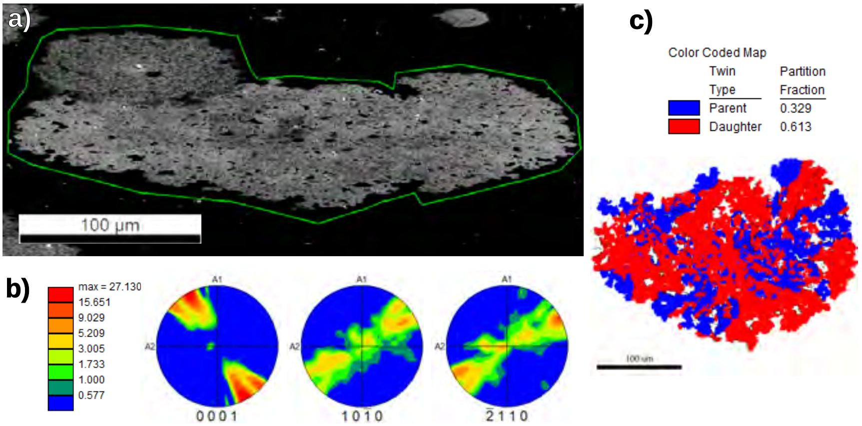

Figure 4.16: EBSD analysis of a x = 2.5% sample. Indexing is made with the α-quartz unit cell. a) 71°-tilted SEM image of a crystalline, non-dendritic region. b) ODF plotted in three different pole figures. The [0001] figure shows a certain orientation, tending to a single in-plane direction. c) EBSD map of the region, showing that the entire formation is 200-300 μm in size, the twinned regions are smaller. There are some grain boundaries present (black lines). The distribution of Dauphiné twins is more disorderly than in the dendritic areas.

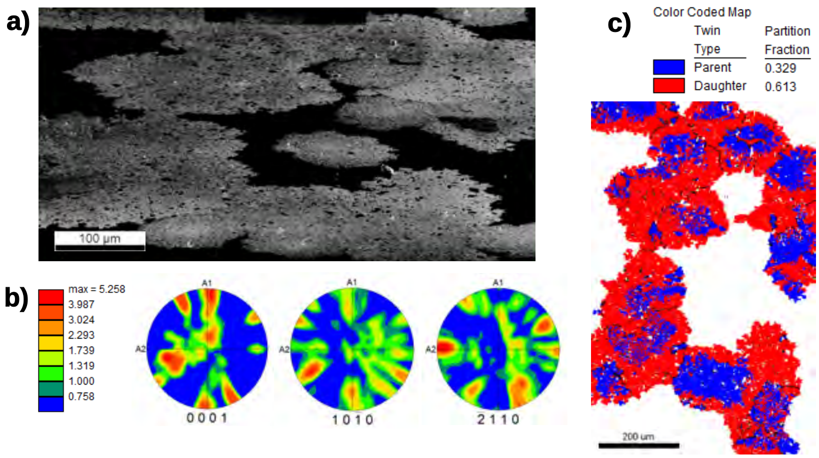

Figure 4.17: EBSD analysis of the x = 2.5% sample of the series, including multiple coagulated islands. Indexing is made with the α-quartz unit cell. We have not been able to index the region between the islands. a) 71°-tilted SEM image of a crystalline, non-dendritic region. b) ODF plotted in three different pole figures shows the presence of a few grains (~5) with different orientations. c) EBSD map of the region showing parent and daughter twinned areas. Grain boundaries indicated with black lines separate islands with different crystal orientations.

tions. The 20% sample does not show any silica peaks, either from quartz or cristobalite. We show that $SrCO_3$ does act as a devitrifying agent and promotes the crystalline silica phases, but in large amounts forms silicates and germanates instead. This is supported by the EBSD observations of the x = 2.5% and 5% samples, which show 100-μm scale α-quartz structures with varying degrees of orientation and twinning. Only α-quartz, and no α-cristobalite, was found by EBSD. This discrepancy with the X-ray diffraction results is most likely due to the surface sensitivity of EBSD. Optical microscopy (Figures 4.6 and S6) confirms the formation of microscopic crystals for Sr concentrations above 0.625%. The 3% sample is anomalous in both GIXRD and optical microscopy measurements (see Figures 4.11 and S6). Its behavior, more similar to that of samples with $x < 2\%$ could be explained by a strongly inhomogeneous Sr distribution across the film.

We note, therefore, that low concentrations of $SrCO_3$ are required for the crystallization of partially-oriented α-quartz and in order to avoid the formation of strontium silicates or germanates. It is also clear from our observations that the crystallization behavior is not uniform across the sample surface (~ 5x5 mm^2), with the 2.5% sample showing both dendritic *and* spherulitic growth. This is most likely due to inhomogeneous distribution of Sr during film growth. This could be solved in the future by growing similar structures using Atomic Layer Deposition (ALD) as multilayers of SiO_2 and GeO_2 [205], including intermediate layers of SrO.

Barring the highest $SrCO_3$ concentrations, we are able to crystallize silica phases. As the interest is in piezoelectric properties, it is desirable to grow α-quartz preferentially over α-cristobalite. The growth of α-cristobalite, while indicative in part of the effectiveness of the devitrifying agent, competes directly with the growth of α-quartz. In order to avoid the cristobalite phase, lower temperatures might be required. This may be challenging, as similar experiments of pure GeO_2 films on sapphire substrates suggest that lowering the temperature can result in spherulitic (rather than dendritic) α-quartz formation[190]. Nevertheless, the appearance of the two competing silica phases in the XRD spectra, together with the nonuniform crystallization behavior observed in optical and electron microscopy (including EBSD), clearly sets the requirement for a better method to distribute the $SrCO_3$ impurities throughout the film.

The crystallization behavior that we observe in our samples makes them especially difficult to characterize with a single technique. EBSD is an excellent tool to analyze the sample orientation at a local scale, but it is surface sensitive and has difficulty detecting crystallites which are covered in amorphous oxide. Our XRD scans are able to detect phases comparatively deeper in the sample, however they require uniformly random orientation (GIXRD) or strong texture (specular $2\theta/\omega$). Particularly in the case of the large quartz formations that we have found (Figures 4.15 and 4.16), they fall into an intermediate regime, and thus are only clearly visible with EBSD. The cristobalite phase that appears in most of the samples described in this manuscript is either present in very small crystallites or buried under other phases, and therefore only present in GIXRD scans. Future work with this type of samples will require an experimental technique that can efficiently overcome some of the limitations mentioned so far. One such technique could be micro XRD [217, 218], which has the ability to penetrate deeper into the film, and, provided that the crystallite size is large enough, could permit local (if complicated) phase and orientation analysis, allowing efficient mapping of the samples crystallization behavior.

4.4. CONCLUSIONS

We have demonstrated the efficacy of $SrCO_3$ as a melting agent to trigger SiO_2/GeO_2 crystallization on silicon at accessible process temperatures. We show that dendritic α-quartz can grow at small $SrCO_3$ concentrations of around 2-2.5%, avoiding the appearance of $SrSiO_3$ and $SrGe_4O_9$, which become the prevalent phases when the melting agent reaches 10% and 20% atomic concentrations. We observe a certain heterogeneity in crystal formation at different points of a sample, which suggests that a more uniform distribution of the melting agent is necessary.

4.5. AUTHOR CONTRIBUTIONS

This work is a collaboration between the University of Groningen (UG) and the University of Twente (UT) under the NWO TOP-PUNT programme "Searching for the Si of piezoelectrics". J. Antoja-Lleonart (UG) and B. Noheda (UG) coordinated the work. J. Antoja-Lleonart carried out the sample synthesis, characterization and modelling, wrote the manuscript and took part in discussions. V. Ocelík (UG) and S. Zhou (UG) collected and analyzed the EBSD and EDS data, and took part in discussions. K. de Hond (UT) performed the X-ray photoelectron spectroscopy and analysis, and took part in discussions as well. G. Koster (UT), G. Rijnders (UT), and B. Noheda all took part in discussions. All coauthors were involved in text revisions.

5

PLD GROWTH OF HfO_2-ZrO_2

Ultrathin $Hf_{1-x}Zr_xO_2$ films have attracted tremendous interest since they show ferroelectric behavior at the nanoscale, where other ferroelectrics fail to stabilize the polar state. Their promise to revolutionize the electronics landscape comes from the well-known Si compatibility of HfO_2 and ZrO_2, which (in amorphous form) are already used as gate oxides in MOSFETs. However, the recently discovered crystalline ferroelectric phases of hafnia-based films have been thus far grown on Si only in polycrystalline form. Better ferroelectric properties and improved quality of the interfaces have been achieved in epitaxially grown films, but these are only obtained on non-Si and buffered Si(100) substrates. Here, we report direct epitaxy of polar $Hf_{1-x}Zr_xO_2$ phases on Si, enabled via in situ scavenging of the native amorphous silica (a-SiO_x) layer by Zr (Hf), using pulsed laser deposition under ballistic deposition conditions. We investigate the effect of substrate orientation and film composition to provide fundamental insights into the conditions that lead to the preferential stabilization of polar phases, namely, the rhombohedral (r-) and the orthorhombic (o-) phases, against the nonpolar monoclinic (m-), on Si.

This chapter includes content published as:
Pavan Nukala, Jordi Antoja-Lleonart, Yingfen Wei, Lluís Yedra, Brahim Dkhil, Beatriz Noheda, *ACS Applied Electronic Materials*, **2019**, *1 (12)*, 2585–2593.

5.1. INTRODUCTION

Ferroelectric hafnia-based thin films [219] have by now been established as the most promising materials to realize the potential of ferroelectric phenomena in real devices [86, 220]. Their Si compatibility, simple chemistry, and unique ferroelectricity, which becomes more robust with miniaturization, is tailor-made for microelectronics, offering ready-made alternatives to conventional ferroelectrics that lack all these attributes [87, 89, 98, 221–226]. Such distinguishing characteristics have led to an upsurge in application-oriented research as well as in curiosity-driven fundamental research to solve questions such as why these materials are capable of sustaining the unconventional ferroelectricity [90, 93, 227–244], how these materials negate the effects of depolarization fields [245, 246] and whether such a new type of ferroelectricity can be replicated in other simple oxide systems.

A prominent feature of hafnia-based materials is polymorphism [246]. While the ground state in the bulk HfO_2 is a nonpolar monoclinic (m-, $P2_1/c$) phase, a plethora of lower-volume, polar and nonpolar, metastable states can be accessed at ambient conditions via a combination of strategies such as cationic and anionic doping [219, 228–230, 232, 235], thermal and inhomogeneous stresses [247, 248], nanostructuring [249], epitaxial strain [42, 229, 232, 237, 241, 243, 244, 250–252] and oxygen vacancy engineering [253, 254], all of which can be suitably engineered into thin-film geometries. Based on first-principles calculations [42, 236, 255, 256] at least five polar polymorphs (with space groups $Pca2_1$, Cc, $Pmn2_1$, R3, and R3m) can be identified as those that can be experimentally obtained. Owing to its relatively low energy, the orthorhombic (o-) $Pca2_1$ phase is widely observed in hafnia-based films grown via atomic layer deposition (ALD) [90, 219, 228, 238], chemical solution deposition (CSD) [231], RF sputtering on Si [239, 242], and pulsed-laser deposition (PLD) on selected substrates [229, 234, 240, 244, 250–252]. A slightly higher energy rhombohedral (r-) phase (R3m or R3 [236]) has been recently observed on epitaxial $Hf_{0.5}Zr_{0.5}O_2$ films grown on $SrTiO_3$ (STO) [42]. The r-phase is stabilized by a combination of the large internal pressure of the nanoparticles (induced by surface energy) and the substrate-imposed compressive strain. The epitaxial growth of the r-phase has enabled the observation of high values of remanent polarization (P_r = 34 $\mu C/cm^2$) [1] in HfO_2-ZrO_2 systems, although they showed larger coercive fields than films in the polar o-phase.

So far, polar phases have been successfully obtained via epitaxial synthesis techniques (PLD) on a variety of substrates: perovskites [237, 250–252] (including buffered STO on Si(001)) [252], fluorites [229, 240, 244], and hexagonal substrates [257]. However, the advantages gained by epitaxy (i.e. single phase materials with enhanced polarizations) are offset by the fact that none of these films are grown directly on Si, despite the Si integrability of hafnia-based systems. It is in this context that we explore for the first time the epitaxy of polar polymorphs in $Hf_{1-x}Zr_xO_2$ (HZO100x) films directly on Si.

The direct epitaxial growth of oxides on Si is complicated by the presence of a very thin amorphous native oxide layer, which prevents the transfer of texture from the substrate to the film. This interfacial layer can be removed prior to deposition through hydrofluoric acid (HF) etching, which lowers the crystalline quality [258, 259]. However, the epitaxial growth of yttria-stabilized zirconia (YSZ) on Si(100) is a mature process [260–263], as witnessed by the fact that YSZ-buffered Si(100) substrates are commonly used for the growth

---

[1] Highest value at the time of writing the original manuscript.

of high-T_c superconductors and other functional layers [264–268]. The problem of native oxide in YSZ on Si is solved via an in situ scavenging process. Since the formation energy of ZrO_2 (Y_2O_3) is less than that of SiO_2, Zr (Y) chemically reacts with a-SiO_2, forming a crystalline seed of ZrO_2(Y_2O_3) directly on Si, with an epitaxial relation [259, 266, 269]. In other words, the scavenging process involves one (or both) of the following decomposition chemical reactions.

$$SiO_2 + Zr \rightarrow Si + ZrO_2 \tag{5.1}$$

$$2SiO_2 + Zr \rightarrow ZrO_2 + 2SiO \uparrow \tag{5.2}$$

As a consequence of this scavenging process, the native a-SiO_x layer is replaced by ZrO_2 (Y_2O_3). The rest of the YSZ growth follows the template set by the crystalline ZrO_2 seed, resulting in a very high crystalline quality. The regrowth of the a-SiO_2 oxide (backward reactions 5.1 and 5.2, upon increasing the amount of product) and generation of misfit dislocations contribute to strain relaxation in thicker layers of YSZ. Inspired by the success of direct epitaxy of a sister compound YSZ on Si, here, we report successful growth of epitaxial polar phases of HfO_2-ZrO_2 alloys directly on Si(111) and Si(100).

5.2. EXPERIMENTAL

PLD was used for the deposition of HZO100x with x = 0.5, 0.7, and 0.85 on p-doped Si(111) (resistivity < 0.005 Ωcm), and Si(100) (resistivity < 0.03 Ωcm). Targets of the desired compositions (x = 0.5, 0.7, 0.85) were prepared through standard solid-state synthesis starting from powders of HfO_2 (99% purity) and ZrO_2 (99.5% purity). A KrF exciplex laser (λ = 248 nm) was used for target ablation at a fluence of 1.1 J/cm^2. A base pressure of 10^{-7} Torr was maintained in the deposition chamber. The target-to-substrate distance was fixed at 50 mm. HZO layers were deposited at 800°C with the flow of Ar (5 sccm) at a process pressure of 0.005 mbar and laser repetition rate of 7 Hz. The choice of target-substrate distance, as well as the low pressure conditions, ensured a ballistic mode of deposition, preventing the oxidation of atomic species (Hf, Zr ions) in the plasma itself. It is indeed crucial for the interfacial scavenging reactions that species transported to the substrate are Hf, Zr, and O ions with no ionized HfO_2 and ZrO_2 present in the plasma. The 7 Hz repetition rate favors nucleation-dominated kinetics or, in this case, the occurrence of interfacial scavenging at multiple locations, and thus the generation of several (Hf)ZrO_2 seeds or growth templates. On Si(111), HZO (x) films of 10 nm thickness with three different compositions (x = 0.5, 0.7, 0.85) were deposited, at a growth rate of 0.7 Å/s. On Si(100), films of 5, 10, and 20 nm were deposited with composition x = 0.7, at a growth rate of 0.9 Å/s.

Thickness was confirmed both directly, with scanning transmission electron microscopy (STEM), and indirectly, with X-ray reflectivity (XRR) measurements. Information about global structure, symmetry, phase-mixing, and domains was inferred from X-ray diffraction (XRD) with a Cu Kα source. Texture analysis was performed via χ-ϕ (pole figure) scans at $2\theta \approx 30.0°$ (approximately corresponding to the d_{111} of the low-volume phases) and at $2\theta \approx 34.5°$ (approximately corresponding to the d_{200} of all the polymorphs). Table 5.1 provides the 2θ values that are expected of some of the relevant low-index planes in the three main HZO phases discussed in this work. The d-spacings of the poles obtained from the χ-ϕ equal area projections were more precisely analyzed through $2\theta/\omega$ scans around them.

Table 5.1: Calculated 2θ values for different Bragg spots as they are expected in monoclinic, rhombohedral and orthorhombic HZO for CuKα radiation.

2θ (deg)	**200**	**020**	**002**	**111**	**$\bar{1}11$**	**$1\bar{1}1$**	**$11\bar{1}$**
Monoclinic ($P2_1/c$)	35.47	34.98	34.37	28.49	31.71	28.40	31.71
Rhombohedral (R3)	35.15	35.15	35.15	30.26	30.33	30.33	30.33
Orthorhombic ($Pca2_1$)	35.82	34.20	35.09	30.23	30.23	30.23	30.23

Local structural characterization and phase analysis was performed through STEM imaging at 200 kV (Titan G2 and Themis). STEM images were obtained in both high-angle annular dark field (HAADF) mode, and bright-field (BF) mode. Chemical maps were generated via energy dispersive spectroscopy (EDS) in a four-detector ChemiSTEM setup on the Titan G2 aberration-corrected electron microscope.

5.3. RESULTS AND DISCUSSION

$Hf_{1-x}Zr_xO_2$ on Si(111). *Strongly textured (111) Films.* Pole figures obtained from films of HZO50 and HZO70 (Figure 5.1a), as well as HZO80 (Figure 5.2a) at about 2θ = 30.0° look qualitatively similar. In addition to the peak at the center (out-of-plane), there are three poles (P1-P3) arising from the film at $\chi \sim 71°$ separated from each other in ϕ by ~ 120°. The weaker poles at $\chi \sim 71°$ (Figure 5.1a) are from the tail of the substrate peak at 2θ = 28.44°. This symmetry is consistent with ⟨111⟩-oriented films, following the substrate. Quite interestingly, the {111} poles corresponding to the substrate and the film are rotated 180° about the substrate normal.

Phase coexistence and evidence of r-phase. On the HZO50 films, the $2\theta/\omega$ scans across P1-P3 clearly show two peaks at every pole centered with 2θ = 28.5° and 31.4° (Figure 5.1b), corresponding to d_{111} and $d_{11\bar{1}}$ of the bulk nonpolar m-phase. With the increase of Zr concentration to x = 0.7 (arrow in Figure 5.1c), a peak corresponding to a low-volume phase starts to appear at 2θ = 30.23°, with the majority phase still being monoclinic. A further increase in Zr concentration changes the predominant phase of the film to this low-volume phase, with a very minor fraction in the m-phase (Figure 5.1d). To determine the symmetry of the low-volume phase for the films with x = 0.85, a three-peak Gaussian fitting was performed to the $2\theta/\omega$ plots from P1, P2, and P3 between 2θ of 27° and 33° (Figure 5.2b,c. Only P1 shown here). The peak position representing the low-volume phase is at $2\theta = 30.24 \pm 0.03°$ for P1, P2, and P3 whereas the out-of-plane peak P0 is at $2\theta = 30.12 \pm 0.04°$. These positions (and errors) are shown in isolation in Figure 5.3a,b.

Such a 3:1 degeneracy in peak positions or d_{111} is indicative of the low-volume phase having a rhombohedral symmetry, a phase which was discovered on films grown epitaxially on STO substrates [42]. In other words, $(11\bar{1})$, $(1\bar{1}1)$, and $(\bar{1}11)$ all have the same d-spacing, which is smaller than the (111) d-spacing along the surface normal. In orthorhombic, tetragonal, or cubic phases, all four of them would have the same d-spacing, whereas in a monoclinic phase there is a 2:2 degeneracy in these peak positions. The d_{111} and $d_{11\bar{1}}$ can be calculated to be 2.96 ± 0.01 Å for P0 and 2.95 ± 0.01 Å for P1-P3, which

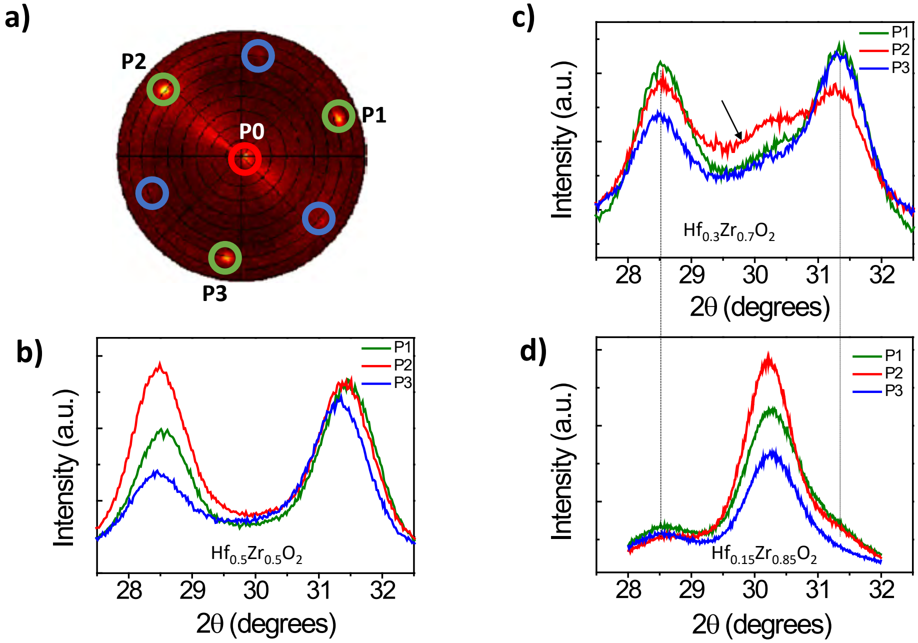

Figure 5.1: Texture and phase analysis on 10 nm (1-x)HfO_2:xZrO_2 films (HZO100x) for three different compositions (x = 50, 70, and 85) grown on Si(111). a) Representative pole figure obtained at about $2\theta = 30°$ on a HZO70 film, consistent with $\langle 111 \rangle$ out-of-plane texture. The out-of-plane {111} pole is labeled P0 and encircled in red. This pole is common to the film and the substrate. The three non-out-of-plane film {111} poles, P1-P3, are centered at $\chi \approx 71°$ and separated in ϕ by 120°. These are highlighted with green circles in the figure. Rotated 180° from the film pattern, we see weak spots arising from the tail of substrate {111} poles $2\theta = 28.44°$, this time highlighted with blue circles. Pole figure symmetry looks similar for HZO50 and HZO85 (Figure 5.2). Pole figure symmetry looks similar for HZO50 and HZO85. $2\theta/\omega$ scans are shown around P1, P2, and P3 for HZO50 (b), HZO70 (c), and HZO85 (d). While HZO50 shows just the monoclinic {111} peaks, a low-volume phase peak (indicated by an arrow) starts evolving from HZO70 at $2\theta \approx 30.2°$ and intensifies for HZO85.

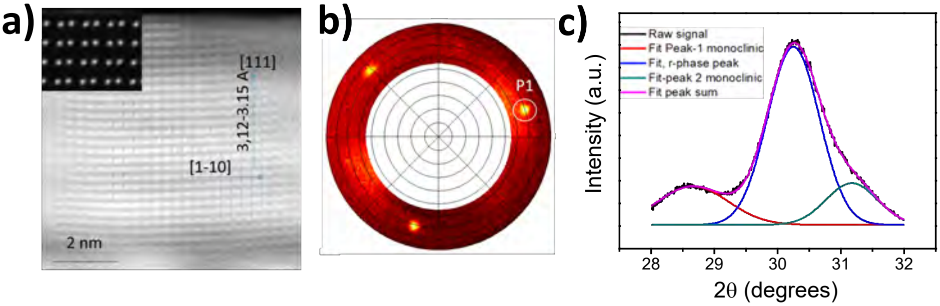

Figure 5.2: a) HAADF image acquired along the [-211] zone axis of a 20 nm-thick, HZO50 film, clearly showing [111] texture. Inset shows the HAADF image simulation of the monoclinic phase in this zone, which matches with our experimental patterns. b) Pole figure from HZO85, films grown on Si(111) around $2\theta \approx 30°$, corresponding to {111} planes of HZO. This pole figure looks very similar to the ones obtained at x = 0.5 and 0.7 compositions (Figure 5.1a), and it is consistent with [111]-oriented films. c) The fitting procedure on the pole-slice of P1 in b) is shown here. The raw signal between $2\theta \approx 28°$ and 32° is fit to three Gaussians centered at 28.55° (red, monoclinic (111)), 30.24° (blue, low-volume phase (111)), and 31.20° (green, monoclinic (11$\bar{1}$)). From these fits on all the three poles (P1-P3) and the out-of-plane peaks, the ones corresponding to the low-volume phase are selectively shown, and further analyzed, in Figure 5.3. The 3:1 multiplicity in the {111} peaks of the low-volume phase clearly show that it is rhombohedral.

are almost equivalent within error. Consequently, this corresponds to a nearly cubic unit cell with a = b = c ~ 5.11 ± 0.01 Å and rhombohedral angle (α) between 89.9° and 90°. This distortion is smaller than what was observed by Wei et al. on 10 nm-thick HZO50 films grown on STO ($\alpha \sim 89.3°$) [42]. In summary, the nondegeneracy of the four peak positions points to a rhombohedral phase, but with a rather small distortion that requires further proof, which follows in this text.

Before that, a comment is necessary about the dispersion in the reported peak positions. Errors in $2\theta/\omega$ scans can occur through slight misalignment and inhomogeneous strain, and we detail our determination of these errors in Figure 5.3c. The alignment procedure for pole-slicing works on the basis of selecting the values of χ and ϕ (also ω-offset) at which the intensity of the Bragg peak is maximum. However, changing from these conditions amounts to misalignment. Slight misalignments (i.e. in χ) can change the peak position of the low-volume phase owing to effects concerning inhomogeneous strain, which in turn introduces an error to the results of our Gaussian fits. It is important to quantify this error, because our phase allocation depends largely on the multiplicity obtained from peak positions. In Figure 5.3c, we quantify the changes in the peak positions of the low-volume phase that occur upon deliberate misalignment. Pole slices were collected from P1 of Figure 5.2a in the HZO85 sample at various values of χ, and peak positions were obtained from a corresponding Gaussian fitting procedure of these slices (described in Figure 5.2). We do notice that the misalignment induces a spread in the values of peak positions by $\Delta(2\theta)$= 0.06°, which is the main source of error in the determination of the peak position. In this chapter, all the peak position data are assumed to have similar error contribution from inhomogeneous strain, which sets an overall lower bound for the actual error.

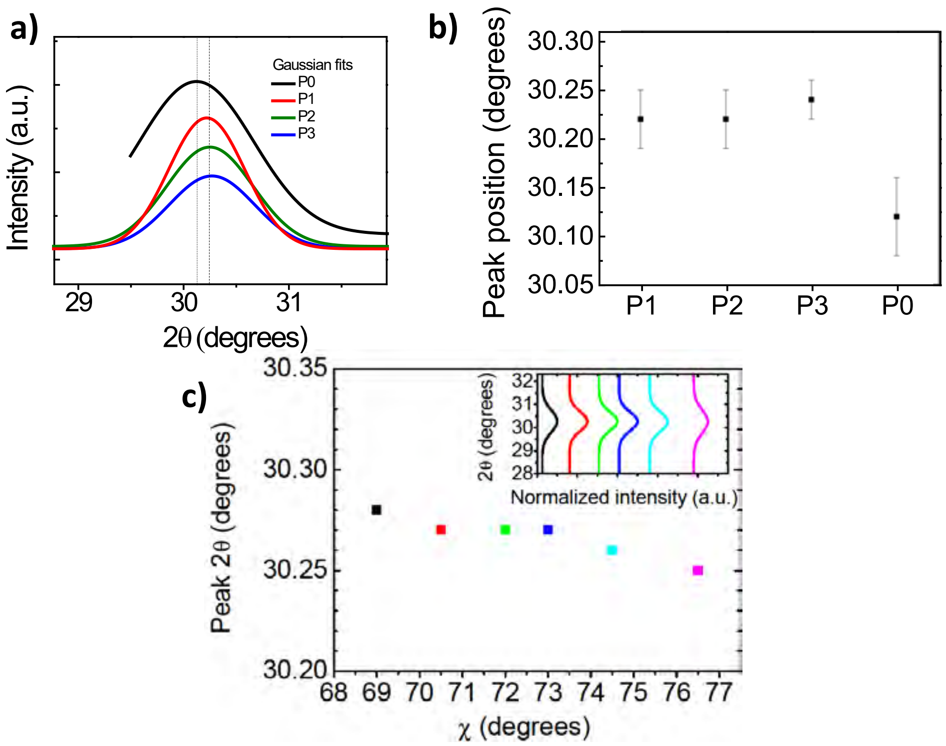

Figure 5.3: XRD determination of symmetry for the low volume phase on Si(111). a) Single Gaussian fits for the low-volume phase reflections at the non-out-of-plane $\{111\}$ poles P1-P3 and the plane normal (P0) for HZO85 films (t = 10 nm). For P0, the fit is cut at lower angles to avoid the substrate signal. P0 has a maximum position clearly separate from P1-P3, as indicated by the vertical dotted line. The raw data (Figure 5.1d) and 3-peak fitting procedure (two monoclinic, and one low-volume phase) are shown in Figure 5.2b. b) Peak positions of P1-P3 compared to P0 obtained from a). This clearly reveals a 3:1 degeneracy in peak positions, or an r-phase. c) Error analysis for inhomogeneous strain. The inset shows $2\theta/\omega$ scans taken at χ values around the P1 pole of Figure Figure 5.2a. The peak positions are plotted here as a function of the χ value, showing that small misalignments in χ induce an error in 2θ.

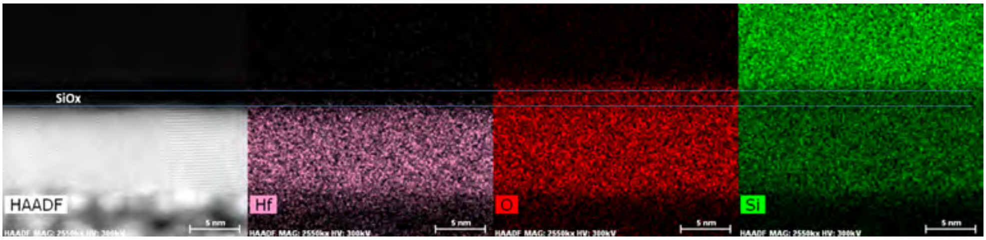

Figure 5.4: Representative EDS elemental maps of HZO (x = 0.5) thin films. Hf, O, and Si elemental maps here are from a region shown in HAADF-STEM image on the left. These maps clearly show the existence of a contiguous a-SiO_x (regrown) layer of less than 1 nm between the substrate and the film. The regrowth of a-SiO_x in the later part of the growth process relaxes the strain on HZO stabilizing it in a bulk monoclinic phase. This is exactly what we see on these films with x = 0.5. They completely stabilize in a monoclinic phase. On samples with x = 0.7, we can clearly identify regions with and without regrown a-SiO_x. The film above the regions with a-SiO_x is monoclinic, and without the regrown SiO_x it is rhombohedral. Thus regrowth of a-SiO_x seems to be predominant mode of strain relaxation in HZO systems.

HAADF-STEM images acquired on cross-sectional samples of HZO50 films clearly show that the entire film is in the monoclinic (nonpolar) phase, consistent with the XRD data (Figure 5.1b). EDS analysis shows a contiguous layer of amorphous a-SiO_x of thickness apporoximately 0.5 to 1 nm between Si and the HZO layer (Figure 5.4). This is a reformed oxide layer, a result of the backward reaction upon increasing the product concentration in the scavenging chemical reactions 5.1 and 5.2. With Zr concentration increased to x = 0.7, this a-SiO_x layer exists in some regions but is absent in some other regions (Figure 5.5a), a result of either the better scavenging properties of Zr ions compared to Hf ions or sluggish reduction kinetics of zirconia compared to hafnia.

Very interestingly, upon analyzing the d_{111} lattice parameters, we find that the film just above the regions with the a-SiO_x layer displays a monoclinic nonpolar phase ($d_{11\bar{1}} \sim 2.82$ Å, $d_{111} \sim 3.13$ Å), while the film directly in contact with Si substrate is in the low-volume phase (Figure 5.5a, zoomed in Figure 5.5b). HAADF-STEM multislice image (200 kV) simulations (Figure 5.5c) obtained from the rhombohedral (R3) phase (cross-sectional sample thickness ≈ 20 nm), among all the other polymorphs, show the closest resemblance to our images. In particular, the alternating intensity of the cationic columns along the ⟨112⟩ direction is a distinct feature of the rhombohedral polar phases (both R3 and R3m), which can be seen in our experimental images (Figure 5.5a,b).

Interfacial phase and epitaxy. At the interface between Si and r-phase HZO, we observe at least two monolayers of crystalline phase, which is different from both the Si and HZO structures, as shown in the bright-field STEM image in Figure 5.6a (contrast digitally inverted). This is most likely a crystalline phase of SiO_2, tridymite or β-cristobalite, which has been studied in detail at the Si/a-SiO_x interfaces and is well-known to induce epitaxy between Si and YSZ layers [259, 270–272]. In Figure 5.6b, we propose a rough schematic for epitaxy, based on Figure 5.6a, assuming the lattice parameters of the β-cristobalite as the crystalline c-SiO_2 phase (in-plane ≈ 3.55 Å). Epitaxy of HZO (in-plane ≈ 3.6 Å) on c-SiO_2 thus provides initial compressive strain boundary conditions.

These results enable us to propose that the phase of the initial seed formed as a result of scavenging the native oxide is the low-volume r-phase. The compressive strain condi-

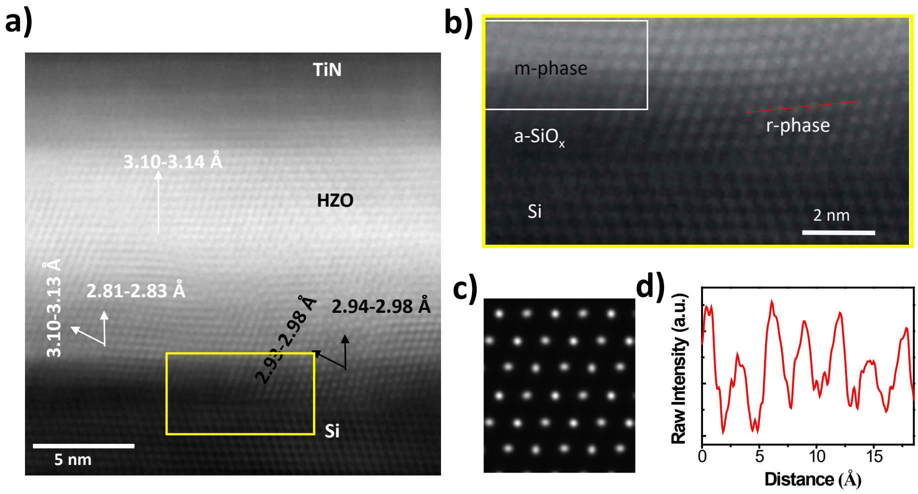

Figure 5.5: STEM determination of symmetry for the low volume phase on Si(111). a) Cross-sectional HAADF-STEM image of a TiN-HZO70(t = 10 nm)-Si metal-insulator-semiconductor (MIS) capacitor (obtained along the $\langle 1\bar{1}0\rangle$ zone of the substrate), showing various {111} d-spacings. $d_{11\bar{1}} = 2.81 \pm 0.02$ Å, and $d_{111} = 3.11 \pm 0.02$ Å. b) Zoomed-in look at the Si-HZO interface, boxed in yellow in a). The interface with Si on the left contains regrown a-SiO$_x$ (<1 nm). We clearly see an m-phase right above it. The region on the right has no a-SiO$_x$, but instead a direct connection between HZO and the crystalline substrate. That is a low-volume phase. c) R3 phase HAADF-STEM multislice image simulation at lamella thickness of ~ 20 nm (defocus ~ 0). This is clearly in agreement with our observations. d) Contrast fluctuations along the red line (one of the $\langle 112\rangle$ directions) in b). These fluctuations do not appear in the o- or t-phase, and are quite unique to the r-phases (as can be seen visually in c).

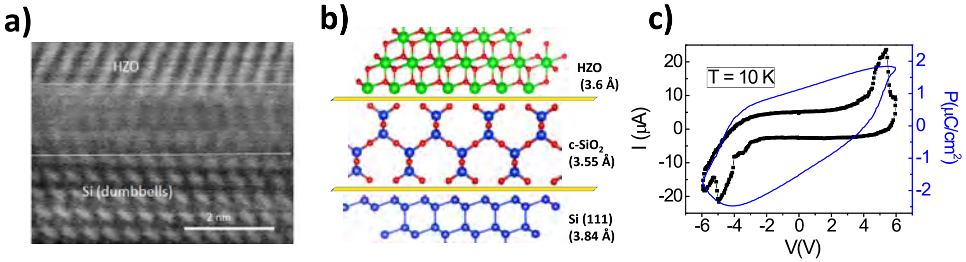

Figure 5.6: Interface structure and epitaxy on Si(111). a) Bright-field (BF) cross-sectional STEM image with inverted contrast of the interface. BF mode provides better contrast for lighter elements, and thus, this mode of imaging is being reported. Clearly, we see 2-3 monolayers of interface phases. b) Schematic of growth on Si, with β-cristobalite at the interface. It provides the compressive strain necessary to stabilize the r-phase on HZO. c) I-V, and corresponding P-V loops obtained from the MIS capacitor structure of TiN-HZO70-Si at 1000 Hz, and 10 K. Although quite leaky on the inversion side (negative voltage), we nevertheless see switching peaks in the I-V curves. P_s is quite low, since the majority of the film is in a nonpolar monoclinic phase. However, this is a proof-of-concept that the r-phase is indeed polar.

tions stabilize the r-phase, quite similar to HZO films grown on STO [42]. However, regrowth of the amorphous oxide layer relaxes the strain, stabilizing the nonpolar m-phase [259]. Increasing the Zr content increases the efficiency of the native oxide scavenging, thus stabilizing a greater volume of the film in the r-phase.

Polar nature of the r-phase. Metal-insulator-semiconductor (MIS) capacitors were fabricated on these films with TiN circles (200 μm diameter) as the top-electrode. These were quite leaky, especially in the inversion regime of operation. Cooling the devices to 10 K reduced the leakage, despite not completely avoiding it. On the HZO70 films, very weak polarization switching (evident from the I-V loop) was observed with ΔPs of $\approx$2 μC/cm^2 (Figure 5.6c), with devices tested at 1000 Hz. While the device optimization and rigorous electrical characterization is a subject of future work, these measurements demonstrate that the r-phase is indeed polar. About the weak ferroelectric switching, apart from the fact that these samples show a predominant fraction of nonpolar m-phase, it must also be noted that the rhombohedral angle in our samples is very close to 90°. First-principles calculations [42] show that, at these low distortions, the phase with R3m symmetry has very low Ps ~ 1 μC/cm^2.

$Hf_{0.3}Zr_{0.7}O_2$ on Si(100). Textured {100} films and thickness dependence. Films were also grown on (100)-oriented silicon. Figure 5.7a shows the pole figure measured at 2θ = 30.5° for a 5 nm thick HZO70 film, which shows its {111} poles. The pole figure data at 2θ = 34°, which shows a 200-pole at $\chi \approx 0°$ (Figure 5.7b), and therefore it is evident that these films are strongly textured with {100} planes parallel to the Si(100) surface. On 10 nm thick films (Figure 5.7c,d), along with all the poles observed for the 5 nm films, some extra satellites appear. Specifically, two satellites appear at $\chi \approx 58°$ for every intense {111} pole (at $\chi \sim 53°$) separated in ϕ by ~ 7° (Figure 5.7c). About the intense center {100} pole, 4 different satellites appear centered at $\chi \approx 8°$ (with a spread of 8-10°) separated in ϕ by 90° (Figure 5.7d). These satellites hint to domains/grains where the {100} planes are misoriented with respect to the Si(100) surface. As the thickness of the film increases to 20 nm (Figure 5.7e,f), poles from these misoriented grains become the most intense, and the signal from the domains with {100}//Si(100) domains almost disappears.

This rationale is displayed visually in Figure 5.8. In this figure, simple pole figure simulations are shown for single-domain films of monoclinic and orthorhombic hafnia at the same 2θ angles as Figure 5.7. The domain orientations that give rise to these pole figures are shown schematically in Figure 5.7c. In the simulations, the red squares indicate a pole on the northern hemisphere ($0^o < \chi < 90^o$) and the blue boxes indicate one on the southern hemisphere ($90^o < \chi < 180^o$) of the samples, thus not accessible in our measurements. Poles located in the equator are plotted in red for convenience, but in practice they are not visible in our experimental data. Only poles with 2θ values close to the ones for the measured pole figures are shown in the calculated patterns. The left column (a, c, e) displays the figures for the {111} plane family. In the monoclinic phase, this plane family shows four peaks near $2\theta = 31.71^o$, shown here, and four more at $2\theta = 28.48^o$. In the orthorhombic phase, all eight peaks are close to $2\theta = 30.12^o$. The right column (b, d, f) figures show the {002} plane family, in each case generating six peaks, four of which are at $2\theta = 35.47^o$, and two of which are at $2\theta = 34.36^o$. In all three proposed domain types, the b-axis is parallel to the a- or b-axis of the Si(100) substrate, For the first m-domain type (a, b), we additionally imposed that the ab plane be parallel to Si(001), i.e. we set the HZO(002) re-

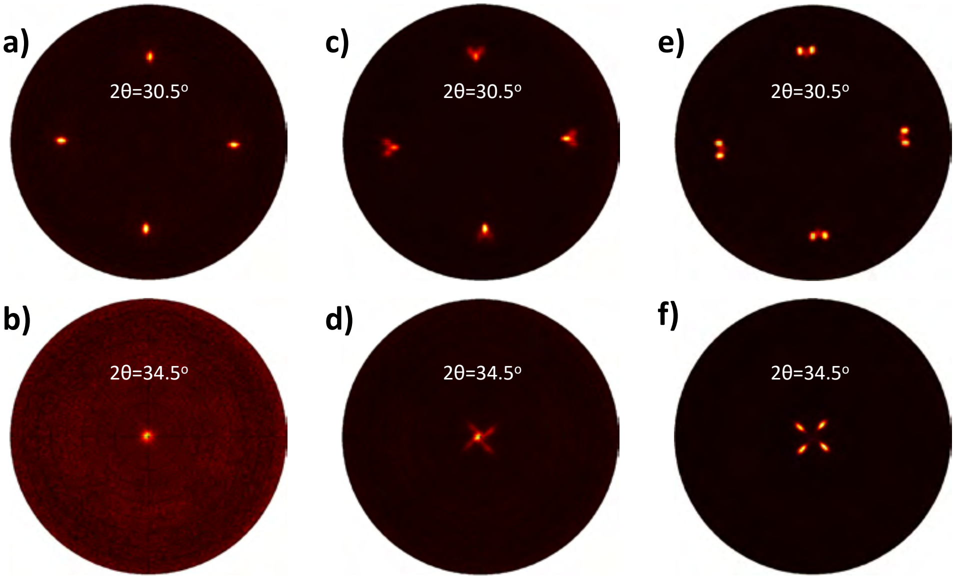

Figure 5.7: Texture measurements of HZO70 on Si(100) at different thicknesses. Pole figures obtained about $2\theta = 30.5^o$ (corresponding to d_{111}) and about $2\theta = 34.5^o$ (corresponding to d_{100}) on (a, b) 5 nm, (c, d) 10 nm, and (e, f) 20nm HZO70 films grown on Si(100). (a, b) In 5 nm-thick samples 4 {111} poles separated in ϕ by 90° are observed at $\chi \approx 53^o$, and a {001} pole at $\chi \approx 0^o$ clearly showing that the films are textured with ⟨001⟩ oriented out-of-plane. (c, d) In 10 nm-thick samples, apart from the poles observed for 5 nm, there are some extra satellite {111} poles at $\chi \approx 58^o$ forming a triangular pattern, and 4 {001} satellites centered around $\chi \approx 8^o$ (spread = 8-10°) separated in ϕ by 90°. All these patterns can be mathematically explained through the coexistence of various monoclinic domains (each contributing to a different set of poles, see Figure 5.8). (e, f) What were just satellite spots in 10 nm samples become the main Bragg spots at 20 nm thickness.

flection to have χ = 0. For the second m-domain type (c, d) we set that same reflection to instead have χ = 90º - β while holding the HZO(200) at χ = 90º, thus tilting the ab plane in such a way that the c-vector (in direct space) is perpendicular to the Si(001) plane. For the o-domain (e, f), the a-axis is pointing upward perpendicular to the substrate surface. Each of the calculated pole figures can be rotated in ϕ by multiples of 90º, thus including the contributions for four (two in the orthorhombic case) in-plane domain orientations. This provides an excellent match with the measured pole locations, particularly for the monoclinic cases, giving rise to our claim that in thin (5 nm) samples the m-HZO phase has its ab plane parallel to the substrate. In thick (20 nm) samples this is no longer the case, instead with its c-axis (in direct space) pointing perpendicular to the substrate. In intermediate (10 nm) thickness a mix of all domain types is observed.

Phase coexistence, domains, and accordions. To further learn about the lattice parameters and global symmetries, $2\theta/\omega$ scans were performed across each of the measured pole figures. Here, we discuss the results from 10 nm films on Si(100), which include all the features of both the 5 nm and the 20 nm films. Around the {111} pole (zoomed in view in Figure 5.9a), when aligned perfectly either at $\chi \approx 53°$ (pixel 1, black, in Figure 5.9a) or at the most intense spot of the satellites ($\chi \approx 58°$, gray pixels 6 and 7 in Figure 5.9a), $2\theta/\omega$ scans clearly show two distinct peaks centered at 2θ = 28.5° and 31.5° (Figure 5.9b). This is a signature of the monoclinic phase, and its corresponding domain structure. In particular, the monoclinic domains that give rise to these Bragg spots (at χ and ϕ of the pixels 1, 6, and 7 in Figure 5.9b) correspond to two types of domains: those having the a-b plane parallel to the substrate's Si(001) (dominating in thinner samples), and those with the a-b plane a few degrees misoriented from Si (001) (in thicker samples), as sketched in Figure 5.9c. The separation in ϕ of the satellites is a result of domains with positive and negative misorientation. Rigorous proof of this model through a complete mathematical analysis of the pole figure analysis is provided in Figures 5.8 and 5.10.

Figure 5.9 shows $2\theta/\omega$ scans that were performed at χ values in between the black and gray pixels, that is, purposely "misaligned". For pixels 2 and 3 (orange) and 4 and 5 (magenta), we find the emergence of a third peak at $2\theta \approx 30.2°$ in addition to the two monoclinic 111 peaks (Figure 5.9b). This corresponds to a low-volume minor phase that coexists with the major bulk monoclinic phase.

The overview cross-sectional HAADF-STEM image acquired along the [010] zone (Figure 5.11a) on the 10 nm thick film clearly shows an accordion-like domain morphology. Upon further zooming in (blue box in Figure 5.11a), we see that the domains that contribute to the zigzag pattern correspond very well to the monoclinic symmetry (HAADF-STEM simulation in Figure 5.11b). The monoclinic angle (β) varies between 95° and 99° across various domains. This variation is indeed reflected as the spread of the satellite spots about χ = 8° in the {001} pole figure (Figure 5.7d). The intersection of two domains with positive and negative misorientation (9° and -9° in Figure 5.11b) of the a-b plane with Si (001) results in the accordion morphology, consistent with the satellite spots of the{111} poles in XRD analysis. The monoclinic domains where the a-b plane is parallel to Si(001) are shown in Figure 5.12.

The region enclosed in red in Figure 5.11a, when zoomed and further analyzed, is consistent with our HAADF-STEM simulations from an orthorhombic crystal (Figure 5.11c), and not the other low-volume polymorphs (simulations of various polymorphs are com-

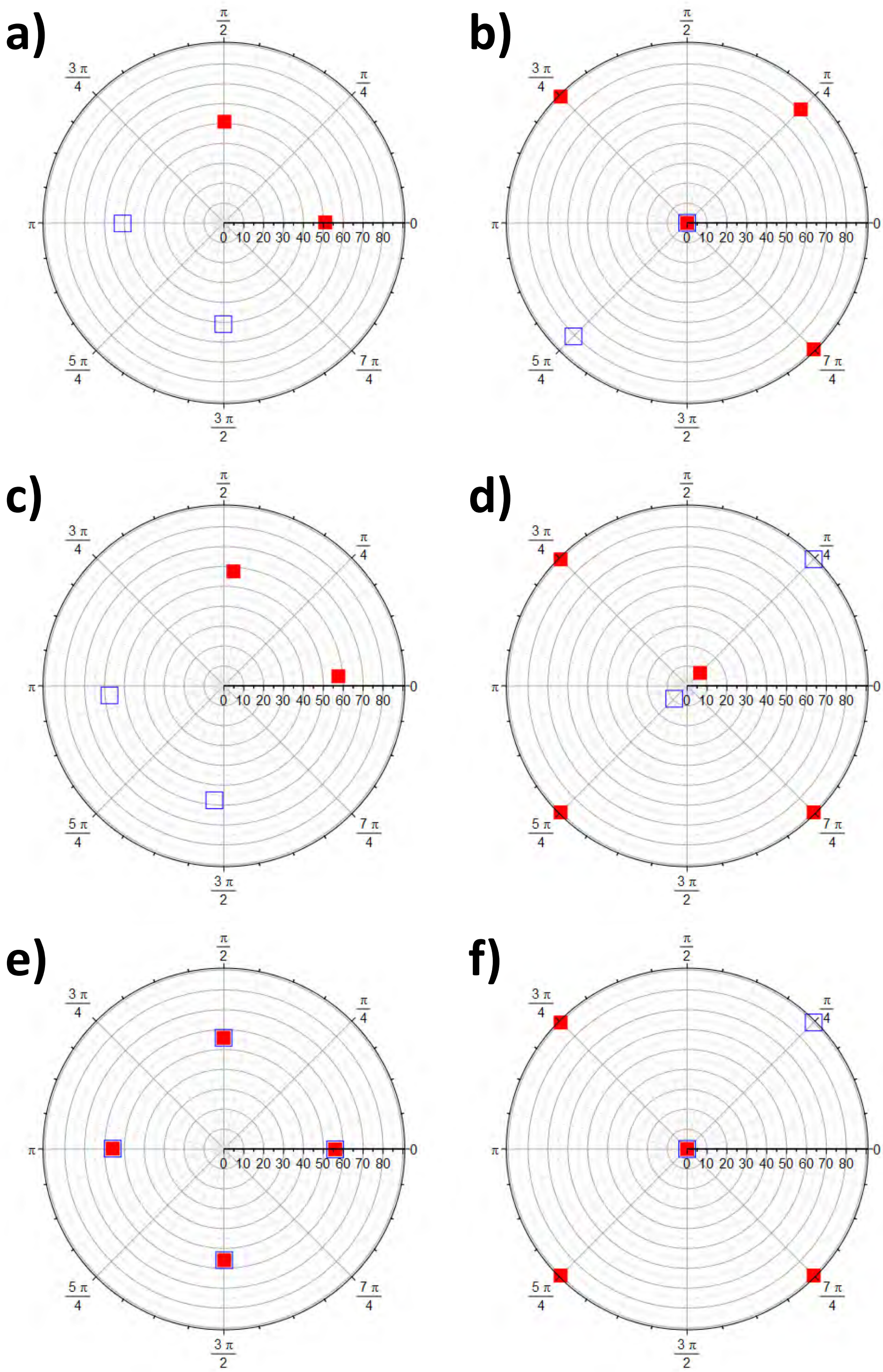

Figure 5.8: Predicted pole figures for the three proposed phases of HZO70 on Si(100). A simple mathematical model was used to generate the pole locations (in 2θ, χ, and ϕ) for the relevant Bragg peaks of m- and o-HZO, using the bulk lattice parameters of m-HfO_2 [91] and o-ZrO_2 [273] as a starting point. For each set of Miller indices, the d-spacing was calculated, as well as the reciprocal space director vector for that plane family. Then, by keeping that vector's angles to a set of basis vectors constant, and rotating the basis by an arbitrary amount in χ and ϕ, the pole locations for any lattice plane of any m- and o-HZO domain could be calculated and plotted. Here a simple polar diagram is used, and the experimental data uses stereographic projections. Diffraction intensities were not included in the model.

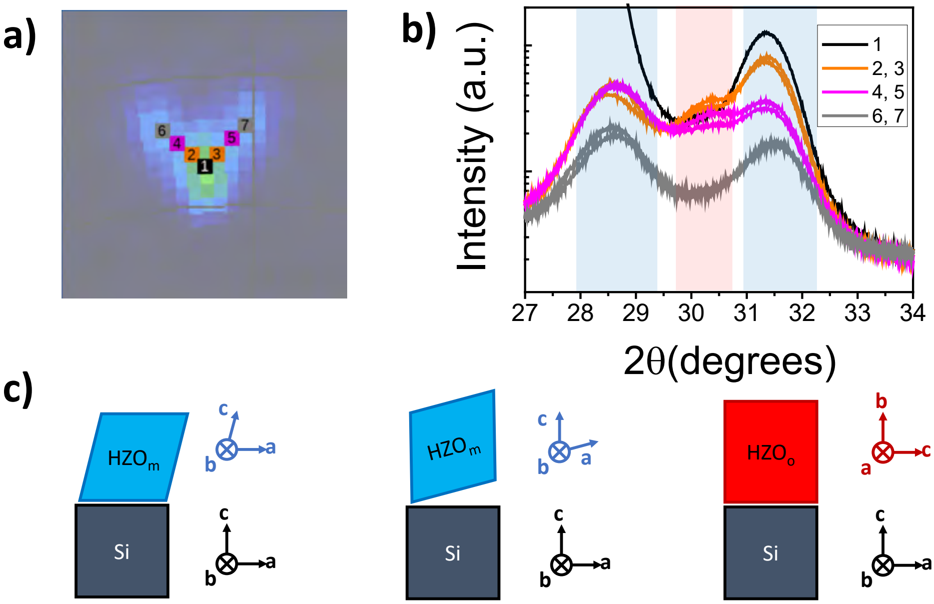

Figure 5.9: Phase coexistence and domains. a) From Figure 5.7c (10 nm film thickness), one of the {111} poles and its corresponding satellites are zoomed in. The black pixel corresponds to $\chi = 53^o$, where the {111} main pole is the most intense. The gray pixels correspond to $\chi = 58^o$ where the satellites are the most intense. A progression from black to gray traverses through orange and magenta pixels, which correspond to purposeful misalignment ("well-aligned" conditions are obtained by maximizing the intensity, which would ignore information from orange and magenta pixels). b) With the color coding scheme as described in a), $2\theta/\omega$ scans were then performed at various χ values from the black pixel to the gray pixel. At the black or gray pixels, peaks corresponding to monoclinic {111} d-spacings are observed. In the orange and magenta pixels, however, a {111} peak corresponding to a low-volume phase appears at $2\theta \approx 30.2^o$. c) Sketches of various domains that correspond to the pole figures presented in Figure 5.7 and simulated in Figure 5.8. The left one shows a monoclinic domain with the a-b plane of HZO parallel to the Si(100) plane. This is a very well-oriented growth observed at low film thicknesses (5 nm). The center panel shows a monoclinic domain with the a-b plane misaligned from the Si(100) surface. Negative and positive misorientations can give rise to an accordion-like zigzag pattern. The rightmost panel shows the domain from the low-volume phase (which can be shown to be orthorhombic from the TEM results to follow).

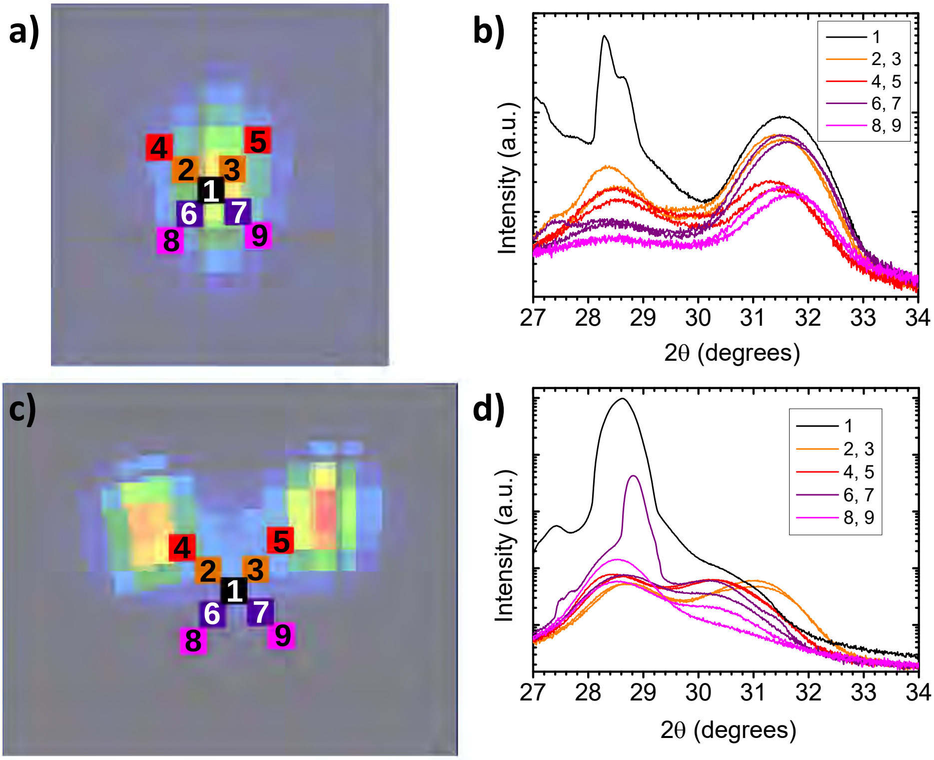

Figure 5.10: {111}) Pole slicing of 5 nm- and 20 nm-thick HZO70 on Si(100). The {111} poles found in Figure 5.7 were analyzed by further pole-slicing. In particular, nine scans were performed near the {111} poles of the 5 nm and 20 nm films, in the positions indicated in a) and c). The black pixel (no misalignment) was aligned using the Si(111) peak. The other pixels are misaligned by 1 or 2 degrees in χ and ϕ away from the black pixel. The results from slicing all nine pixels are plotted in b) and d), with the line colors matching those of the pixels for convenience. For both cases, a similar behavior is observed to that of the 10 nm-thick film. The signature of the low-volume phase is barely visible after slicing the {111} pole of the 5 nm film. However, in the 20 nm film the slicing results in a noticeable peak for the low-volume phase. It is possible that this low-volume phase somehow becomes more prevalent with increasing thickness. However, another convincing explanation is that, with increasing thickness, the fraction of the film that remains with its ab plane parallel to the Si(100) substrate decreases, thus weakening the peak at $\chi = 54^{o}$ enough that the low-volume peak becomes much more obvious.

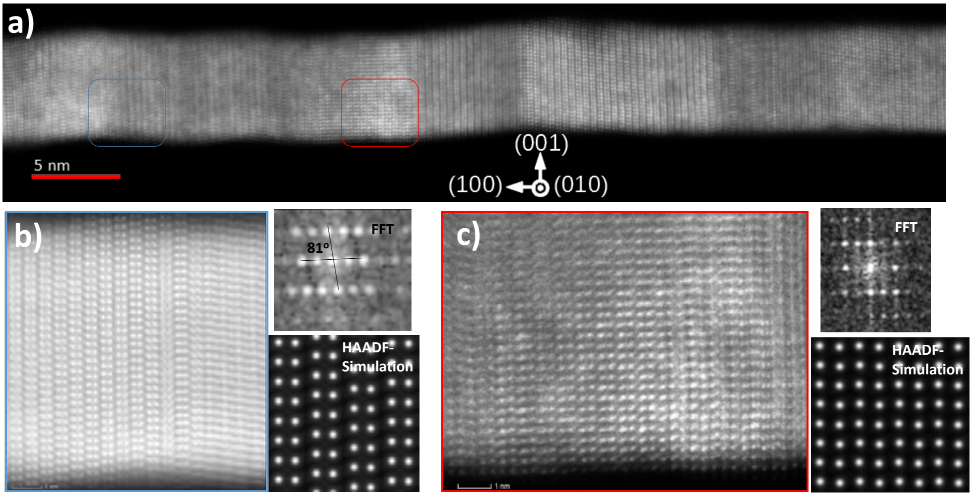

Figure 5.11: Monoclinic domains, orthorhombic domains, and accordions of HZO70 (t = 10 nm) on Si(100). a) Overview cross-sectional HAADF-STEM image along the [010] zone axis, of 10 nm-thick HZO70, showing an accordion-like morphology. b) Zoomed-in view of the region surrounded by a blue box in part a), showing the intersection of two domains. d-spacings estimated from the fast Fourier transform (FFT) obtained from the domain on the left confirm a monoclinic phase. Furthermore, the monoclinic angle (180° - β) can be directly read from the FFT to be ~ 81° in this image. The a-b plane is misoriented with respect to the substrate (normal) by 9°. HAADF-STEM multislice image simulations of the monoclinic phase, clearly matching our domain. If the domain on the left is positively misoriented with the substrate, the domain on the right is negatively misoriented, and their intersection gives rise to an accordion pattern. c) Zoomed-in view of the region surrounded by the red box in a). The d-spacing obtained from FFT clearly shows that this is in the o-phase ($d_{002} = 2.51 \pm 0.02$ Å, and $d_{200} = 2.57 \pm 0.02$ Å). HAADF-STEM image simulations match the real image (with zigzag arrangement of atomic columns along [001]). Simulations from different phases are compared in Figure 5.8. The polar axis, however, is the c-axis which is in-plane.

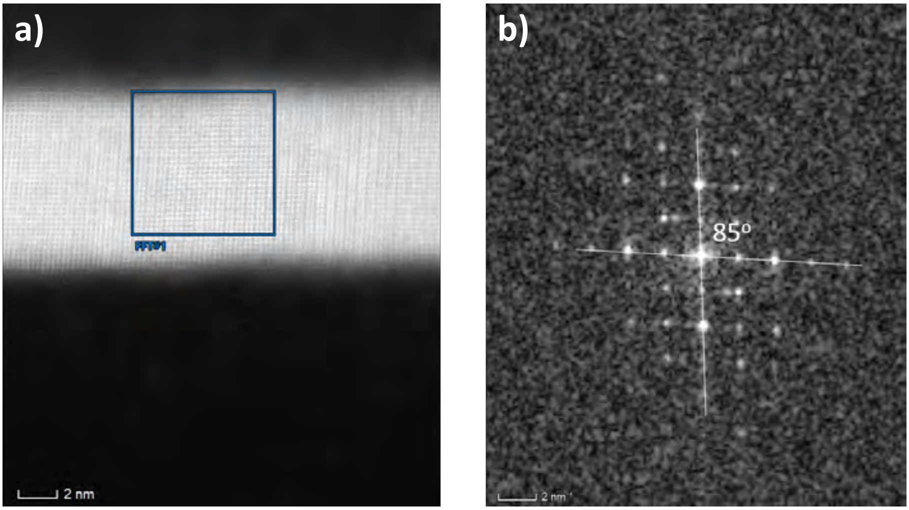

Figure 5.12: a) HAADF-STEM image of HZO70 (t = 10 nm) film on Si(100). b) Fast Fourier Transform obtained from the blue boxed region in a). The d-spacings correspond to a monoclinic phase. The monoclinic angle is β = 95°. The spot corresponding to the ab plane is perfectly aligned with the substrate normal, thus the ab plane is parallel to Si(100). This kind of domain is predominant in the thinner sample (t = 5 nm, see Figure 5.9c), and completely disappears in the thicker sample (t = 20 nm). The most intense pixels from all the poles observed in the pole figures from HZO70 (t = 5 nm, Fig 5.7a and b) arise from these domains.

pared in Figure 5.13). d-spacings for various crystallographic planes obtained from the HAADF-STEM image Fourier transform (Figure 5.11c) match very well with o-phase bulk lattice parameters [274]. In particular, $d_{in\text{-}plane} = 2.51 \pm 0.02$ Å and $d_{out\text{-}of\text{-}plane} = 2.57 \pm 0.02$ Å correspond to d_{002} and d_{200} for the o-phase, suggesting that the polar axis (c-axis in $Pca2_1$ symmetry) is in-plane. Thus, STEM analysis conclusively shows that, in addition to the various kinds of monoclinic domains (Figure 5.9c), a low-volume o-phase, the commonly occurring low-energy ferroelectric phase in polycrystalline thin films, is also present in these films.

Interface and epitaxy. From EDS chemical maps (Figure 5.14a) and Wiener-filtered HAADF-STEM images (Figure 5.14b) at the interface between HZO and Si(100), it is quite clear that a contiguous layer of < 1 nm regrown a-SiO_x exists. Furthermore, there also is an interface c-SiO_2 (β-cristobalite, most likely) structure between Si(100) and the a-SiO_x, which enables epitaxy on Si(001) [259, 270–272]. The in-plane lattice parameter of β-cristobalite (5.03 Å) imposes a compressive strain on any polymorph of HZO. However, the regrowth of a-SiO_x relaxes this strain stabilizing most of the film in a bulk monoclinic phase.

Notably, the grains stabilizing in the o-phase also are interfaced with regrown a-SiO_x. This is unlike growth of HZO (x = 0.7) on Si(111), where there is a clear correlation between the existence of a low-volume phase, and the absence of regrown a-SiO_x on Si. Thus, it appears that the stabilization of o-phase is a result of the inhomogeneous strain fields originating at the intersection of various kinds of nanoscopic monoclinic domains that

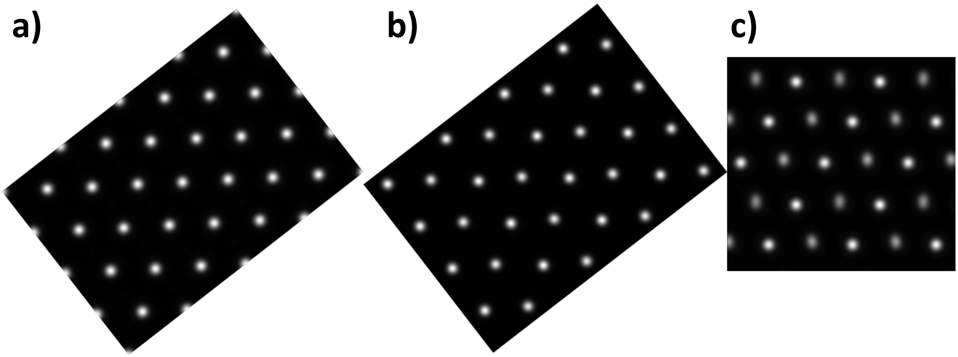

Figure 5.13: HAADF multislice simulations (t = 20 nm) of a) $P4_2/nmc$ (tetragonal), b) $Pca2_1$ (orthorhombic), and c) R3 (rhombohedral) phases. The horizontal direction is the ⟨112⟩ direction, and thecontrast changes in alternate cationic positions are only characteristic of R3.

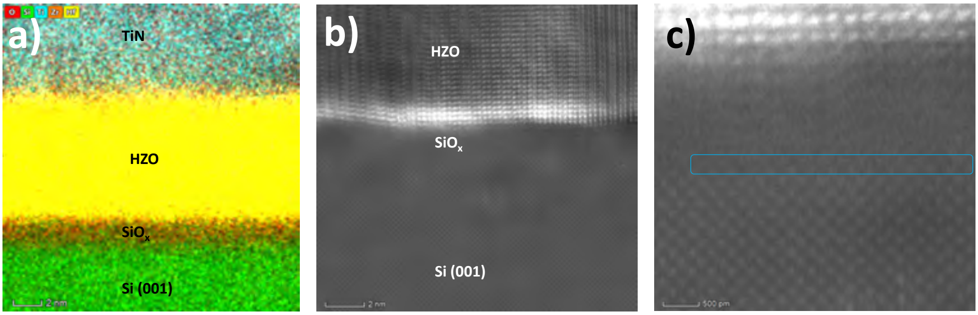

Figure 5.14: Interface and epitaxy on Si(100). a) EDS chemical maps. b) Wiener-filtered HAADF-STEM image. Both frames show a regrown a-SiO_x layer of ~ 1 nm between Si(100) and HZO70. c) Zoomed-in view of Wiener-filtered image in part b. There is also an interfacial crystalline structure (boxed in blue) between Si and a-SiO_x, most likely belonging to c-SiO_2 in β-cristobalite phase. This enables an orientational relationship with the HZO layer.

form the accordion, and not because of strain transfer from the substrate.

Polar r-phase vs polar o-phase. Among all the polar polymorphs of hafnia, first-principles calculations suggest that the o-phase ($Pca2_1$) has the least energy (64 meV/f.u. with respect to the ground state) [42, 236]. The rhombohedral polymorphs (R3m, 158 meV/f.u., and R3, 195 meV/f.u.), though more energetic, seem more favorable to obtain experimentally, under a combination of compressive strain and quite notably a (111) film orientation. Both the films grown on STO substrates by Wei et al. [42] and the films grown on Si(111) in the current work satisfy these conditions and, thus, exhibit a polar r-phase (and not the lower-energy o-phase). These observations, however, are quite contradictory to the theoretical predictions of Liu and Hanrahan [243], possibly owing to the absence of the r-phases in their calculations. It must also be noted that films grown in (001) orientation in this work show a preference for the o-phase, and not the r-phase. Such an orientation dependence of the obtained polar phase is very unique and deserves further investigation.

5.4. CONCLUSIONS

$Hf_{1-x}Zr_xO_2$ (HZO100x) with various compositions in the range 0.5 < x < 0.85 was grown epitaxially on Si(111) and Si(100), without using buffer layers, by PLD. In situ scavenging of the native oxide using decomposition reactions plays a crucial role in achieving epitaxy directly on Si. On both of these substrates, an interfacial phase of c-SiO_2 (most likely β-cristobalite) has been found, and it offers initial compressive strain conditions for the growth of HZO. The regrowth of an amorphous a-SiO_x interlayer has been observed in some parts of the interface. On Si(111), the film on the top of the regions of regrown amorphous oxide relaxes to a bulk nonpolar monoclinic phase, and the film directly in connection with the c-SiO_2 is in the polar r-phase. The volume fraction of the r-phase increases, and the regrown a-SiO_x decreases with increasing Zr content, owing to better reactivity of Zr to participate in the a-SiO_x scavenging reaction (compared to Hf). Ferroelectric measurements show leaky and incipient, but clear, P-E hysteresis loops, evidence to the polar nature of the r-phase. On Si(100), the observed polar o-phase seems to be stabilized by inhomogeneous strains arising out of nanodomain coexistence of the surrounding m-phase. Finally, in addition to strain and surface energy, there also appears to be an orientational dependence to the stabilization of polar phases (at least on Si). That is, the r-phase is favored in (111) orientation, while the o-phase is preferred in (001).

5.5. AUTHOR CONTRIBUTIONS

This work is a collaboration between the University of Groningen (UG) and the Université Paris-Saclay (UPS). P. Nukala (UG) and J. Antoja-Lleonart (UG) carried out the thin film growth and XRD measurements, and wrote the manuscript. P. Nukala and L. Yedra (UPS) did the EM measurements. P. Nukala performed the EM simulations, as well as the electrical measurements, and coordinated the work. J. Antoja-Lleonart wrote and used the code for the pole figure simulations. P. Nukala, J. Antoja, L. Yedra, Y. Wei (UG), B. Dkhil (UPS), and B. Noheda all took part in discussions and text revisions.

SUMMARY

This thesis is about the synthesis and characterization of functional materials made of binary oxides. These materials exist in bulk form, but in this work they are nanostructured, in particular as thin films ranging between a few tens and a few hundreds of nanometers. For the work described in the research chapters, the films are grown on single crystal silicon substrates, which are relatively inexpensive and common in industrial applications.

There are two materials central to this thesis, which are introduced in **Chapter 1**. One is α-quartz, which is a piezoelectric crystalline polymorph of silica (and also germania), thus made of abundant, cheap and nontoxic elements. Although quartz is not a new material, it has otential applications as high frequency oscillators, which require it to be grown at, or cut down to, the nanometer scale. If one were able to grow it in thin film form, it could find usage in those applications, outperforming current devices.

The second material of interest in this work is the solid solution of hafnia and zirconia. These two oxides have very similar structure and chemistry, and they have unusual behavior when synthesized in thin film form. Their nanoscale ferroelectricity is very attractive for use in electronic devices, and to fully exploit it one might be interested in growing these films directly on silicon. This comes with its own set of challenges.

We distinguish two paths for the growth of crystalline oxide thin films. In the first, the films are initially grown in the amorphous state and crystallized at a later stage. This is how we have proceeded with SiO_2 and GeO_2 heterostructures. Because of the configurational strength of the silica matrix, it might be necessary to introduce small metallic impurities to these films that enable their crystallization at reasonable temperatures.

In the second path, the films grow in the crystalline form directly by using elevated temperatures during growth. This includes our work with HZO solid solutions, as well as other cases where, under the growth conditions, the crystalline phase during growth is not the same as under room conditions. To achieve this growth, the nature and quality of the interface is crucial. Therefore, when growing on silicon, one must address the native layer of amorphous oxide that is present at its surface.

Experimental techniques used in this thesis are summarised in **Chapter 2**. One can broadly divide them between synthesis and characterization methods. The two synthesis or growth methods chiefly used in this project are atomic layer deposition (ALD) and pulsed laser deposition (PLD). ALD is a low-temperature, chemical vapor growth technique with very precise thickness control but, in our case, it is largely limited to amorphous materials. PLD takes place in much harsher conditions, with high temperatures and plasma transport being involved, and it is capable of growing epitaxial films films: that means that they retain the crystal ordering of the substrate on which they are grown. The main characterization techniques used in this thesis are a range of X-ray diffraction (XRD) and electron microscopy (EM) techniques, atomic force microscopy (AFM), and spectroscopic ellipsometry.

In **Chapter 3**, the ALD growth of silica-germania films on Si(100) is demonstrated. This begins with the optimization of GeO_2 growth from a TDMAGe precursor, utilizing similar parameters as the growth of SiO_2 from BDEAS. The optimal growth parameters are found to be similar for the two of them, except in terms of reactor temperature. Capacitance measurements reveal that, at low frequencies, the films have much larger dielectric permittivity than expected, possibly due to extrinsic effects such as water absorption. When measured indirectly by spectroscopic ellipsometry, the films show clearly lower permittivity than literature values, which we attribute to lower-than-bulk mass density.

The combined growth of SiO_2 and GeO_2 sublayers, to this point unreported, must proceed at a single temperature, and the choice of 300ºC for this means that GeO_2 will not grow in an optimal regime. Nevertheless, the films display low surface roughness, and our XRR measurements suggest sharp interfaces down to the nanometer level, showing that the ALD-grown multilayers retain their chemical contrast at a nearly unit-cell length scale. Elemental quantification by XPS shows an appreciable carbon contamination, and XRR analysis reveals densities consistent with the dielectric constants determined by spectroscopic ellipsometry of pure GeO_2 films.

The PLD growth of Sr particles on the surface of the silica-germania films is successful in inducing their crystallization upon annealing, but ultimately we have only been able to detect $SrSiO_3$ and α-cristobalite crystals. Only the former appear in EBSD maps, and there they exhibit a clear texture.

In **Chapter 4** the PLD growth of $Si_{0.7}Ge_{0.3}O_2$ thin films on Si(100) is investigated. The growth step takes place at low temperature, so that the films are amorphous. A series of heterostructures with similar thicknesses are grown, each from a target containing a different concentration of $SrCO_3$. $SrCO_3$ is used as a source of Sr, a melting agent. When the films are annealed, their Sr content influences their crystallization behavior. With GIXRD we probe the randomly oriented crystalline phases, and with symmetric $2\theta/\omega$ scans the out-of-plane textured phases. EBSD allows us to index and map the phase and orientation of surface crystalline features.

Our results indicate that the highest concentrations of $SrCO_3$ result in the formation of strontium silicates and germanates, and the lowest concentrations produce very little crystallization. This suggests that the optimal Sr concentration is within our range of 0-20% atomic. Samples with 2.5% and 5% Sr crystallize, albeit locally, in the form of dendritic crystals of α-quartz. X-ray photoelectron spectroscopy allows us to qualitatively describe the influence of the deposition and annealing steps on the relative Si, Ge and Sr contents.

The samples where α-quartz successfully grows show fundamental hurdles to measurable piezoelectricity. While relatively large single crystal domains are achieved, they do not appear uniformly throughout the sample surface. Additionally, in some places the quartz growth is not dendritic but spherulitic, and in many cases we have identified Dauphiné twinning, which can diminish or cancel out the global piezoelectric response. For these reasons, we consider that, although significant progress has been made, the methods used to grow these films need further optimization.

Chapter 5 details the growth of hafnia-zirconia solid solutions by PLD directly on silicon substrates. This time, both Si(100) and Si(111) are explored. The choice of the appropriate PLD growth conditions can result on the scavenging of the native surface oxide layer on the substrates, which allows the new HZO film to grow epitaxially. The crystal structure and texture of the films are analyzed both by X-ray measurements and STEM imaging.

For HZO films of various compositions grown on Si(111), pole multiplicity analysis suggests a slight rhombohedral (ferroelectric) distortion to the film structure, separately to a nonpolar monoclinic phase. The films have a strong {111} texture, and STEM shows direct proof of the successful native SiO_x scavenging. However, some regrowth of this native oxide also takes place, and we link it to the local loss of epitaxy.

When HZO films are grown on Si(100) instead, their crystallization behavior changes. Our study involved samples of the same concentration ($Hf_{0.3}Zr_{0.7}O_2$) but different thicknesses. In it, we elucidate the change of domain structure for the monoclinic fraction of the film as thickness increases by employing pole figure simulations.

In both cases, one of the most important steps towards the identification of the polar phases is the recording of additional $2\theta/\omega$ scans at the film poles, which we have informally called pole slicing. This method allows us to distinguish similarly oriented phases which appear indistinguishable by pole figures alone. With the intentional addition of small misalignments, we can further separate this signal from substrate contributions, and together with STEM data we can identify the polar phases with more confidence. We find a rhombohedral phase grows on Si(111) and an orthorhombic phase on Si(100).

Thus, in this thesis the growth of SiO_2/GeO_2 and HfO_2/ZrO_2, both solutions of binary oxides, on Si substrates has been studied. Their structure and composition have taken a front seat as a means to lead the optimization of growth parameters, be it by PLD or ALD.

SAMENVATTING

Dit proefschrift gaat over de synthese en karakterisatie van functionele materialen gemaakt uit binaire oxiden. Deze materialen bestaan in bulkvorm, maar in dit werk zijn ze nanogestructureerd. In het bijzonder als dunne films variërend van enkele tientallen tot enkele honderden nanometer. Voor het werk beschreven in de onderzoekshoofdstukken zijn de films gegroeid op monokristallijne siliciumsubstraten, die relatief goedkoop en gebruikelijk zijn in industrie toepassingen.

In dit proefschrift staan twee materialen centraal, die in **Hoofdstuk 1** worden geïntroduceerd. De eerste is α-kwarts, een piëzo-elektrische kristallijne polymorf van silica (en ook germania), dus gemaakt uit overvloedige, goedkope en niet-toxische elementen. Hoewel kwarts geen nieuw materiaal is, heeft het mogelijke toepassingen als hoogfrequentie oscillatoren, waarvoor het vereist is te zijn gekweekt op, of teruggebracht tot, de nanometerschaal. Als men α-kwarts in de vorm van dunne films zou kunnen laten groeien, zou het gebruikt kunnen worden in die toepassingen en beter presteren dan huidige apparaten.

Het tweede materiaal van belang in dit proefschrift is de vaste oplossing van hafnia en zirkonia. Deze twee oxiden hebben een zeer vergelijkbare structuur en chemie, en vertonen ongebruikelijk gedrag wanneer ze gesynthetiseerd zijn in dunne filmvorm. Hun ferro-elektriciteit op nanoschaal is erg aantrekkelijk voor gebruik in elektronische apparaten, en om het volledig te benutten zou het interessant kunnen zijn om deze films direct op silicium te laten groeien. Dit komt met een eigen set uitdagingen.

We onderscheiden twee wegen voor de groei van dunne kristallijne oxidefilms. In de eerste worden de films aanvankelijk in amorfe toestand gekweekt en in een later stadium gekristalliseerd. Dit is hoe we te werk zijn gegaan met SiO_2- en GeO_2-heterostructuren. Vanwege de configuratie-sterkte van de silicamatrix kan het nodig zijn om kleine metalen onzuiverheden te introduceren aan deze films, die hun kristallisatie bij redelijke temperaturen mogelijk maken.

Op het tweede pad groeien de films direct in de kristallijne vorm door gebruik te maken van hogere temperaturen tijdens de groei. Dit omvat ons werk met HZO-solide oplossingen, maar ook andere gevallen waarin, onder de groeiomstandigheden, de kristallijne fase tijdens de groei niet hetzelfde is als onder kameromstandigheden. Om deze groei te realiseren, zijn de aard en kwaliteit van de interface cruciaal. Daarom moet men bij het kweken op silicium rekening houden met de inheemse laag amorfe oxide die aan het oppervlak aanwezig is.

De experimentele technieken die in dit proefschrift worden gebruikt, zijn samengevat in **Hoofdstuk 2**. Men kan ze in grote lijnen verdelen tussen synthese- en karakteriseringsmethoden. De twee synthese- of groeimethoden die voornamelijk in dit project worden gebruikt, zijn atomaire laagdepositie (ALD) en gepulseerde laserdepositie (PLD). ALD is een techniek voor chemische gasgroei bij lage temperatuur met zeer nauwkeurige diktecontrole, maar in ons geval is het grotendeels beperkt tot amorfe materialen.

PLD vindt in veel zwaardere omstandigheden plaats, bij hoge temperaturen en plasmatransport. Het is in staat epitaxiale films te laten groeien: dat betekent dat ze de kristalordening behouden van het substraat waarop ze worden gekweekt. De belangrijkste karakteriseringstechnieken die in dit proefschrift worden gebruikt, zijn een reeks röntgendiffractie (XRD) en elektronenmicroscopie (EM) technieken, atoomkrachtmicroscopie (AFM), en spectroscopische ellipsometrie.

In **Hoofdstuk 3** wordt de ALD-groei van silica-germania-films op Si(100) gedemonstreerd. Dit begint met de optimalisatie van de GeO_2-groei met een TDMAGe-precursor, gebruikmakend van vergelijkbare parameters als de groei van SiO_2 met BDEAS. De optimale groeiparameters blijken voor beide vergelijkbaar te zijn, behalve in termen van reactortemperatuur. Capaciteitsmetingen laten zien dat de films bij lage frequenties veel grotere diëlektrische permittiviteit hebben dan verwacht, mogelijk als gevolg van extrinsieke effecten zoals water absorptie. Wanneer indirect wordt gemeten door spectroscopische ellipsometrie, tonen de films duidelijk lagere permittiviteit dan literatuurwaarden. Die schrijven we toe aan lager-dan-bulk massadichtheid.

De gecombineerde groei van SiO_2- en GeO_2-sublagen, die tot op heden niet gerapporteerd zijn, moet bij een enkele temperatuur gebeuren. Daarbij betekent, de keuze van 300°C hiervoor dat GeO_2 niet in een optimaal regime zal groeien. Niettemin vertonen de films een lage oppervlakteruwheid, en onze XRR-metingen suggereren scherpe interfaces tot op nanometerniveau. Dat toont aan dat de ALD-gegroeide multilagen hun chemische contrast behouden bij een lengteschaal van bijna een eenheidscel. Elementaire kwantificering door XPS toont een aanzienlijke koolstofverontreiniging. Verder onthult XRR-analyse dichtheden die consistent zijn met de bepaalde diëlektrische constanten door spectroscopische ellipsometrie van zuivere GeO_2-films.

De PLD-groei van Sr-deeltjes op het oppervlak van de silica-germania-films is succesvol bij het induceren van hun kristallisatie bij uitgloeien, maar uiteindelijk hebben we alleen $SrSiO_3$- en α-cristobalietkristallen gedetecteerd. Alleen die eersten verschijnen in EBSD-kaarten, en daar vertonen ze een duidelijke textuur.

In **Hoofdstuk 4** wordt de PLD-groei van $Si_{0.7}Ge_{0.3}O_2$ dunne films op Si(100) onderzocht. De groeistap vindt plaats bij lage temperatuur, zodat de films amorf zijn. Een reeks van heterostructuren met vergelijkbare diktes worden gekweekt, elk met een verschillende concentratie $SrCO_3$. $SrCO_3$ wordt gebruikt als bron van Sr, een smeltmiddel. Wanneer de films worden gegloeid, beïnvloedt hun Sr-gehalte hun kristallisatiegedrag. Met GIXRD onderzoeken we de willekeurig georiënteerde kristallijne fasen, en met symmetrische $2\theta/\omega$ scans de getextureerde fasen buiten het vlak. Met EBSD indexeren we de fase en brengen we de oriëntatie van kristallijne oppervlaktekenmerken in kaart.

Onze resultaten geven aan dat de hoogste concentraties $SrCO_3$ resulteren in de vorming van strontiumsilicaten en germanaten, en de laagste concentraties produceren heel weinig kristallisatie. Dit suggereert dat de optimale Sr-concentratie binnen ons bereik van 0-20% atomair ligt. Monsters met 2.5% en 5% Sr kristalliseren, zij het lokaal, in de vorm van dendritische kristallen van α-kwarts. Röntgen-fotoelektronenspectroscopie geeft een kwalitatieve omschrijving van de invloed van de depositie- en gloeistappen op de relatieve Si, Ge en Sr inhouden.

De monsters waar α-kwarts met succes groeit, vertonen fundamentele moeilijkheden om hun piëzo-elektriciteit te kunnen meten. Hoewel relatief grote eenkristaldomeinen worden bereikt, verschijnen ze niet uniform over het monsteroppervlak. Bovendien, op sommige plaatsen is de kwartsgroei niet dendritisch maar sferulitisch, en in veel gevallen hebben we Dauphiné-twinning opgemerkt, die de algemene piëzo-elektrische respons kan verminderen of opheffen. Om deze redenen zijn wij van mening dat, hoewel er aanzienlijke vooruitgang is geboekt, de methoden die worden gebruikt om deze films te laten groeien, verder moeten worden geoptimaliseerd.

Hoofdstuk 5 beschrijft de groei van vaste hafnia-zirconia-oplossingen door PLD, direct op silicium substraten. Deze keer worden zowel Si(100) als Si(111) onderzocht. De keuze van de juiste PLD-groeiomstandigheden kan leiden tot het wegvangen van het oorspronkelijke oppervlak-oxidelaag op de substraten, waardoor de nieuwe HZO-film epitaxiaal kan groeien. De kristalstructuur en textuur van de films worden geanalyseerd door zowel röntgenmetingen als STEM-beeldvorming.

Voor HZO-films van verschillende samenstellingen gekweekt op Si(111), suggereert poolmultipliciteitsanalyse een lichte rhomboëdrische (ferro-elektrische) vervorming van de filmstructuur, afzonderlijk naar een niet-polaire monokliene fase. De films hebben een sterke {111} textuur en STEM toont direct bewijs van de succesvolle inheemse SiO_x-opruiming. Enige hergroei van deze oxide vindt echter ook plaats en we koppelen het aan het lokale verlies van epitaxie.

Wanneer HZO-films op Si(100) in plaats van Si(111) worden gekweekt, verandert hun kristallisatiegedrag. Onze studie omvatte monsters met dezelfde concentratie ($Hf_{0.3}Zr_{0.7}O_2$) maar met verschillende diktes. Daarin verhelderen we de verandering van de domeinstructuur van de monokliene fractie van de film naarmate de dikte toeneemt door gebruik te maken van simulaties van poolfiguren.

In beide gevallen is een van de belangrijkste stappen op weg naar de identificatie van de polaire fasen de opname van extra $2\theta/\omega$ scans bij de filmpolen, die we informeel pole-slicing hebben genoemd. Met deze methode kunnen we gelijk georiënteerde fasen onderscheiden die door poolfiguren alleen niet te onderscheiden lijken. Met de bewuste toevoeging van kleine uitlijnfouten kunnen we dit signaal verder scheiden van substraatbijdragen. Samen met STEM data kunnen we de polaire fasen met meer vertrouwen identificeren. Wij vinden dat een rhomboëdrische fase op Si(111) groeit, en een orthorhombische fase op Si(100).

In dit proefschrift wordt dus de groei van SiO_2/GeO_2 en HfO_2/ZrO_2, beiden oplossingen van oxiden, op Si-substraten is bestudeerd. Hun structuur en samenstelling hebben een voorstoel als middel om de optimalisatie van groeiparameters te leiden, of het nu door PLD of ALD is.

CURRICULUM VITAE

CONTACT INFORMATION

Email: jordiantoja.92@gmail.com
LinkedIn: linkedin.com/in/jordi-antoja-lleonart
OrcID: orcid.org/0000-0003-0092-2833

WORK

09/2016 - 03/2021 **PhD Candidate** at Nanostructures of Functional Oxides
University of Groningen (RUG), Groningen, The Netherlands

EDUCATION

09/2014 - 09/2016 **MSc in Nanoscience**
University of Groningen (RUG), Groningen, The Netherlands
Grade: 8.00/10 (*cum laude*)
Thesis title: PLD growth of ferroelectric thin films for wet etching

09/2010 - 09/2014 **BSc in Nanoscience and Nanotechnology**
Autonomous University of Barcelona (UAB), Bellaterra, Spain
Grade: 8.71/10
Thesis title: Study of the resistive switching phenomenon in YBCO superconducting samples

ACHIEVEMENTS

- Winner of the FLASH presentation prize (2019) of the Zernike Institute for Advanced Materials.

- Co-founder of SCN2, the Catalan Society of Nanoscience and Nanotechnology.

PUBLICATIONS

Antoja-Lleonart, J.; Ocelík, V.; Zhou, S.; de Hond, K.; Koster, G.; Rijnders, G.; Noheda, B.; *Growth and crystallization of SiO_2/GeO_2 thin films on Si(100) substrates*, Nanomaterials 11 (7), **2021**, 1654.

Lutjes, N.R.; Zhou, S.; Antoja-Lleonart, J.; Noheda, B.; Ocelik, V.; *Spherulitic and rotational crystal growth of Quartz thin films* (submitted).

Nukala, P.; Ahmadi, M.; Antoja-Lleonart, J.; de Graaf, S.; Wei, Y.; Zandbergen, H.W.; Kooi, B.; Noheda, B.; *In situ heating studies on temperature-induced phase-transitions in epitaxial* $Hf_{0.5}Zr_{0.5}O_2/La_{0.67}Sr_{0.33}MnO_3$ *heterostructures*, Applied Physics Letters 118 (6), **2021**, 062901.

Quinteros, C.P.; Antoja-Lleonart, J.; Noheda, B.; *Plausible physical mechanisms for unusual volatile/non-volatile resistive switching in* HfO_2*-based stacks*, Condensed Matter 6 (1), **2021**, 7.

Antoja-Lleonart, J.; Zhou, S.; de Hond, K.; Huang, S.; Koster, G.; Rijnders, G.; Noheda, B.; *Atomic layer deposition of* SiO_2*-*GeO_2 *multilayers*, Applied Physics Letters 117, **2020**, 041601.

Nukala, P.; Wei, Y.; de Haas, V.; Guo, Q.; Antoja-Lleonart, J.; Noheda, B.; *Guidelines for the stabilization of a polar rhombohedral phase in epitaxial* $Hf_{0.5}Zr_{0.5}O_2$ *thin films*, Ferroelectrics 569 (1), **2021**, 148-163.

Gomez, A.; Antoja-Lleonart, J.; Sauthier, G.; Gich, M.; Carretero-Genevrier, A.; Noheda, B.; Verdaguer, A.; *Quantification of poling gain in lead zirconate titanate (PZT) ceramics by direct piezoelectric force microscopy (DPFM)* (submitted).

Nukala, P.; Antoja-Lleonart, J.; Wei, Y.F.; Yedra, L.; Dkhil, B.; Noheda, B.; *Direct epitaxial growth of polar* $(1\text{-}x)HfO_2\text{-}(x)ZrO_2$ *ultrathin films on silicon*, ACS Applied Electronic Materials 1 (12), **2019**, 2585-2593.

Vila-Fungueirino, J.M.; Gomez, A.; Antoja-Lleonart, J.; Gazquez, J.; Magen, C.; Noheda, B.; Carretero-Genevrier, A.; *Direct and converse piezoelectric responses at the nanoscale from epitaxial* $BiFeO_3$ *thin films grown by polymer assisted deposition*, Nanoscale 10 (43), **2018**, 20155-20161.

ACKNOWLEDGEMENTS

Professor Doctor Beatriz Noheda y Pinuaga. I have tried to rewrite this many times, so here goes the last one. You gave me my first job, and you did not hesitate for a moment at that. Inside and outside the group you inspire and motivate people to do their best, and then some more. You work too much, and I dare you or anybody else to contradict me, but I want you to know that this is one of the reasons I admire you. You have provided a guiding hand while still letting my colleagues and me work with quite a bit of freedom, and I feel like I have learned a lot more this way than if you had been micromanaging from over my shoulder. The most important product of this PhD is not this book, or the propositions, or the samples, or the data, but the lessons. And I owe those to you. De corazón lo digo, gracias jefa.

Speaking of the project, a tip of the hat is due to NWO, our sponsor. The quartz project (TOP-PUNT Grant No. 718.016002) has been an amazing and daring venture, and it is of course directly thanks to them that this thesis is even possible. I hope that their vision is, in time, shared by others and that research efforts continue, if not in quartz in particular, then off the treaded path in general.

Likewise, this thesis could not have been finished without the help of the reading committee. First and closest, Prof. Dr. Maria Antonietta Loi at the Photophysics and Optoelectronics group of the University of Groningen. Slightly to the West of that, at the Spintronics of Functional Materials group, also of the University of Groningen, Prof. Dr. Tamalika Banerjee. And finally, more than a bit further South, Prof. Dr. Erwin Kessels of the Department of Applied Physics at Eindhoven University of Technology. Thank you all for reading my thesis with such short notice and for your helpful and constructive comments.

I think immediately next should follow my sister-in-arms, the one and only Silang Zhou. You and I go way back, to the Nanoscience Master days of 2014. I have seen you change a bit over the last few years, and all I can say about you is that you are the best colleague that I could have asked for. I never heard you speak one word more than was strictly needed, but you always made time to listen and discuss. You taught me almost everything there was to know about the PLD2, which ended up being a lot more necessary than I had anticipated. But more than anything, you made me feel like I was not alone in this crazy roller coaster of a project.

And here I talk about my students, in order of appearance, thus starting with Joshua Levinsky. I don't remember ever asking if it's okay to just call you Josh. I hope I did not offend you all these years. Our work on CSD silica was certainly a special time, and I considered you more a colleague than a student. We discovered a few hard truths and the whole thing was way more difficult than I anticipated. Nevertheless, you showed (and still show) incredible spirit and resolve and helped me get through the bumpy start of my project. You are a brilliant scientist and as a person you almost always have strong and thought-out opinions. Our office discussions about fitting magnetic data were very stimulating and every time I was on the edge of my seat waiting to see what you would discover next.

Jeroen Homan, my second student. I also gave you a seemingly simple task that in the end turned out to be horribly difficult. Our time with the ALD was complicated by both technical and human external factors, and you managed to soldier on in a very new field for you with remarkable success, including some clever ALD growth tricks that I could never have come up with myself. Hafnium oxide can be a harsh mistress and I think you have more than earned your stripes. I regard you as a talented chemist, and your motivation and will to learn make you an excellent researcher.

Sietse Tock, you are without a doubt the worst student I have ever heard of! For real though, it was a blast to work with you on the high-T X-rays, tough and confusing as it may have been. You are extremely capable of working independently and sometimes I felt like I was slowing you down by trying to help. I find you extremely smart, maybe too smart for your own good, and I see nothing but success in your future career, whichever one you choose. And how could I forget about your reasonably-sized superhero sidekick, Mike Uiterwijk, whom I just heard saying “well, well, well” from across the hall!

Back to my mentors: Pavan Nukala, you dragged me into an excellent paper about HZO and its accompanying mighty video spectacle, and you put your heart and soul into both of them. You were always happy to argue about anything, from the current state of academia to the proper way to attach a lightbulb, and I like to think that because of it I have learned to sometimes let go of my own viewpoint, which has traditionally been difficult for me. I was happy to have you as a colleague, and I am extremely lucky to have you as a friend.

Cynthia Quinteros, my unofficial jedi master, you are one of the strongest and most driven people I have met in this line of work. Many of the people in this list owe you their samples or research data one way or another, as do I. Our discussions not only about work, but life in general, kept me sane enough to carry on, as did finding you in the building at the weirdest hours of the weirdest days. Know that, wherever you are, you bring all of this to the people around you.

Václav Ocelík, or Vasek as the common folk would say, when you joined the group I could not have expected how crucial you would be to my own project. Everybody knows that you are an ace with the microscope, but your expertise in metallurgy, mathematics and materials science makes you a true Renaissance man. You taught us things about the crystallization process that I don’t think we could ever have even thought of without you, and we found truly incredible stuff in our samples thanks to your tenacity and strength of character. Thank you for playing!

To our friends in Twente I say, it was great working with you. Doubtless, we all enjoyed a great deal of independence, but in the end this was still a joint project. Our update meetings were a great source of perspective and fierce discussion. Kit de Hond, you are a pleasure to work with, snarky humor included, and I have the deepest admiration for you as someone who, while working on DFT, also came through with some extraordinary measurements on samples from our lab. Sizhao "Fox"Huang, you likewise took some lightning-fast XPS measurements at the height of the pandemic, which left me impressed and grateful. Professors Gertjan Koster and Guus Rijnders, you were always ready to hear whatever results I presented to you, and replied with expert, constructive comments and questions. This is what you want in a project collaborator, and it motivated me to try harder.

Now moving on momentarily to the sunny South, Adrian Carretero-Genevrier, at the Université de Montpellier. You were always excited about collaborating, helping us out with understanding the CSD approach to quartz, and even inviting me to work for a short time in the NanoChemLab when it did not work out. It was an honor to stay in your group and to work with you in a couple publications. José Manuel Vila-Fungueiriño (Jose para todos) Qianzhe Zhang, David Sánchez, Claire Jolly and Vincent Stunt, you guys are great, and though by now we are all scattered to the four winds I remember our good times together. Just as with the Colombière buddies, Christy Fadel and Otmane Khalfaoui, thank you for the good times around Montpellier.

On to the researchers of the ICMAB in Barcelona: Mariona Coll, thank you for offering your ALD expertise, and for always being ready to help out. Though we have only met on a handful of occasions, you had a considerable impact on this thesis. Martí Gich, also of the ICMAB, your encouragement in the initial stages of this project kept me going forward. Andrés Gómez, also at the ICMAB, your brilliant work on DPFM really left me wanting to know more, and I am happy to have seen you do it in person and to have collaborated with you. Thank you all!

Back to Groningen, the vast majority of the experimental work shown in this thesis would not have been possible without support from several staff members. I want to start by thanking our very own Henriët van Mil-Boddeveld, the master of puppets. Without microscopes and lasers, the research would still continue, but you are one of the few people without whom we could never carry on. You are always there to help us navigate the paperwork, which is great, but more importantly, when we are not in your office you take care of everyone's scheduling and keep this group (and other groups as well) afloat. Thank you for all of that.

Graeme Blake, I distinctly and specifically remember a nail-bitingly thrilling discussion in your office about the Scherrer equation. Every time that anybody stands in front of the research group with any doubts revolving around X-ray diffraction, thermoelectrics, or pretty much any other field, you always have expert and polite insights to offer. And on the dark side, all of us who were present will forever recall with fear and a cold sweat your righteous whistle-wielding at Vlieland!

Moving on to the technicians, let's start with Jacob Baas, the man behind the moustache. I cannot begin to say how much you have done for me, and everybody else, but I have the feeling that you probably know quite accurately. Much like you know everything else approximately! You keep the labs going and the scientists alive (and with all fingers still attached), and it is largely thanks to you that I could make it to the end.

Henk Bonder, the man with a plan. I lost count of all the stuff that you fixed or built from scratch for us. Many times there was a problem in the lab (or in the office for that matter), or we needed a weird part for a setup, and we all looked at each other and said "Ah, Henk can do this", then you came around and fixed it and we all nodded in silence. The PLD setups would have been dead for years without you, and you made some incredible add-ons, including safety improvements, for many systems. It was also nice, I should say, to have random Spanish and French words thrown at me from accross the hall every now and then.

Gert ten Brink, I was happy to be able to fall back on your expertise when I was stuck in my work. Be it polishing, electron microscopy, or dungeon design, you always seemed to have crazily well-grounded ideas, and I felt like after every conversation with you I walked away a little smarter. Thank you for taking the time to share that with me.

Arjun Joshua, our lines of work very rarely crossed, save for some ALD business, but you strike me as an extremely curious person who always asks well-thought, hard-hitting and relevant questions, very often preceded by "I'm not an expert but...". Thank you for taking over the ALD. Johan Holstein, you helped me get started with clean room work, which turned out to be very important in my project. Thank you for finding the time and for listening to my ALD-related ramblings. Tom Schouten, you were always there when I needed a hand with the ALD and never once complained about the soul-crushing work of switching bottles and testing for leaks. I learned more than a couple tricks for vacuum systems from you, and I am grateful for that. Martijn de Roosz, we met rather briefly but you taught me how to use the substrate cutter and the sputter system, one of which I have avoided like the plague ever since, and one of which was extremely useful to me. I will remember that. Hans de Vries, you took his mantle very graciously, though I am afraid you will need a larger one for yourself. You are extremely talented, I owe you quite a few pieces of clean room wisdom, and you were always kind to me even though the ALD was not necessarily your problem. Diego Ribas, your kindness and guidance made me feel a bit less of a stranger in the APE basement. Thank you all for the hands.

Nick Lutjes, you are a pain to argue with. You're like me, but always right, somehow. Hopefully when you get to my age you too will understand how mad that can make someone. But it was fun obliterating that one STO substrate with a hammer...for science. I think between all of that we also got quite a bit of actual science done. Thank you for being a great project buddy!

On the teaching side, Jin Xu, you showed me the wonders of chemical solution methods, and even though I didn't stick with that, I do remember it very well. You must be happy to know that our group does quite a bit of spin-coating now. Mónica Acuautla, now you have your own group, but when I started doing solid state synthesis you were there for me, and I have tried to pass on your teachings to whoever asked. Yingfen Wei, you helped me get started cutting substrates, using the hydrostatic pellet press and doing GIXRD measurements. It may not have been a big deal for you, but to me it makes a huge difference versus having to figure all of these things out myself. Also, the humiliation to which I was subjected having dinner at your place truly motivated me to learn how to eat with chopsticks, so I guess I also owe you that, in a rather twisted way. Mart Salverda, I could list what you taught me in the X-ray and PLD labs, but I will just summarize it and say that you have helped everyone with everything. I have met very few people with this spirit of cooperation, and we would all be better off with one of you in our lives. Blessed is he whose hand is guided by such compassion and generosity!

Of the Photophysics and Optoelectronics group, I begin with Teodor Zaharia, the master of the ellipsometer, who spent an inordinate amount of time making sure that I understood what I was doing and that the measurements were going well. Also, you taught me that ALT+167 is the degree symbol, which I can never repay in full. Dima Bederak, you were a great ALD teacher, and I was always a bit bummed that I couldn't return the favor in the X-ray lab. Wytse Talsma, I can say with certainty that you are my oldest friend in

Groningen. Thank you for the ellipsometry and ALD lectures, but also for the life lessons. Both of you were amazing colleagues, and constituted my small ALD circle. Thank you for that more than anything.

Let me not forget about Professors Maxim Pschenitchnikov and Steven Hoekstra, who gave me (read: not a physicist) the opportunity to teach their course, Electricity and Magnetism. There were some great moments there, and I learned quite a bit about myself that would otherwise have remained hidden forever. The two of them also taught me important lessons, not only for teaching, but about work ethics and duty, and I will remember those times with a smile. Likewise, I would like to mention here Professor Paris Avgeriou, in charge of my group at Mastering your PhD, who took the time to meet and listen to the wide range of troubles that come with PhD life, and then came up with ideas to try to overcome them.

I would also like to dedicate some well-deserved space here for people who, although not directly involved in my research, teaching, or the production of this thesis, were also an important part of the scientific and social environment that made it possible. I begin, of course, with Machteld Bosma-Kamminga, indubitably a role model and one of the smartest, kindest people I have ever met. Interestingly, also the first one (to the date of writing this, the first of only two) who managed to make me wear a suit. Tom Bosma, you were usually far away, but hanging out with you taught me the definition of "politely cool", and if that was not a thing already, it is now. Thanks for "mastering your PhD"with me!

Liliia Kulish, of all the scary Russian secret agents that I have met you must be the friendliest one. I remember very fondly our time together in the office, and I have the utmost respect for your management of the chem lab. At this point I might want to mention Kirill Kulish also, because both of you bring the standards of work safety up by three orders of magnitude wherever you go. Experimental work should not be allowed wherever you are not present! I learned a lot of chemistry with you two, and also a thing or two about Russian culture. Hanging out with you was awesome also, be it the singing, dancing, travelling, recording, or being secretly photographed from an apartment block across the pond.

I am also thankful to many of my colleagues who made it a joy to work at NFO all these years. Qikai Guo, I have never in my life seen a person who can smile so much. You are a gentleman and a scholar, and I am honored to have worked by your side. Sanne Berg, I think you are one of the few people I know that just understand how much food, sleep and videogames mean to me. Thank you for sharing the office. Winnfried (the Silent) de Haas, after hanging out with both, I can safely say that you are truly the superior de Haas brother. Keep it quiet though, I don’t want Vincent to find out. Ewout van der Veer, since you joined the group I have been amazed at the talent, skill, hard work, and dedication that you display when delivering sick burns, occasionally to me. Ruben Hamming-Green, you seem to always have a clever opinion about everything, yet I feel that you say much, much less than you think. And it’s nice to keep you around for if I need my heart massaged! Jelte van der Valk, likely the finest actor this group has ever seen, thank you for being a great office mate, and for teaching this dinosaur a thing or two about computers. Arash Tebyani, we enjoyed a lot of exciting discussions, both about work and otherwise, and I am happy that we could still meet after you moved away. Vincent de Haas, after hanging out with both, I can safely say that you are truly the superior de Haas brother. Don’t you tell

Winnfried I said that! Evgenios Stylianidis, my cousin from across the puddle, you keep on smiling, and thanks for making me. Jolle Sulter, our collective Reddit front(er) end, thank you for the facts and trivia. It sure feels a bit less lonely when someone I know from the outernet follows the same öbscureIJouTube channels I do. Jan Rieck, we coincided for a rather short time, which did include some nice hanging out and a banging trip to Borkum. But, I think you are a worthy heir to my office spot, an excellent charade artist, and sadly a clear winner of the "Tallest person in the group"belt. Wear it with pride. Miguel Badillo, you are a joy to share the lab with. I have met few people who get so visibly appalled when things are not done properly. Diana Tulip, I remember our serious talks next to the AFM, and I truly hope that you are a bit happier because of them. I know I am! Kim van Adrichem, you are cool to hang with but you need to adjust playback speed to 0.75x. Contrast and brightness are just fine! Hong Lian, you need to find another punching bag now. But thank you for making the office a more magical place. Eric Brand, you are my latest and last office mate. I appreciate your encyclopedic knowledge of history and miscellaneous random facts, both of which truly resonate with me.

And finally, Arnoud Everhardt, the OG, you are an example of research attitude and team spirit. It is now, as my project is coming to an end, that I appreciate most your effort in teaching Silang and me, not only how to do experiments, but how to do science. I would like to think that you advice during my MSc project stuck with me through my PhD. I certainly tried.

On a similar, but different, note, I must mention the esteemed Alexandra Elbakyan. I have never met her or communicated with her directly, so I cannot add nice words about camaraderie here, but I can definitely highlight her vision, some of which I share wholeheartedly, as well as her selflessness. Although the wrong that she seeks to right is slowly being addressed by the community as a whole, many of my colleagues and I owe her gratitude for her hard work and dedication not only to science, but to humanity as a whole.

Now for the folks around the corner, it is time to talk about my "friends in theory": Luis Suarez, my buddy from the colonies, we have been to three continents together and it would take another thesis to talk about all the hanging out, partying, eating and drinking which were always civil and reasonable, and not once involved the police, or chemical assassination of plants, or a furious mime chasing us through a chicken market. With you, we went to the Ziggo Dome to see the D on a rainy February afternoon, which is something that I had been dreaming of for the previous ten years, and that I can never forget. Maria Tsanai, after the trips and years, I can confidently say that you are cooler than ice cold, and your kindness to all around you is truly inspiring. I have also seen you take up some impressive responsibility in organization boards, and take them *seriously*. And as a reminder, you call it "nopal". Nopal. I very much enjoyed kidnapping that guy with you that one time. We should repeat it soon! Alejandro Díaz, I still hate you for taking us to the Lekkel Lekkel. I will have my revenge in this life or the next. The Italians, Riccardo Alessandri and Anna Bondarenko, I feel like it was yesterday that I looked around and said "Hey, where did the Italians go?"for the seventy billionth time. It was great travelling with you guys! And the slightly more American Italian, Goran Giudetti, you piece of art. I feel like I have missed you longer than I have met you, but I know that you are out there doing what you do best. Siva Sudhan, you were always very kind to me, even though I was a stranger, and chatting with you about whatever is always a welcome source of chill. Kathir

Kanagarajan, it sure takes guts to go to Ukraine without speaking a word of Ukrainian or Russian. I admire you for this. Edison Salazar, you listened to me when I rambled about my work and were forever laid back. Thanks to all of you for the good times! And that is it for the theoreticians, there is nobody else.

Arsalan Torke Ghashghaee, of IBM, I am thankful for your expert review of my Dutch summary, but that feels more like a drop in the ocean. I remember meeting you at Het Concerthuis long ago and thinking "What a peculiar fellow". Rest assured, I still think that about you every time we meet. You put a smile on my face when I was at my lowest points, and also at my highest. Thank you for the movie nights, and together with the rest of Sugarspin, for getting me hopping. I have tried many ways to write this, but in short, rock on, you majestic creature!

Selim Sami, if you didn't think you would get an entire paragraph to yourself, it means you don't know half of me half as well as half of you should like. What I would like to say to you, I will say it in person because this text still needs to be approved for the general public, but let it be written in this record that you are one of a kind. Scientifically, I owe you much LaTeX and Python help, as well as a good chunk of what I know about dielectrics. Truly the best roommate I have ever had, and that really is something for the ages because you had to deal with me, from very much up close, during a world crisis that had everyone getting cabin fever. In summary, you're a pretty decent chap and I look forward to our agreed retirement plan together in the Adriatic Sea.

Ara que arribo al final, em permetré la grolleria d'escriure en català, no perquè no vulgui que m'entenguin, sinó perquè toca parlar dels de casa. Josep (Pep!) Ingla Aynés, Sergi Trias Llimós, els veritables Catalans de Groningen. A vosaltres, més que a ningú altre, em puc estalviar de recordar-vos com d'estressant pot arribar a ser treure's el doctorat aquí. I és precisament amb vosaltres, anant a veure el fumbol i fent unes birres, que em vaig sentir més com si mai no hagués marxat de casa. Sigui a Donostia o a Londres, o a Santa Monica o a Singapur, espero que també trobeu amics així de collonuts i que un dia, si ja toca, torneu a casa, a casa de debò. Raquel Rodriguez Lamas, no ens vam conèixer a la UAB, que mira que hauria estat fàcil. Ha estat fantàstic anar-te trobant per altres llocs, a Còrsega (no al carrer, no, a Còrsega de veritat), a Estrasburg i altre cop a l'Autònoma. Gràcies pels ànims sempre! I als companys en absència, la penya de l'espardenya, Pino, Gandu i Turru (amb menció al català honorífic que és en Travis), encara que sols un de vosaltres hagi plantat, a la data d'escriure aquests mots, i que jo sàpiga, un peu a Groningen, sempre hi heu estat en esperit, i els vicis i DND amb vosaltres no poden quedar faltats de mèrit en aquesta bella obra de progrés científic.

Silvia, ja fa anys que ens coneixem però llavors no m'hauria pogut imaginar que series la meva companya de viatge. Hores i hores d'alinear el làser, mirar fixament les passades de l'AFM o provar d'entendre què de nou li passa al difractòmetre de raigs X no s'obliden fàcilment. Ni tampoc l'ajuda amb LaTeX i altres programets, o totes les vegades que m'has escoltat quan em queixava de la feina, i que m'has animat quan estava fent morros i el doctorat m'estava tocant la moral. Gràcies de tot cor.

I ja per acabar, queden la mare, el pare i en Guillem. Podria dir que sense vosaltres mai me n'hauria sortit, però és que sense vosaltres mai hauria començat. Sempre, sempre hi heu estat quan us necessitava, i sempre m'heu fet costat, fins i tot quan no tenia tota la raó o quan m'enfadava per tonteries. Aquesta tesi és sobretot per vosaltres, perquè un bon dia vaig marxar de casa volent ensenyar-vos que el vostre fill petit i germà petit també es pot arremangar i fer alguna cosa de profit, amb les mans i amb el cap. Així que bueno, aquí ho teniu. Està ple de faltes i ja no vull mirar-me'l més, però és un llibre.

Groningen, 24 of July, 2021.

BIBLIOGRAPHY

[1] J. Rödel, K. G. Webber, R. Dittmer, W. Jo, M. Kimura, and D. Damjanovic, *Transferring lead-free piezoelectric ceramics into application,* Journal of the European Ceramic Society **35**, 1659 (2015).

[2] T. Takenaka and H. Nagata, *Present status of non-lead-based piezoelectric ceramics,* Key Engineering Materials **157-158**, 57 (1999).

[3] The European Parliament, *Directive 2000/53/EC of the European Parliament and of the Council on end-of life vehicles,* Official Journal of the European Communities **L269**, 34 (2000).

[4] The European Parliament, *Comission Directive 2013/28/EU amending Annex II to Directive 2000/53/EC of the European Parliament and of the Council on end-of-life vehicles,* Official Journal of the European Union **L135**, 14 (2013).

[5] A. Everhardt, S. Matzen, N. Domingo, G. Catalan, and B. Noheda, *Ferroelectric Domain Structures in Low-Strain BaTiO3,* Advanced Electronic Materials **2**, 1500214 (2016).

[6] Y. Saito, H. Takao, T. Tani, T. Nonoyama, K. Takatori, T. Homma, T. Nagaya, and M. Nakamura, *Lead-free piezoceramics,* Physica Status Solidi B **432**, 84 (2004).

[7] X. Wang, J. Wu, D. Xiao, J. Zhu, X. Cheng, T. Zheng, B. Zhang, X. Lou, and X. Wang, *Giant Piezoelectricity in Potassium-Sodium Niobate Lead-Free Ceramics,* Journal of the American Chemical Society **136**, 2905 (2014).

[8] Y. Makiuchi, R. Aoyagi, Y. Hiruma, H. Nagata, and T. Takenaka, *(Bi 1/2 Na 1/2)TiO3 - (Bi 1/2 K 1/2)TiO3 - BaTiO3-Based Lead-Free Piezoelectric Ceramics,* Japanese Journal of Applied Physics **44**, 4350 (2005).

[9] S. Bauer and F. Bauer, *Piezoelectric Polymers and Their Applications,* in *Piezoelectricity* (Springer Berlin Heidelberg, 2008) pp. 157–177.

[10] J. H. McElhaney, *The Charge Distribution on the Human Femur Due to Load,* The Journal of Bone & Joint Surgery **49**, 1561 (1967).

[11] R. E. Newnham, *Properties of materials,* 1st ed. (Oxford University Press, Oxford, UK, 2005) p. 378.

[12] S. Sundar and J. Chakravarty, *Antimony toxicity,* International Journal of Environmental Research and Public Health **7**, 4267 (2010).

[13] T. Nakamura, *5G Evolution and 6G,* in *2020 International Symposium on VLSI Design, Automation and Test (VLSI-DAT)* (IEEE, 2020) pp. 1–17.

[14] W. C. Young, R. G. Budynas, and A. M. Sadegh, *Roark's formulas for stress and strain,* 8th ed. (The McGraw Hill Companies, 2012) p. 1054.

[15] A. Ballato, *Basic Material Quartz and Related Innovations,* in *Piezoelectricity* (Springer Berlin Heidelberg, 2008) pp. 9–35.

[16] J. Rabe, S. Büttgenbach, J. Schröder, and P. Hauptmann, *Monolithic miniaturized quartz microbalance array and its application to chemical sensor systems for liquids,* IEEE Sensors Journal **3**, 361 (2003).

[17] G. Johnson, *History of the industrial production and technical development of single crystal cultured quartz,* in *Proceedings of the 2004 IEEE International Frequency Control Symposium and Exposition, 2004.*, Vol. 00 (IEEE, 2004) pp. 35–45.

[18] R. Kubena, F. Stratton, D. Chang, R. Joyce, T. Hsu, M. Lim, and R. M'Closkey, *Next Generation Quartz Oscillators and Filters for VHF-UHF Systems,* in *2006 IEEE MTT-S International Microwave Symposium Digest* (IEEE, 2006) pp. 668–671.

[19] B. Jaffe, *Piezoelectric Ceramics* (Academic Press, London, 1971) p. 313.

[20] J. Curie and P. Curie, *Sur l'électricité polaire dans les cristaux hémièdres à faces inclinées.* Comptes Rendus de l'Académie des Sciences **91**, 383 (1880).

[21] J. Curie and P. Curie, *Développement, par pression, de l'électricité polaire dans les cristaux hémièdres à faces inclinées.* Comptes Rendus de l'Académie des Sciences **91**, 294 (1880).

[22] W. H. Bragg, *The X-ray Spectra given by Crystals of Sulphur and Quartz,* Proceedings of the Royal Society of London. Series A. **89**, 575 (1914).

[23] W. H. Bragg and R. E. Gibbs, *The structure of alpha- and beta-quartz,* Proceedings of the Royal Society of London. Series A. **109**, 405 (1925).

[24] G. Lippmann, *Principe de la conservation de l'électricité, ou Second principe de la théorie des phénomènes électriques,* Journal de Physique Théorique et Appliquée **10**, 381 (1881).

[25] J. Curie and P. Curie, *Contractions et dilatations produites par des tensions électriques dans les cristaux hémièdres à faces inclinées,* Comptes Rendus de l'Académie des Sciences **93**, 1137 (1881).

[26] J. Valasek, *Piezo-electric activity of Rochelle salt under various conditions,* Physical Review **17**, 422 (1921).

[27] J. Valasek, *Piezo-electric and allied phenomena in Rochelle salt,* Physical Review **17**, 475 (1921).

[28] L. E. Cross and R. E. Newnham, *History of Ferroelectrics,* Ceramics and Civilization **III**, 289 (1987).

[29] D. J. Griffiths, *Introduction to Electrodynamics*, 4th ed. (Pearson, 2013) p. 604, arXiv:0712.0689 .

[30] C. A. Randall, R. E. Newnham, and L. E. Cross, *History of the First Ferroelectric Oxide, BaTiO3,* (2004).

[31] S. Roberts, *Dielectric and piezoelectric properties of barium titanate,* Physical Review **71**, 890 (1947).

[32] B. Jaffe, R. S. Roth, and S. Marzullo, *Piezoelectric Properties of Lead Zirconate-Lead Titanate Solid-Solution Ceramics,* Journal of Applied Physics **25**, 809 (1954).

[33] G. Shirane, S. Hoshino, and K. Suzuki, *X-Ray Study of the Phase Transition in Lead Titanate,* Physical Review **80**, 1105 (1950).

[34] B. Jaffe, R. S. Roth, and S. Marzullo, *Properties of Piezoelectric Ceramics in the Solid-Solution Series Lead Titanate-Lead Zirconate-Lead Oxide: Tin Oxide and Lead Titanate-Lead Hafnate,* Journal of Research of the National Bureau of Standards **55**, 239 (1955).

[35] G. Shirane, *Phase Transitions in Solid Solutions Containing PbZrO3,* Physical Review **84**, 854 (1951).

[36] G. Shirane and S. Hoshino, *Crystal Structure of the Ferroelectric Phase in PbZrO3 Containing Ba or Ti,* Physical Review **86**, 248 (1952).

[37] G. Shirane and A. Takeda, *Phase Transitions in Solid Solutions of PbZrO3 and PbTiO3 (I) Small Concentrations of PbTiO3,* Journal of the Physical Society of Japan **7**, 5 (1952).

[38] G. Shirane, K. Suzuki, and A. Takeda, *Phase Transitions in Solid Solutions of PbZrO3 and PbTiO3 (II) X-ray Study,* Journal of the Physical Society of Japan **7**, 12 (1952).

[39] G. Shirane and K. Suzuki, *Crystal Structure of Pb(Zr-Ti)O3,* Journal of the Physical Society of Japan **7**, 333 (1952).

[40] V. M. Goldschmidt, *Crystal structure and chemical constitution,* Transactions of the Faraday Society **25**, 253 (1929).

[41] J. Rödel, W. Jo, K. T. P. Seifert, E.-M. Anton, T. Granzow, and D. Damjanovic, *Perspective on the development of lead-free piezoceramics,* Journal of the American Ceramic Society **92**, 1153 (2009).

[42] Y. Wei, P. Nukala, M. Salverda, S. Matzen, H. J. Zhao, J. Momand, A. S. Everhardt, G. Agnus, G. R. Blake, P. Lecoeur, B. J. Kooi, J. Íñiguez, B. Dkhil, and B. Noheda, *A rhombohedral ferroelectric phase in epitaxially strained Hf0.5Zr0.5O2 thin films,* Nature Materials **17**, 1095 (2018), arXiv:1801.09008 .

[43] N. A. Spaldin, *A beginner's guide to the modern theory of polarization,* Journal of Solid State Chemistry **195**, 2 (2012), arXiv:1202.1831 .

[44] K. A. Müller and H. Burkard, *SrTiO3: An intrinsic quantum paraelectric below 4 K,* Physical Review B **19**, 3593 (1979).

[45] K. Driscoll, *Understanding quartz technology in early prehistoric Ireland*, Ph.D. thesis, University College Dublin (2010).

[46] J. A. Harrell, *Utilitarian Stones,* in *UCLA Encyclopedia of Egyptology*, edited by W. Wendrich (Los Angeles, 2012).

[47] J. A. Harrell, *Gemstones,* in *UCLA Encyclopedia of Egyptology*, edited by W. Wendrich (Los Angeles, 2012).

[48] G. Spezia, *La pressione e' chimicamente inattive nella solubilite e riecostituzione del quarzo,* Atti della Reale Accademia delle scienze di Torino **40**, 262 (1904).

[49] R. L. Rudnick and S. Gao, *The Crust,* in *Treatise in Geochemistry*, edited by H. D. Holland and K. K. Turekian (Elsevier, 2005) Chap. 3, p. 663.

[50] R. K. Cook and P. G. Weissler, *Piezoelectric constants of alpha- and beta-quartz at various temperatures,* Physical Review **80**, 712 (1950).

[51] P. Heaney, *Structure and chemistry of the low-pressure silica polymorphs,* in *Silica: Physical Behavior, Geochemistry , and Materials Applications*, 29, edited by P. J. Heaney, C. T. Prewitt, and G. V. Gibbs (De Gruyter, Berlin, Boston, 2019) pp. 1–40.

[52] R. Bechmann, *Elastic and piezoelectric constants of alpha-quartz,* Physical Review **110**, 1060 (1958).

[53] J. Haines, O. Cambon, D. A. Keen, M. G. Tucker, and M. T. Dove, *Structural disorder and loss of piezoelectric properties in Alpha-quartz at high temperature,* Applied Physics Letters **81**, 2968 (2002).

[54] V. Swamy and S. K. Saxena, *A thermodynamic assessment of silica phase diagram,* Journal of Geophysical Research **99**, 11787 (1994).

[55] J. Phalippou, M. Prassas, and J. Zarzycki, *Crystallization of gels and glasses made from hot-pressed gels,* Journal of Non-Crystalline Solids **48**, 17 (1982).

[56] L. Zhao, N. Li, A. Langner, M. Steinhart, T. Y. Tan, E. Pippel, H. Hofmeister, K. N. Tu, and U. Gösele, *Crystallization of amorphous SiO2 microtubes catalyzed by lithium,* Advanced Functional Materials **17**, 1952 (2007).

[57] F. Iwasaki and H. Iwasaki, *Historical review of quartz crystal growth,* Journal of Crystal Growth **237-239**, 820 (2002).

[58] M. Miclau, N. Miclau, M. Poienar, and I. Grozescu, *A new piezoelectric single crystal obtained by Ge doping in the SiO2 structure,* Crystal Research and Technology **44**, 577 (2009).

[59] G. Sauerbrey, *Verwendung von Schwingquarzen zur Wägung dünner Schichten und zur Mikrowägung,* Zeitschrift für Physik **155**, 206 (1959).

[60] M. Tanaka, *An overview of quartz MEMS devices,* in *2010 IEEE International Frequency Control Symposium* (IEEE, 2010) pp. 162–167.

[61] J. R. Vig, *Quartz Crystal Resonators and Oscillators - For Frequency Control and Timing Applications - A Tutorial,* (2014).

[62] N. F. Foster, *Piezoelectricity in thin film materials,* Journal of the Acoustical Society of America **70**, 1609 (1981).

[63] B. J. Williamson, S. Pastiroff, and G. Cressey, *Piezoelectric properties of quartz and cristobalite airborne particulates as a cause of adverse health effects,* Atmospheric Environment **35**, 3539 (2001).

[64] N. Takahashi, M. Hoshogi, T. Nakumura, Y. Momose, S. Nonaka, H. Yagi, Y. Sinriki, and K. Tamanuki, *Catalyst-enhanced vapor-phase epitaxy of quartz thin films under atmospheric pressure,* J. Mater. Chem. **12**, 719 (2002).

[65] N. Takahashi, J. Majima, T. Nakumura, S. Nonaka, H. Yagi, Y. Shinriki, and K. Tamanuki, *Growth of a High Quality Quartz Film on Sapphire by Epitaxy Using Buffer Layers,* Chemistry of Materials **15**, 2889 (2003).

[66] N. Takahashi, T. Nakumura, S. Nonaka, H. Yagi, Y. Sinriki, and K. Tamanuki, *Rapid Growth of Thick Quartz Films by Catalyst-Enhanced Vapor-Phase Epitaxy under Atmospheric Pressure,* Electrochemical and Solid-State Letters **6**, C77 (2003).

[67] N. Takahashi and T. Nakamura, *Quartz Oscillator Films Prepared under Atmospheric Pressure,* Electrochemical and Solid-State Letters **6**, H25 (2003).

[68] G. Devaud, C. Hayzelden, M. J. Aziz, and D. Turnbull, *Growth of quartz from amorphous silica at ambient pressure,* Journal of Non-Crystalline Solids **134**, 129 (1991).

[69] F. Roccaforte, W. Bolse, and K. P. Lieb, *Solid phase epitaxial regrowth of ion beam-amorphized alpha-quartz,* Applied Physics Letters **73**, 1349 (1998).

[70] F. Roccaforte, S. Dhar, F. Harbsmeier, and K. P. Lieb, *Epitaxial crystallization of amorphous SiO2 films deposited on single-crystalline alpha-quartz,* Applied Physics Letters **75**, 2903 (1999).

[71] S. Dhar, W. Bolse, and K.-P. Lieb, *Ion-beam induced amorphization and dynamic epitaxial recrystallization in alpha-quartz,* Journal of Applied Physics **85**, 3120 (1999).

[72] S. Dhar, P. K. Sahoo, S. Gąsiorek, U. Vetter, V. N. Kulkarni, and K. P. Lieb, *Cathodoluminescence and solid phase epitaxy in Ba-irradiated alpha-quartz,* Journal of Applied Physics **97**, 14910 (2005).

[73] S. Gasiorek, S. Dhar, K. P. Lieb, and P. Schaaf, *Laser-induced epitaxial recrystallization after alkali-ion implantion into a-quartz,* Applied Surface Science **247**, 396 (2005).

[74] G. L. Drisko, A. Carretero-Genevrier, M. Gich, J. Gàzquez, D. Ferrah, D. Grosso, C. Boissière, J. Rodriguez-Carvajal, and C. Sanchez, *Water-induced phase separation forming macrostructured epitaxial quartz films on silicon,* Advanced Functional Materials **24**, 5494 (2014).

[75] G. L. Drisko, A. Carretero-Genevrier, A. Perrot, M. Gich, J. Gàzquez, J. Rodriguez-Carvajal, L. Favre, D. Grosso, C. Boissière, and C. Sanchez, *Crystallization of hollow mesoporous silica nanoparticles,* Chemical Communications **51**, 4164 (2015).

[76] A. Carretero-Genevrier, M. Gich, L. Picas, J. Gazquez, G. L. Drisko, C. Boissiere, D. Grosso, J. Rodriguez-Carvajal, and C. Sanchez, *Soft-chemistry-based routes to epitaxial alpha-quartz thin films with tunable textures.* Science (New York, N.Y.) **340**, 827 (2013).

[77] A. Carretero-Genevrier, M. Gich, L. Picas, C. Sanchez, and J. Rodriguez-Carvajal, *Chiral habit selection on nanostructured epitaxial quartz films,* Faraday Discuss. **179**, 227 (2015).

[78] Q. Zhang, D. Sánchez-Fuentes, A. Gómez, R. Desgarceaux, B. Charlot, J. Gázquez, A. Carretero-Genevrier, and M. Gich, *Tailoring the crystal growth of quartz on silicon for patterning epitaxial piezoelectric films,* Nanoscale Advances **1**, 3741 (2019).

[79] W. Stöber, A. Fink, and E. Bohn, *Controlled growth of monodisperse silica spheres in the micron size range,* Journal of Colloid and Interface Science **26**, 62 (1968).

[80] C. J. S. G. W. Brinker, *Sol-Gel Science: The Physics and Chemistry of Sol-Gel Processing*, 1st ed. (Academic Press, Inc., 1990) p. 908.

[81] C. J. Brinker, Y. Lu, A. Sellinger, and H. Fan, *Evaporation-Induced Self-Assembly: Nanostructures Made Easy,* Advanced Materials **11**, 579 (1999).

[82] *U.S. Geological Survey*, Tech. Rep. (2020).

[83] L. Xu, Y. Xiao, A. Van Sandwijk, Q. Xu, and Y. Yang, *Separation of zirconium and hafnium: A review,* in *Energy Materials 2014, Conference Proceedings* (2014) pp. 451–457.

[84] J. Robertson and R. M. Wallace, *High-K materials and metal gates for CMOS applications,* Materials Science & Engineering R **88**, 1 (2015).

[85] T. S. Böscke, P. Y. Hung, P. D. Kirsch, M. A. Quevedo-Lopez, and R. Ramírez-Bon, *Increasing permittivity in HfZrO thin films by surface manipulation,* Applied Physics Letters **95**, 052904 (2009).

[86] T. S. Böscke, J. Müller, D. Bräuhaus, U. Schröder, and U. Böttger, *Ferroelectricity in hafnium oxide thin films,* Applied Physics Letters **99**, 102903 (2011).

[87] J. Muller, T. S. Boscke, S. Muller, E. Yurchuk, P. Polakowski, J. Paul, D. Martin, T. Schenk, K. Khullar, A. Kersch, W. Weinreich, S. Riedel, K. Seidel, A. Kumar, T. M. Arruda, S. V. Kalinin, T. Schlosser, R. Boschke, R. Van Bentum, U. Schroder, and T. Mikolajick, *Ferroelectric hafnium oxide: A CMOS-compatible and highly scalable approach to future ferroelectric memories,* Technical Digest - International Electron Devices Meeting, IEDM , 280 (2013).

[88] J. Muller, P. Polakowski, S. Riedel, S. Mueller, E. Yurchuk, and T. Mikolajick, *Ferroelectric Hafnium Oxide A Game Changer to FRAM?* in *2014 14th Annual Non-Volatile Memory Technology Symposium (NVMTS)* (IEEE, 2014) pp. 1–7.

[89] J. Müller, T. S. Böscke, D. Bräuhaus, U. Schröder, U. Böttger, J. Sundqvist, P. Kücher, T. Mikolajick, and L. Frey, *Ferroelectric Zr0.5 Hf0.5 O2 thin films for nonvolatile memory applications,* Applied Physics Letters **99**, 1 (2011).

[90] J. Müller, T. S. Böscke, U. Schröder, S. Mueller, D. Bräuhaus, U. Böttger, L. Frey, and T. Mikolajick, *Ferroelectricity in simple binary ZrO2 and HfO2,* Nano Letters **12**, 4318 (2012).

[91] R. Ruh and P. W. R. Corfield, *Crystal Structure of Monoclinic Hafnia and Comparison with Monoclinic Zirconia,* Journal of the American Ceramic Society **53**, 126 (1970).

[92] K. Momma and F. Izumi, *VESTA 3 for three-dimensional visualization of crystal, volumetric and morphology data,* Journal of Applied Crystallography **44**, 1272 (2011).

[93] M. H. Park, Y. H. Lee, H. J. Kim, Y. J. Kim, T. Moon, K. D. Kim, S. D. Hyun, and C. S. Hwang, *Morphotropic Phase Boundary of Hf1-xZrxO2 Thin Films for Dynamic Random Access Memories,* ACS Applied Materials and Interfaces **10**, 42666 (2018).

[94] K. Ni, A. Saha, W. Chakraborty, H. Ye, B. Grisafe, J. Smith, G. B. Rayner, S. Gupta, and S. Datta, *Equivalent Oxide Thickness (EOT) Scaling With Hafnium Zirconium Oxide High-K Dielectric Near Morphotropic Phase Boundary,* in *2019 IEEE International Electron Devices Meeting (IEDM)* (IEEE, 2019) pp. 7.4.1–7.4.4.

[95] M. Shandalov and P. C. McIntyre, *Size-dependent polymorphism in HfO2 nanotubes and nanoscale thin films,* Journal of Applied Physics **106**, 084322 (2009).

[96] S. Starschich, T. Schenk, U. Schroeder, and U. Boettger, *Ferroelectric and piezoelectric properties of Hf1-xZrxO2 and pure ZrO2 films,* Applied Physics Letters **110**, 182905 (2017).

[97] H. A. Hsain, P. Sharma, H. Yu, J. L. Jones, F. So, and J. Seidel, *Enhanced piezoelectricity of thin film hafnia-zirconia (HZO) by inorganic flexible substrates,* Applied Physics Letters **113**, 022905 (2018).

[98] Y. Wei, S. Matzen, T. Maroutian, G. Agnus, M. Salverda, P. Nukala, Q. Chen, J. Ye, P. Lecoeur, and B. Noheda, *Magnetic Tunnel Junctions Based on Ferroelectric Hf0.5Zr0.5O2 Tunnel Barriers,* Physical Review Applied **12**, 1 (2019), arXiv:1902.08021 .

[99] Y. Wei, S. Matzen, C. P. Quinteros, T. Maroutian, G. Agnus, P. Lecoeur, and B. Noheda, *Magneto-ionic control of spin polarization in multiferroic tunnel junctions,* npj Quantum Materials **4**, 62 (2019).

[100] M. Mahadevaiah, E. Perez, C. Wenger, A. Grossi, C. Zambelli, P. Olivo, F. Zahari, H. Kohlstedt, and M. Ziegler, *Reliability of CMOS Integrated Memristive HfO2 Arrays with Respect to Neuromorphic Computing,* in *2019 IEEE International Reliability Physics Symposium (IRPS),* Vol. 2019-March (IEEE, 2019) pp. 1–4.

[101] R. L. Puurunen, *Surface chemistry of atomic layer deposition : a case study for the trimethylaluminum/water process,* Journal of Applied Physics **97**, 1 (2005).

[102] J. Hämäläinen, M. Ritala, and M. Leskelä, *Atomic Layer Deposition of Noble Metals and Their Oxides,* Chemistry of Materials **26**, 786 (2014).

[103] A. J. Mackus, J. R. Schneider, C. Macisaac, J. G. Baker, and S. F. Bent, *Synthesis of Doped, Ternary, and Quaternary Materials by Atomic Layer Deposition: A Review,* Chemistry of Materials **31**, 1142 (2019).

[104] M. Coll and M. Napari, *Atomic layer deposition of functional multicomponent oxides,* APL Materials **7**, 1 (2019).

[105] M. Tyunina, M. Plekh, J. Levoska, M. Vehkamäki, M. Hatanpää, M. Ritala, and M. Leskelä, *Dielectric properties of atomic layer deposited thin-film barium strontium titanate,* Integrated Ferroelectrics: An International Journal **102**, 29 (2008).

[106] N. M. Sbrockey, M. Luong, E. M. Gallo, J. D. Sloppy, G. Chen, C. R. Winkler, S. H. Johnson, M. L. Taheri, G. S. Tompa, and J. E. Spanier, *LaAlO3/SrTiO3 Epitaxial Heterostructures by Atomic Layer Deposition,* Journal of Electronic Materials **41**, 819 (2012).

[107] A. R. Akbashev, G. Chen, and J. E. Spanier, *A facile route for producing single-crystalline epitaxial perovskite oxide thin films,* Nano Letters **14**, 44 (2014).

[108] M. D. McDaniel, T. Q. Ngo, S. Hu, A. Posadas, A. A. Demkov, and J. G. Ekerdt, *Atomic layer deposition of perovskite oxides and their epitaxial integration with Si, Ge, and other semiconductors,* Applied Physics Reviews **2**, 1 (2015).

[109] E. L. Lin, A. B. Posadas, L. Zheng, J. Elliott Ortmann, S. Abel, J. Fompeyrine, K. Lai, A. A. Demkov, and J. G. Ekerdt, *Atomic layer deposition of epitaxial ferroelectric barium titanate on Si(001) for electronic and photonic applications,* Journal of Applied Physics **126**, 1 (2019).

[110] R. W. Johnson, A. Hultqvist, and S. F. Bent, *A brief review of atomic layer deposition: from fundamentals to applications,* Materials Today **17**, 236 (2014).

[111] C. Auth, C. Allen, A. Blattner, D. Bergstrom, M. Brazier, M. Bost, M. Buehler, V. Chikarmane, T. Ghani, T. Glassman, R. Grover, W. Han, D. Hanken, M. Hattendorf, P. Hentges, R. Heussner, J. Hicks, D. Ingerly, P. Jain, S. Jaloviar, R. James, D. Jones, J. Jopling, S. Joshi, C. Kenyon, H. Liu, R. McFadden, B. McIntyre, J. Neirynck,

C. Parker, L. Pipes, I. Post, S. Pradhan, M. Prince, S. Ramey, T. Reynolds, J. Roesler, J. Sandford, J. Seiple, P. Smith, C. Thomas, D. Towner, T. Troeger, C. Weber, P. Yashar, K. Zawadzki, and K. Mistry, *A 22nm high performance and low-power CMOS technology featuring fully-depleted tri-gate transistors, self-aligned contacts and high density MIM capacitors,* in *Digest of Technical Papers - Symposium on VLSI Technology* (2012) pp. 131–132.

[112] T. Suntola and J. Antson, *Method for producing compound thin films (US Patent 4058430),* (1977).

[113] J. D. Ferguson, A. W. Weimer, and S. M. George, *Atomic layer deposition of Al2O3 and SiO2 on BN particles using sequential surface reactions,* Chemistry of materials **162-163**, 280 (2000).

[114] D. Hausmann, J. Becker, S. Wang, and R. G. Gordon, *Rapid Vapor Deposition of Highly Conformal Silica Nanolaminates,* Science **298**, 402 (2002).

[115] B. B. Burton, M. P. Boleslawski, A. T. Desombre, and S. M. George, *Rapid SiO2 atomic layer deposition using tris (tert-pentoxy) silanol,* Chemistry of Materials **20**, 7031 (2008).

[116] O. Sneh, M. L. Wise, A. W. Ott, L. A. Okada, and S. M. George, *Atomic layer growth of SiO2 on Si(100) using SiCl4 and H2O in a binary reaction sequence,* Surface Science **334**, 135 (1995).

[117] A. Satta, J. Schuhmacher, C. M. Whelan, W. Vandervorst, S. H. Brongersma, G. P. Beyer, K. Maex, A. Vantomme, M. M. Viitanen, H. H. Brongersma, and W. F. A. Besling, *Growth mechanism and continuity of atomic layer deposited TiN films on thermal SiO2,* Journal of Applied Physics **92**, 7641 (2002).

[118] F. Gao, S. Arpiainen, and R. L. Puurunen, *Microscopic silicon-based lateral high-aspect-ratio structures for thin film conformality analysis,* Journal of Vacuum Science & Technology A: Vacuum, Surfaces, and Films **33**, 10601 (2015).

[119] R. L. Puurunen and F. Gao, *Influence of ALD temperature on thin film conformality: Investigation with microscopic lateral high-aspect-ratio structures,* in *14th International Baltic Conference on Atomic Layer Deposition (BALD)* (2016).

[120] H. M. Smith and A. F. Turner, *Vacuum Deposited Thin Films Using a Ruby Laser,* Applied Optics **4**, 147 (1965).

[121] D. Dijkkamp, T. Venkatesan, X. D. Wu, S. A. Shaheen, N. Jisrawi, Y. H. Min-Lee, W. L. McLean, and M. Croft, *Preparation of Y-Ba-Cu oxide superconductor thin films using pulsed laser evaporation from high Tc bulk material,* Applied Physics Letters **51**, 619 (1987).

[122] G. Rijnders and D. H. Blank, *Real-time growth monitoring by high-pressure RHEED during Pulsed Laser Deposition,* in *Thin Films and Heterostructures for Oxide Electronics,* Multifunctional Thin Film Series, edited by S. B. Ogale (Springer-Verlag, New York, 2005) Chap. 12.

[123] S. C. Skoryna, *Handbook of Stable Strontium*, edited by S. C. Skoryna (Springer US, Boston, MA, 1981).

[124] G. K. Binnig, *Atomic force microscope and method for imaging surfaces with atomic resolution,* (1986).

[125] G. Binnig, H. Rohrer, C. Gerber, and E. Weibel, *Surface Studies by Scanning Tunneling Microscopy,* Physical Review Letters **49**, 57 (1982).

[126] X. Jiang, P. Scott, D. Whitehouse, and L. Blunt, *Paradigm shifts in surface metrology. Part I. Historical philosophy,* Proceedings of the Royal Society A: Mathematical, Physical and Engineering Sciences **463**, 2049 (2007).

[127] H. Hölscher, *AFM, Tapping Mode,* in *Encyclopedia of Nanotechnology*, edited by B. Bhushan (Springer Netherlands, Dordrecht, 2012) pp. 99–105.

[128] P. Eaton and P. West, *Atomic Force Microscopy* (Oxford University Press Inc., 2010) p. 248.

[129] J. Als-Nielsen and D. McMorrow, *Elements of Modern X-ray Physics*, 2nd ed. (John Wiley & Sons, Inc., Hoboken, NJ, USA, 2011) p. 432.

[130] U. Pietsch, V. Holý, and B. Tilo, *High-resolution X-ray scattering: from thin films to lateral nanostrutures*, 2nd ed. (Springer-Verlag, New York, 2004) p. 408.

[131] R. Jenkins, R. Manne, R. Robin, and C. Senemaud, *Nomenclature system for X-ray spectroscopy,* Pure & Applied Chemistry **63**, 735 (1991).

[132] M. Björk and G. Andersson, *GenX : an extensible X-ray reflectivity refinement program utilizing differential evolution,* Journal of Applied Crystallography **40**, 1174 (2007).

[133] H. Fujiwara, *Spectroscopic Ellipsometry: Principles and Applications* (John Wiley & Sons, Inc., 2007) p. 388.

[134] R. F. Egerton, *Physical Principles of Electron Spectroscopy*, 2nd ed. (Springer US, Boston, MA, 2016).

[135] G. Fang, L. Xu, J. Ma, and A. Li, *Theoretical Understanding of the Reaction Mechanism of SiO2 Atomic Layer Deposition,* Chemistry of Materials **28**, 1247 (2016).

[136] J.-H. Lee, U.-J. Kim, C.-H. Han, S.-K. Rha, W.-J. Lee, and C.-O. Park, *Investigation of Silicon Oxide Thin Films Prepared by Atomic Layer Deposition Using SiH 2 Cl 2 and O 3 as the Precursors,* Japanese Journal of Applied Physics **43**, L328 (2004).

[137] S. M. George, O. Sneh, A. C. Dillon, M. L. Wise, A. W. Ott, L. A. Okada, and J. D. Way, *Atomic layer controlled deposition of SiO2 and Al2O3 using ABAB... binary reaction sequence chemistry,* Applied Surface Science **82-83**, 460 (1994).

[138] J. W. Klaus, A. W. Ott, J. M. Johnson, and S. M. George, *Atomic layer controlled deposition of SiO2 films using binary reaction sequence chemistry,* Applied Physics Letters **70**, 1092 (1997).

[139] M. A. Cameron, I. P. Gartland, J. A. Smith, S. F. Diaz, and S. M. George, *Atomic layer deposition of SiO2 and TiO2 in alumina tubular membranes: Pore reduction and effect of surface species on gas transport,* Langmuir **16**, 7435 (2000).

[140] J. W. Klaus, O. Sneh, A. W. Ott, and S. M. George, *Atomic layer deposition of SiO2 using catalyzed and uncatalyzed self-limiting surface reactions,* Surface Review and Letters **6**, 435 (1999).

[141] B. a. McCool and W. J. DeSisto, *Synthesis and Characterization of Silica Membranes Prepared by Pyridine-Catalyzed Atomic Layer Deposition,* Industrial & Engineering Chemistry Research **43**, 2478 (2004).

[142] J. W. Klaus and S. M. George, *Atomic layer deposition of SiO2 at room temperature using NH3-catalyzed sequential surface reactions,* Surface Science **447**, 81 (2000).

[143] W. Gasser, Y. Uchida, and M. Matsumura, *Quasi-monolayer deposition of silicon dioxide,* Thin Solid Films **250**, 213 (1994).

[144] K. i. Yamaguchi, S. Imai, N. Ishitobi, M. Takemoto, H. Miki, and M. Matsumura, *Atomic-layer chemical-vapor-deposition of silicon dioxide films with an extremely low hydrogen content,* Applied Surface Science **130-132**, 202 (1998).

[145] S. Morishita, W. Gasser, K. Usami, and M. Matsumura, *New substances for atomic-layer deposition of silicon dioxide,* Journal of Non-Crystalline Solids **187**, 66 (1995).

[146] S. Morishita, Y. Uchida, and M. Matsumura, *Atomic-Layer Chemical-Vapor-Deposition of SiO2 by Cyclic Exposures of CH3OSi(NCO)3 and H2O2,* Japanese Journal of Applied Physics **34**, 5738 (1995).

[147] J. D. Ferguson, E. R. Smith, A. W. Weimer, and S. M. George, *ALD of SiO2 at Room Temperature Using TEOS and H2O with NH3 as the Catalyst,* Journal of The Electrochemical Society **151**, G528 (2004).

[148] J. Bachmann, R. Zierold, Y. T. Chong, R. Hauert, C. Sturm, R. Schmidt-Grund, B. Rheinländer, M. Grundmann, U. Gösele, and K. Nielsch, *A practical, self-catalytic, atomic layer deposition of silicon dioxide,* Angewandte Chemie - International Edition **47**, 6177 (2008).

[149] F. Hirose, Y. Kinoshita, S. Shibuya, Y. Narita, Y. Takahashi, H. Miya, K. Hirahara, Y. Kimura, and M. Niwano, *Atomic layer deposition of SiO@ from Tris(dimethylamino)silane and ozone by using temperature-controlled water vapor treatment,* Thin Solid Films **519**, 270 (2010).

[150] S. Kamiyama, T. Miura, and Y. Nara, *Comparison between SiO2 films deposited by atomic layer deposition with SiH2[N(CH3)2]2 and SiH[N(CH3)2]3 precursors,* Thin Solid Films **515**, 1517 (2006).

[151] L. Ju and N. C. Strandwitz, *Cyclic azasilanes as volatile and reactive precursors for atomic layer deposition of silicon dioxide,* Journal of Materials Chemistry C **4**, 4034 (2016).

[152] T. Nam, H. Lee, T. Choi, S. Seo, C. M. Yoon, Y. Choi, H. Jeong, H. K. Lingam, V. R. Chitturi, A. Korolev, J. H. Ahn, and H. Kim, *Low-temperature, high-growth-rate ALD of SiO2 using aminodisilane precursor,* Applied Surface Science **485**, 381 (2019).

[153] S.-J. Won, H.-S. Jung, S. Suh, Y. Jin Choi, N.-I. Lee, C. Seong Hwang, and H. Joon Kim, *Growth and electrical properties of silicon oxide grown by atomic layer deposition using Bis(ethyl-methyl-amino)silane and ozone,* Journal of Vacuum Science & Technology A: Vacuum, Surfaces, and Films **30**, 01A126 (2012).

[154] M. L. O'Neill, H. R. Bowen, A. Derecskei-Kovacs, K. S. Cuthill, B. Han, and M. Xiao, *Impact of Aminosilane Precursor Structure on Silicon Oxides by Atomic Layer Deposition,* The Electrochemical Society Interface **20**, 33 (2011).

[155] M. Putkonen, M. Bosund, O. M. E. Ylivaara, R. L. Puurunen, L. Kilpi, H. Ronkainen, S. Sintonen, S. Ali, H. Lipsanen, X. Liu, E. Haimi, S. P. Hannula, T. Sajavaara, I. Buchanan, E. Karwacki, and M. Vähä-Nissi, *Thermal and plasma enhanced atomic layer deposition of SiO2 using commercial silicon precursors,* Thin Solid Films **558**, 93 (2014).

[156] A. Mallikarjunan, H. Chandra, M. Xiao, X. Lei, R. M. Pearlstein, H. R. Bowen, M. L. O'Neill, A. Derecskei-Kovacs, and B. Han, *Designing high performance precursors for atomic layer deposition of silicon oxide,* Journal of Vacuum Science & Technology A: Vacuum, Surfaces, and Films **33**, 01A137 (2015).

[157] L. Huang, B. Han, M. Fan, and H. Cheng, *Design of efficient mono-aminosilane precursors for atomic layer deposition of SiO2 thin films,* RSC Adv. **7**, 22672 (2017).

[158] Seok-Jun Won, Sungin Suh, Myung Soo Huh, and Hyeong Joon Kim, *High-Quality Low-Temperature Silicon Oxide by Plasma-Enhanced Atomic Layer Deposition Using a Metal–Organic Silicon Precursor and Oxygen Radical,* IEEE Electron Device Letters **31**, 857 (2010).

[159] Picosun, private communication.

[160] S. B. Baek, D. H. Kim, and Y. C. Kim, *Adsorption and surface reaction of bis-diethylaminosilane as a Si precursor on an OH-terminated Si (0 0 1) surface,* Applied Surface Science **258**, 6341 (2012).

[161] M. C. Schwille, T. Schössler, F. Schön, M. Oettel, and J. W. Bartha, *Temperature dependence of the sticking coefficients of bis-diethyl aminosilane and trimethylaluminum in atomic layer deposition,* Journal of Vacuum Science & Technology A: Vacuum, Surfaces, and Films **35**, 01B119 (2017).

[162] P. R. Chalker, P. a. Marshall, P. J. King, K. Dawson, S. Romani, P. a. Williams, J. Ridealgh, and M. J. Rosseinsky, *Atomic layer deposition of germanium-doped zinc oxide*

films with tuneable ultraviolet emission, Journal of Materials Chemistry **22**, 12824 (2012).

[163] R. H. Matero, *Atomic Layer Deposition of GeO2 (US Patent),* (2014).

[164] V. Adinolfi, L. Cheng, M. Laudato, R. C. Clarke, V. K. Narasimhan, S. Balatti, S. Hoang, and K. A. Littau, *Composition-Controlled Atomic Layer Deposition of Phase-Change Memories and Ovonic Threshold Switches with High Performance,* ACS Nano **13**, 10440 (2019).

[165] V. Adinolfi, M. Laudato, R. Clarke, V. K. Narasimhan, L. Cheng, and K. Littau, *Atomic layer deposition of germanium-selenium-tellurium compounds for low-leakage, tunable ovonic threshold switches,* Journal of Vacuum Science & Technology A **38**, 052404 (2020).

[166] T. Yoshida, K. Kato, S. Shibayama, M. Sakashita, N. Taoka, W. Takeuchi, O. Nakatsuka, and S. Zaima, *Interface properties of Al 2 O 3 / Ge structures with thin Ge oxide interfacial layer formed by pulsed metal organic chemical vapor deposition,* Japanese Journal of Applied Physics **53**, 1 (2014).

[167] S. Shibayama, T. Yoshida, K. Kato, M. Sakashita, W. Takeuchi, N. Taoka, O. Nakatsuka, and S. Zaima, *Formation of chemically stable GeO2 on the Ge surface with pulsed metal-organic chemical vapor deposition,* Applied Physics Letters **106**, 1 (2015).

[168] M. Kanematsu, S. Shibayama, M. Sakashita, W. Takeuchi, O. Nakatsuka, and S. Zaima, *Effect of GeO2 deposition temperature in atomic layer deposition on electrical properties of Ge gate stack,* Japanese Journal of Applied Physics **55**, 08PC05 (2016).

[169] H. Matsubara, T. Sasada, M. Takenaka, and S. Takagi, *Evidence of low interface trap density in GeO2/Ge metal-oxide-semiconductor structures fabricated by thermal oxidation,* Applied Physics Letters **93**, 1 (2008).

[170] E. Barsoukov and J. R. Macdonald, *Impedance Spectroscopy: Theory, Experiment, and Applications*, 3rd ed. (John Wiley & Sons, Inc., 2018) p. 528.

[171] B. Walker, C. C. Dharmawardhana, N. Dari, P. Rulis, and W. Y. Ching, *Electronic structure and optical properties of amorphous GeO2 in comparison to amorphous SiO2,* Journal of Non-Crystalline Solids **428**, 176 (2015).

[172] F. Bellenger, M. Houssa, A. Delabie, T. Conard, M. Caymax, M. Meuris, K. De Meyer, and M. Heyns, *Electrical Passivation of the (100)Ge Surface by Its Thermal Oxide,* ECS Transactions **11**, 451 (2007).

[173] S. Takagi, T. Maeda, N. Taoka, M. Nishizawa, Y. Morita, K. Ikeda, Y. Yamashita, M. Nishikawa, H. Kumagai, R. Nakane, S. Sugahara, and N. Sugiyama, *Gate dielectric formation and MIS interface characterization on Ge,* Microelectronic Engineering **84**, 2314 (2007).

[174] I. Banu Lucy, *Dielectric behavior of Cu-GeO2 cermet thin films,* Journal of Materials Science **42**, 5875 (2007).

[175] D. M. Roessler and W. A. Albers, *Infrared reflectance of single crystal tetragonal GeO2,* Journal of Physics and Chemistry of Solids **33**, 293 (1972).

[176] C. Sevik and C. Bulutay, *Theoretical study of the insulating oxides and nitrides: SiO2, GeO2, Al2O3, Si3N4, and Ge3N4,* Journal of Materials Science **42**, 6555 (2007).

[177] M. Tamura, J. Nakamura, and A. Natori, *First-principles calculations of the dielectric constant for the GeO2 films,* Key Engineering Materials **470**, 60 (2011).

[178] J. W. Fleming, *Dispersion in GeO 2 -SiO 2 glasses,* Applied Optics **23**, 4486 (1984).

[179] T. N. Nunley, N. S. Fernando, N. Samarasingha, J. M. Moya, C. M. Nelson, A. A. Medina, and S. Zollner, *Optical constants of germanium and thermally grown germanium dioxide from 0.5 to 6.6eV via a multisample ellipsometry investigation,* Journal of Vacuum Science & Technology B, Nanotechnology and Microelectronics: Materials, Processing, Measurement, and Phenomena **34**, 061205 (2016).

[180] G. G. Devyatykh, E. M. Dianov, N. S. Karpychev, S. M. Mazavin, V. M. Mashinskiĭ, V. B. Neustruev, A. V. Nikolaĭchik, A. M. Prokhorov, A. I. Ritus, N. I. Sokolov, and A. S. Yushin, *Material dispersion and Rayleigh scattering in glassy germanium dioxide, a substance with promising applications in low-loss optical fiber waveguides,* Soviet Journal of Quantum Electronics **10**, 900 (1980).

[181] L. Pajasová, *Optical properties of GeO2 in the ultraviolet region,* Czechoslovak Journal of Physics **19**, 1265 (1969).

[182] S. R. Da Silva, G. K. Rolim, G. V. Soares, I. J. Baumvol, C. Krug, L. Miotti, F. L. Freire, M. E. Da Costa, and C. Radtke, *Oxygen transport and GeO2 stability during thermal oxidation of Ge,* Applied Physics Letters **100**, 191907 (2012).

[183] Q. Y. Zhang, K. Pita, C. K. F. Ho, N. Q. Ngo, L. P. Zuo, and S. Takahashi, *Low optical loss germanosilicate planar waveguides by low-pressure inductively coupled plasma-enhanced chemical vapor deposition,* Chemical Physics Letters **368**, 183 (2003).

[184] C. K. F. Ho, H. S. Djie, K. Pita, N. Q. Ngo, and C. H. Kam, *Sintering and Porosity Control of (X)GeO2:(1-x)SiO2 Sol-Gel Derived Films For Optoelectronic Applications,* Electromechanical and Solid-State Letters **7**, F96 (2004).

[185] C. K. F. Ho, K. Pita, N. Q. Ngo, and C. H. Kam, *Optical functions of (x) GeO2 :(1-x) SiO2 films determined by multi-sample and multi-angle spectroscopic ellipsometry,* Optics Express **13**, 1049 (2005).

[186] H. Hosono and J. Nishii, *High photosensitivity and nanometer-scale phase separation in GeO2-SiO2 glass thin films,* Optics Letters **24**, 1352 (1999).

[187] K. Sasan, A. Lange, T. D. Yee, N. Dudukovic, D. T. Nguyen, M. A. Johnson, O. D. Herrera, J. H. Yoo, A. M. Sawvel, M. E. Ellis, C. M. Mah, R. Ryerson, L. L. Wong, T. Suratwala, J. F. Destino, and R. Dylla-Spears, *Additive Manufacturing of Optical Quality Germania-Silica Glasses,* ACS Applied Materials and Interfaces **12**, 6736 (2020).

[188] A. Savitzky and M. J. E. Golay, *Smoothing and Differentiation of Data by Simplified Least Squares Procedures.* Analytical Chemistry **36**, 1627 (1964).

[189] V. Longo, N. Leick, F. Roozeboom, and W. M. M. Kessels, *Plasma-Assisted Atomic Layer Deposition of SrTiO3: Stoichiometry and Crystallinity Studied by Spectroscopic Ellipsometry,* ECS Journal of Solid State Science and Technology **2**, N15 (2013).

[190] S. Zhou, J. Antoja-Lleonart, P. Nukala, V. Ocelik, N. R. Lutjes, and B. Noheda, *Crystallization of GeO2 thin films into alpha-quartz: from spherulites to single crystals,* arXiv (2020), arXiv:2007.03916 .

[191] V. Ranieri, D. Bourgogne, S. Darracq, M. Cambon, J. Haines, O. Cambon, R. Leparc, C. Levelut, A. Largeteau, and G. Demazeau, *Raman scattering study of alpha-quartz and Si1-xGexO2 solid solutions,* Physical Review B **79**, 224304 (2009).

[192] R. M. Taziev, *SAW properties in quartz-like α-GeO 2 single crystal,* Journal of Physics: Conference Series **1015**, 032142 (2018).

[193] E. Le Bourhis, *Glass: Mechanics and Technology*, 2nd ed. (Wiley-VCH Verlag GmbH & Co. KGaA, 2014) p. 416.

[194] C. Jolly, A. Gomez, D. Sanchez-Fuentes, D. Cakiroglu, R. Rathar, N. Maurin, R. Garcia-Bermejo, B. Charlot, M. Gich, M. Bahriz, L. Picas, and A. Carretero-Genevrier, *Soft chemistry assisted On-chip Integration of Nanostructured quartz-based Piezoelectric Microelectromechanical System,* arXiv (2020), arXiv:2007.07566 .

[195] S. W. Lee, J. H. Han, S. Han, W. Lee, J. H. Jang, M. Seo, S. K. Kim, C. Dussarrat, J. Gatineau, Y.-S. Min, and C. S. Hwang, *Atomic Layer Deposition of SrTiO 3 Thin Films with Highly Enhanced Growth Rate for Ultrahigh Density Capacitors,* Chemistry of Materials **23**, 2227 (2011).

[196] W. Lee, J. H. Han, W. Jeon, Y. W. Yoo, S. W. Lee, S. K. Kim, C.-H. Ko, C. Lansalot-Matras, and C. S. Hwang, *Atomic Layer Deposition of SrTiO 3 Films with Cyclopentadienyl-Based Precursors for Metal–Insulator–Metal Capacitors,* Chemistry of Materials **25**, 953 (2013).

[197] W. Nieuwenkamp, *Die Kristallstruktur des Tief-Cristobalits SiO2,* Zeitschrift für Kristallographie - Crystalline Materials **92**, 82 (1935).

[198] F. Nishi, *Strontium Metasilicate, SrSiO3,* Acta Crystallographica Section C Crystal Structure Communications **53**, 534 (1997).

[199] E. A. Owen and G. I. Williams, *A low-temperature X-ray camera,* Journal of Scientific Instruments **31**, 49 (1954).

[200] F. Stratton, D. Chang, D. Kirby, R. Joyce, Tsung-Yuan Hsu, R. Kubena, and Yook-Kong Yong, *A MEMS-based quartz resonator technology for GHz applications,* in *Proceedings of the 2004 IEEE International Frequency Control Symposium and Exposition, 2004.*, September (IEEE, 2005) pp. 27–34.

[201] C. Jolly, A. Gomez, D. Sánchez-Fuentes, D. Cakiroglu, R. Rathar, N. Maurin, R. Garcia-Bermejo, B. Charlot, M. Gich, M. Bahriz, L. Picas, and A. Carretero-Genevrier, *Soft-Chemistry-Assisted On-Chip Integration of Nanostructured α-Quartz Microelectromechanical System,* Advanced Materials Technologies **6**, 2000831 (2021).

[202] D. B. Balitskii, O. Y. Sil'vestrova, V. S. Balitskii, Y. V. Pisarevskii, D. Y. Pushcharovskii, and E. Philippot, *Elastic, piezoelectric, and dielectric properties of alpha-GeO2 single crystals,* Crystallography Reports **45**, 145 (2000).

[203] W. H. Zachariasen, *The atomic arrangement in glass,* Journal of the American Chemical Society **54**, 3841 (1932).

[204] N. Nagasima and H. Enari, *Local Crystallization of Thermal Oxide Film of Silicon,* Japanese Journal of Applied Physics **10**, 441 (1971).

[205] J. Antoja-Lleonart, S. Zhou, K. de Hond, S. Huang, G. Koster, G. Rijnders, and B. Noheda, *Atomic layer deposition of SiO2-GeO2 multilayers,* Applied Physics Letters **117**, 041601 (2020).

[206] F. Bachmann, R. Hielscher, and H. Schaeben, *Texture Analysis with MTEX – Free and Open Source Software Toolbox,* Solid State Phenomena **160**, 63 (2010).

[207] C. Arnold and M. Aziz, *Stoichiometry issues in pulsed-laser deposition of alloys grown from multicomponent targets,* Applied Physics A: Materials Science & Processing **69**, S23 (1999).

[208] G. Henderson, *The Germanate Anomaly: What do we know?* Journal of Non-Crystalline Solids **353**, 1695 (2007).

[209] J. Z. Tischler, J. D. Budai, G. E. Ice, and A. Habenschuss, *Multiple scattering and the 200 reflection in silicon and germanium,* Acta Crystallographica Section A **44**, 22 (1988).

[210] C. Weiss, *New Silicon Nanocrystal Materials for Photovoltaic Applications,* Ph.D. thesis, Friederich-Schiller-Universität Jena (Jena, Germany) (2017).

[211] P. Nukala, J. Antoja-Lleonart, Y. Wei, L. Yedra, B. Dkhil, and B. Noheda, *Direct Epitaxial Growth of Polar (1-x)HfO 2-(x)ZrO 2 Ultrathin Films on Silicon,* ACS Applied Electronic Materials **1**, 2585 (2019).

[212] P.-H. Wei, *The Structure of a-Quartz,* Zeitschrift für Kristallographie - Crystalline Materials **92**, 355 (1935).

[213] F. Nishi, *Strontium Tetragermanate, SrGe4O9,* Acta Crystallographica Section C Crystal Structure Communications **52**, 2393 (1996).

[214] A. G. Shtukenberg, Y. O. Punin, E. Gunn, and B. Kahr, *Spherulites,* Chemical Reviews **112**, 1805 (2012).

[215] C. Frondel, *Secondary Dauphiné twinning in quartz,* American Mineralogist: Journal of Earth and Planetary Materials **30**, 447 (1945).

[216] L. Gránásy, T. Pusztai, G. Tegze, J. A. Warren, and J. F. Douglas, *Growth and form of spherulites,* Physical Review E - Statistical, Nonlinear, and Soft Matter Physics **72**, 1 (2005).

[217] D. Carlström, *Micro X-ray diffraction for use in histochemistry,* Journal of Histochemistry & Cytochemistry **2**, 149 (1954).

[218] R. L. Flemming, *Micro X-ray diffraction (µXRD): a versatile technique for characterization of Earth and planetary materials,* Canadian Journal of Earth Sciences **44**, 1333 (2007).

[219] U. Schroeder, C. Seong Hwang, and H. Funakubo, eds., *Ferroelectricity in Doped Hafnium Oxide: Materials, Properties and Devices* (Elsevier, 2019).

[220] M. H. Park, Y. H. Lee, T. Mikolajick, U. Schroeder, and C. S. Hwang, *Review and perspective on ferroelectric HfO2-based thin films for memory applications,* MRS Communications **8**, 795 (2018).

[221] P. Polakowski, S. Riedel, W. Weinreich, M. Rudolf, J. Sundqvist, K. Seidel, and J. Muller, *Ferroelectric deep trench capacitors based on Al:HfO2 for 3D nonvolatile memory applications,* 2014 IEEE 6th International Memory Workshop, IMW 2014 , 1 (2014).

[222] M. Pešić, M. Hoffmann, C. Richter, T. Mikolajick, and U. Schroeder, *Nonvolatile Random Access Memory and Energy Storage Based on Antiferroelectric Like Hysteresis in ZrO2,* Advanced Functional Materials **26**, 7486 (2016).

[223] H. Mulaosmanovic, J. Ocker, S. Muller, M. Noack, J. Muller, P. Polakowski, T. Mikolajick, and S. Slesazeck, *Novel ferroelectric FET based synapse for neuromorphic systems,* Digest of Technical Papers - Symposium on VLSI Technology , T176 (2017).

[224] J. Müller, E. Yurchuk, T. Schlösser, J. Paul, R. Hoffmann, S. Müller, D. Martin, S. Slesazeck, P. Polakowski, J. Sundqvist, M. Czernohorsky, K. Seidel, P. Kücher, R. Boschke, M. Trentzsch, K. Gebauer, U. Schröder, and T. Mikolajick, *Ferroelectricity in HfO2 enables nonvolatile data storage in 28 nm HKMG,* Digest of Technical Papers - Symposium on VLSI Technology , 25 (2012).

[225] C. C. Fan, C. H. Cheng, C. Y. Tu, C. Liu, W. H. Chen, T. J. Chang, and C. Y. Chang, *Achieving high-scalability negative capacitance FETs with uniform Sub-35 mV/dec switch using dopant-free hafnium oxide and gate strain,* Digest of Technical Papers - Symposium on VLSI Technology , 139 (2018).

[226] M. Dragoman, M. Modreanu, I. M. Povey, S. Iordanescu, M. Aldrigo, C. Romanitan, D. Vasilache, A. Dinescu, and D. Dragoman, *Very large phase shift of microwave signals in a 6nm HfxZr1-xO2 ferroelectric at ±3 V,* Nanotechnology **28**, 38LT04 (2017).

[227] X. Sang, E. D. Grimley, T. Schenk, U. Schroeder, and J. M. LeBeau, *On the structural origins of ferroelectricity in HfO2 thin films,* Applied Physics Letters **106**, 162905 (2015).

[228] K. Florent, S. Lavizzari, M. Popovici, L. Di Piazza, U. Celano, G. Groeseneken, and J. Van Houdt, *Understanding ferroelectric Al:HfO2 thin films with Si-based electrodes for 3D applications,* Journal of Applied Physics **121**, 204103 (2017).

[229] T. Shimizu, T. Yokouchi, T. Oikawa, T. Shiraishi, T. Kiguchi, A. Akama, T. J. Konno, A. Gruverman, and H. Funakubo, *Contribution of oxygen vacancies to the ferroelectric behavior of Hf0.5Zr0.5O2 thin films,* Applied Physics Letters **106**, 112904 (2015).

[230] U. Schroeder, E. Yurchuk, J. Müller, D. Martin, T. Schenk, P. Polakowski, C. Adelmann, M. I. Popovici, S. V. Kalinin, and T. Mikolajick, *Impact of different dopants on the switching properties of ferroelectric hafnium oxide,* Japanese Journal of Applied Physics **53**, 08LE02 (2014).

[231] S. Starschich, D. Griesche, T. Schneller, and U. Böttger, *Chemical Solution Deposition of Ferroelectric Hafnium Oxide for Future Lead Free Ferroelectric Devices,* ECS Journal of Solid State Science and Technology **4**, P419 (2015).

[232] Y. Sharma, D. Barrionuevo, R. Agarwal, S. P. Pavunny, and R. S. Katiyar, *Ferroelectricity in rare-earth modified hafnia thin films deposited by sequential pulsed laser deposition,* ECS Solid State Letters **4**, N13 (2015).

[233] E. D. Grimley, T. Schenk, X. Sang, M. Pešić, U. Schroeder, T. Mikolajick, and J. M. LeBeau, *Structural Changes Underlying Field-Cycling Phenomena in Ferroelectric HfO2 Thin Films,* Advanced Electronic Materials **2**, 1600173 (2016).

[234] J. Lyu, I. Fina, R. Solanas, J. Fontcuberta, and F. Sánchez, *Robust ferroelectricity in epitaxial Hf1/2Zr1/2O2 thin films,* Applied Physics Letters **113**, 082902 (2018).

[235] M. Hoffmann, U. Schroeder, T. Schenk, T. Shimizu, H. Funakubo, O. Sakata, D. Pohl, M. Drescher, C. Adelmann, R. Materlik, A. Kersch, and T. Mikolajick, *Stabilizing the ferroelectric phase in doped hafnium oxide,* Journal of Applied Physics **118**, 072006 (2015).

[236] S. V. Barabash, *Prediction of new metastable HfO2 phases: toward understanding ferro- and antiferroelectric films,* Journal of Computational Electronics **16**, 1227 (2017).

[237] J. Lyu, I. Fina, R. Solanas, J. Fontcuberta, and F. Sánchez, *Growth Window of Ferroelectric Epitaxial Hf 0.5Zr0.5O2 Thin Films,* ACS Applied Electronic Materials **1**, 220 (2019).

[238] C. Zacharaki, P. Tsipas, S. Chaitoglou, S. Fragkos, M. Axiotis, A. Lagoyiannis, R. Negrea, L. Pintilie, and A. Dimoulas, *Very large remanent polarization in ferroelectric Hf1-xZrxO2 grown on Ge substrates by plasma assisted atomic oxygen deposition,* Applied Physics Letters **114**, 112901 (2019).

[239] Q. Luo, H. Ma, H. Su, K. H. Xue, R. Cao, Z. Gao, J. Yu, T. Gong, X. Xu, J. Yin, P. Yuan, L. Tai, D. Dong, S. Long, Q. Liu, X. S. Miao, H. Lv, and M. Liu, *Composition-dependent ferroelectric properties in sputtered HfxZr1-xO2 Thin Films,* IEEE Electron Device Letters **40**, 570 (2019).

[240] K. Katayama, T. Shimizu, O. Sakata, T. Shiraishi, S. Nakamura, T. Kiguchi, A. Akama, T. J. Konno, H. Uchida, and H. Funakubo, *Orientation control and domain structure analysis of {100}-oriented epitaxial ferroelectric orthorhombic HfO2-based thin films,* Journal of Applied Physics **119**, 134101 (2016).

[241] M. H. Park, H. J. Kim, Y. J. Kim, T. Moon, and C. S. Hwang, *The effects of crystallographic orientation and strain of thin Hf0.5Zr0.5O2 film on its ferroelectricity,* Applied Physics Letters **104**, 072901 (2014).

[242] J. Bouaziz, P. Rojo Romeo, N. Baboux, and B. Vilquin, *Characterization of ferroelectric hafnium/zirconium oxide solid solutions deposited by reactive magnetron sputtering,* Journal of Vacuum Science & Technology B **37**, 021203 (2019).

[243] S. Liu and B. M. Hanrahan, *Effects of growth orientations and epitaxial strains on phase stability of HfO2 thin films,* Physical Review Materials **3**, 054404 (2019), arXiv:arXiv:1812.09180v2 .

[244] T. Shimizu, K. Katayama, T. Kiguchi, A. Akama, T. J. Konno, O. Sakata, and H. Funakubo, *The demonstration of significant ferroelectricity in epitaxial Y-doped HfO2 film,* Scientific Reports **6**, 32931 (2016).

[245] A. Chouprik, S. Zakharchenko, M. Spiridonov, S. Zarubin, A. Chernikova, R. Kirtaev, P. Buragohain, A. Gruverman, A. Zenkevich, and D. Negrov, *Ferroelectricity in Hf0.5Zr0.5O2 Thin Films: A Microscopic Study of the Polarization Switching Phenomenon and Field-Induced Phase Transformations,* ACS Applied Materials and Interfaces **10**, 8818 (2018).

[246] P. Li, I. W. Chen, and J. E. Penner-Hahn, *X-ray-absorption studies of zirconia polymorphs. I. Characteristic local structures,* Physical Review B **48**, 10063 (1993).

[247] C. J. Howard, E. H. Kisi, R. B. Roberts, and R. J. Hill, *Neutron Diffraction Studies of Phase Transformations between Tetragonal and Orthorhombic Zirconia in Magnesia-Partially-Stabilized Zirconia,* Journal of the American Ceramic Society **73**, 2828 (1990).

[248] D. M. Adams, S. Leonard, D. R. Russell, and R. J. Cernik, *X-ray diffraction study of Hafnia under high pressure using synchrotron radiation,* Journal of Physics and Chemistry of Solids **52**, 1181 (1991).

[249] G. Sharma, S. V. Ushakov, and A. Navrotsky, *Size driven thermodynamic crossovers in phase stability in zirconia and hafnia,* Journal of the American Ceramic Society **101**, 31 (2018).

[250] J. Lyu, I. Fina, R. Bachelet, G. Saint-Girons, S. Estandía, J. Gázquez, J. Fontcuberta, and F. Sánchez, *Enhanced ferroelectricity in epitaxial Hf0.5Zr0.5O2 thin films integrated with Si(001) using SrTiO3 templates,* Applied Physics Letters **114**, 222901 (2019).

[251] H. Y. Yoong, H. Wu, J. Zhao, H. Wang, R. Guo, J. Xiao, B. Zhang, P. Yang, S. J. Pennycook, N. Deng, X. Yan, and J. Chen, *Epitaxial Ferroelectric Hf0.5Zr0.5O2 Thin Films and Their Implementations in Memristors for Brain-Inspired Computing,* Advanced Functional Materials **28**, 1806037 (2018).

[252] J. Lyu, I. Fina, J. Fontcuberta, and F. Sánchez, *Epitaxial Integration on Si(001) of Ferroelectric Hf0.5 Zr0.5O2 Capacitors with High Retention and Endurance,* ACS Applied Materials & Interfaces **11**, 6224 (2019).

[253] J. S. Moya, R. Moreno, J. Requena, and J. Soria, *Black Color in Partially Stabilized Zirconia,* Journal of the American Ceramic Society **71**, C479 (1988).

[254] S. U. Sharath, S. Vogel, L. Molina-Luna, E. Hildebrandt, C. Wenger, J. Kurian, M. Duerrschnabel, T. Niermann, G. Niu, P. Calka, M. Lehmann, H. J. Kleebe, T. Schroeder, and L. Alff, *Control of Switching Modes and Conductance Quantization in Oxygen Engineered HfOx based Memristive Devices,* Advanced Functional Materials **27**, 1700432 (2017).

[255] R. Materlik, C. Kunneth, and A. Kersch, *The origin of ferroelectricity in Hf1-xZrxO2: A computational investigation and a surface energy model,* Journal of Applied Physics **117**, 134109 (2015).

[256] R. Batra, T. D. Huan, J. L. Jones, G. Rossetti, and R. Ramprasad, *Factors Favoring Ferroelectricity in Hafnia: A First-Principles Computational Study,* Journal of Physical Chemistry C **121**, 4139 (2017).

[257] M. Mulder, *Epitaxial hafnium zirconate on GaN by Pulsed Laser Deposition*, Ph.D. thesis, University of Twente (2019).

[258] T. Sakuma, L. M. Sheppard, and Y. Ikuhara, eds., *Grain Boundary Engineering in Ceramics: From Grain Boundary Phenomena to Grain Boundary Quantum Structures* (American Ceramic Society, 2000) p. 612.

[259] H. Ishigaki, T. Yamada, N. Wakiya, K. Shinozaki, and N. Mizutani, *Effect of the thickness of SiO2 under layer on the initial stage of epitaxial growth process of yttria-stabilized zirconia (YSZ) thin film deposited on Si(001) substrate,* Journal of the Ceramic Society of Japan **109**, 766 (2001).

[260] S. J. Wang and C. K. Ong, *Epitaxial Y-stabilized ZrO2 films on silicon: Dynamic growth process and interface structure,* Applied Physics Letters **80**, 2541 (2002).

[261] A. Lubig, C. Buchal, D. Guggi, C. L. Jia, and B. Stritzker, *Epitaxial growth of monoclinic and cubic ZrO2 on Si(100) without prior removal of the native SiO2,* Thin Solid Films **217**, 125 (1992).

[262] A. Bardal, T. Matthée, J. Wecker, and K. Samwer, *Initial stages of epitaxial growth of Y-stabilized ZrO2 thin films on a-SiOx/Si(001) substrates,* Journal of Applied Physics **75**, 2902 (1994).

[263] D. Dubbink, G. Koster, and G. Rijnders, *Growth mechanism of epitaxial YSZ on Si by Pulsed Laser Deposition,* Scientific Reports **8**, 5774 (2018).

[264] T. Hirai, K. Teramoto, K. Nagashima, H. Koike, S. Matsuno, S. Tanimoto, and Y. Tarui, *Crystal and electrical characterizations of oriented yttria-stabilized zirconia buffer layer for the metal/ferroelectric/insulator/semiconductor field-effect transistor,* Japanese Journal of Applied Physics, Part 1: Regular Papers and Short Notes and Review Papers **35**, 4016 (1996).

[265] D. B. Fenner, A. M. Viano, D. K. Fork, G. A. Connell, J. B. Boyce, F. A. Ponce, and J. C. Tramontana, *Reactions at the interfaces of thin films of Y-Ba-Cu- and Zr-oxides with Si substrates,* Journal of Applied Physics **69**, 2176 (1991).

[266] S. Gsell, M. Fischer, T. Bauer, M. Schreck, and B. Stritzker, *Yttria-stabilized zirconia films of different composition as buffer layers for the deposition of epitaxial diamond/Ir layers on Si(001),* Diamond and Related Materials **15**, 479 (2006).

[267] G. Ockenfuß, F. Baudenbacher, W. Prusseit-Elffroth, K. Hirata, P. Berberich, and H. Kinder, *Preparation and growth of YSZ buffer layers and YBa2Cu3O7- films on silicon (100),* Physica C: Superconductivity **180**, 30 (1991).

[268] H. Myoren, Y. Nishiyama, H. Fukumoto, H. Nasu, and Y. Osaka, *As-Grown Preparation of Ba2YCu3Ox Thin Films on Si with Epitaxially Grown ZrO2 as a Buffer Layer,* Processing of Films for High Tc Superconducting Electronics **28**, 351 (1989).

[269] P. Bunt, W. J. Varhue, E. Adams, and S. Mongeon, *Initial Stages of Growth of Heteroepitaxial Yttria-Stabilized Zirconia Films on Silicon Substrates,* Journal of The Electrochemical Society **147**, 4541 (2000).

[270] A. Ourmazd, D. W. Taylor, J. A. Rentschler, and J. Bevk, *Si - SiO2 Transformation: Interfacial Structure and Mechanism,* Physical Review Letters **59**, 213 (1987).

[271] I. Ohdomari, H. Akatsu, Y. Yamakoshi, and K. Kishimoto, *The structural models of the Si/SiO2 interface,* Journal of Non-Crystalline Solids **89**, 239 (1987).

[272] M. Hane, Y. Miyamoto, and A. Oshiyama, *Atomic and electronic structures of an interface between silicon and beta-cristobalite,* Physical Review B **41**, 637 (1990).

[273] E. H. Kisi, C. J. Howard, and R. J. Hill, *Crystal Structure of Orthorhombic Zirconia in Partially Stabilized Zirconia,* Journal of the American Ceramic Society **72**, 1757 (1989).

[274] O. Ohtaka, T. Yamanaka, S. Kume, N. Hara, H. Asano, and F. Izumi, *Structural Analysis of Orthorhombic Hafnia by Neutron Powder Diffraction,* Journal of the American Ceramic Society **78**, 233 (1995).